Studies of active systems for robotic exploration, wave manipulation, and control of liquids in the Leidenfrost state

Samuel Hidalgo Caballero

PSL UNIVERSITÉ PARIS

THÈSE DE DOCTORAT
DE L'UNIVERSITÉ PSL

Préparée à l'École Supérieure de Physique et de Chimie Industrielles de la ville de Paris

Études des systèmes actifs pour l'exploration robotique, la manipulation des ondes et le contrôle de la caléfaction

Studies of active systems for robotic exploration, wave manipulation, and control of liquids in the Leidenfrost state

Soutenue par
Samuel HIDALGO-CABALLERO
Le 7 décembre 2022

École doctorale n°564
Physique en Île-de-France

Spécialité
Physique

Préparée au
Laboratoire Gulliver UMR 7083

Composition du jury :

Elie RAPHAEL Directeur de Recherche CNRS ESPCI Paris, Université PSL	*Président du jury*
Suzie PROTIERE Chargée de Recherche CNRS, Sorbonne Université	*Rapportrice*
Stéphane DORBOLO Professeur, Universite de Liège	*Rapporteur*
Corentin COULAIS Assistant Profesor University of Amsterdam	*Examinateur*
Emmanuel FORT Professeur ESPCI Paris, Université PSL	*Directeur de thèse*
Matthieu LABOUSSE Chargé de Recherche CNRS, ESPCI Paris, Université PSL	*Codirecteur de thèse*

ESPCI PARIS | PSL

Remerciements

Je tiens à remercier Suzie Protière et Stéphane Dorbolo, qui ont accepté d'être les rapporteurs de mon travail ainsi que Corentin Coulais et Elie Raphael qui l'ont examiné.

Cette thèse représente la synthèse d'un travail d'équipe en collaboration avec mes super directeurs de thèse que je tiens à remercier infiniment. D'une part Emmanuel Fort (il capo), pour son enthousiasme et dynamisme présents chaque jour vécu à l'institut et, d'autre part, Matthieu Labousse (el maestro), pour toutes ses contributions théoriques ainsi que son suivi tout au long de ma thèse. Cela a été un grand honneur et surtout un grand plaisir de travailler avec eux. Je les remercie également pour tout ce que qu'ils m'ont apporté au-delà de la science, les repas, les cafés, les soirées, etc.

Je tiens à remercier les directeurs des deux laboratoires qui m'ont accueilli tout au long de ma thèse. Je remercie d'une part Olivier Dauchot, directeur du laboratoire Gulliver et, d'autre part, Arnaud Tourin, directeur de l'institut Langevin. Grâce à eux j'ai eu la chance d'être entouré de théoriciens de la matière molle ainsi que d'expérimentateurs en physique des ondes. Je remercie aussi tout le personnel administratif des deux laboratoires pour toute l'aide et le support toujours apportés avec un grand sourire.

Je remercie tous les responsables du COFuND UptoParis et CONACYT Mexico pour leur soutien financier. Grâce à eux, j'ai eu l'opportunité d'accomplir mon rêve de venir faire mon doctorat en France, accompagné d'autres doctorants internationaux, tous ayant des qualités scientifiques ainsi qu'humaines exceptionnelles. Je remercie CONACYT Mexico pour la bourse de mobilité et pour le suivi de mon doctorat.

Je tiens à remercier les membres de mon comité de suivi de thèse pour leurs conseils et leur soutien. Je remercie aussi chacun de mes collègues doctorants et postdoctorants de Gulliver et de l'Institut Langevin, en particulier ceux avec qui j'ai eu le plaisir d'avoir des moments de partage, de joie ou de danse: Benjamin, Paul, Vincent, Anwesh, Antoine, Thibaut, Daniel, Max, Jana, Chloë, Hussam, Claudia et Paty. Je ne vais jamais oublier les manipes, congrès, soirées ou voyages que nous avons vécus ensemble.

Je tiens à remercier tous mes amis et, en particulier, ma compagne Aurore et ma belle famille pour l'encouragement au cours de ces années remplies de travail et surtout d'apprentissage. Finalement, je remercie toutes les personnes qui partagent avec moi la passion de la danse, une belle activité qui a été la cerise sur le gâteau durant mon séjour en France.

Contents

Introduction

Active systems have become a rich field of research during the last decades which is probably due to their versatility and multiple possibilities for their dynamics. From micro-sized entities to macroscopic systems, they have the unique feature of being able to convert an external or embedded source of energy into net propulsion. They can be natural or artificial systems performing from simple to very complex interactions with their environment in order to direct their motion. A very large number of such systems exists in the universe, but in this thesis we focus our attention on the study of the three following ones: a simple spherical robot, an active damped medium, and liquids in the Leidenfrost state. We are going to show that a controlled actuation of these inherently out-of-equilibrium systems can result into nontrivial applications such as shape recognition, time reversal of waves or stabilization of levitating liquids. Thus, the goal of this thesis is to demonstrate these possibilities for systems whose dynamics can be well controlled.

This manuscript is divided into three independent parts, corresponding to the applications of each active system. In the first part, we are interested in the geometrical information that can be obtained from random explorations of an arbitrary region in the plane. In our case, we employ a very limited and randomly moving spherical robot that can perform straight line motion. The first question we want to answer is whether we can estimate the area and perimeter of the explored region. We will see that we can address this problem by using the powerful tools given from the branch of mathematics named statistical geometry. One of its most remarkable results states that the average length of the random crossing chords is proportional to the ratio between the area and perimeter of the explored region. This was first demonstrated by Cauchy in 1836 [1] for the case of lines randomly intersecting convex shapes. More recently, it has been shown that this invariant also holds for non-convex regions [2], Brownian motion [3] and random distributed closed-loop trajectories crossing a region [4]. However, Cauchy's formula gives us only the ratio between the area and perimeter of the region of interest; then, a second general invariant is needed to separately obtain both geometrical quantities for any shape in 2D. We will analytically demonstrate this new invariant, and along the way, we will find other interesting statistical geometry results. From this, we will propose a simple strategy for recognizing any shape in 2D thanks to the space representation given only by the area and perimeter. Finally, an extension of this idea for reading letters and words from a text will be addressed.

In the second part, we study mechanical waves that propagate in an active medium whose damping can perform a programmable abrupt change in time. This will allow us to introduce a counter intuitive method to perform time reversal of waves thanks to the application of damping pulses. Inspired by the instantaneous time reversal mirrors designed for surface water waves in [5], [6], where a sudden change in the propagation speed generates a time reversed wave, here, we are interested in the possibility of performing a time-reversal operation of an initial propagating wave thanks to the application of a time-controlled damping pulse. An experimental proof of concept will be given with a system composed of magnets which repel each other and are placed on an air cushion to remove the friction generated by the contact between the particles and the surface. The magnets are placed one by one, and they self-arrange forming an ordered structure of levitating magnets, corresponding to an equilibrium position. The whole array of magnets behave like an elastic medium through which phonon waves can propagate. An experimental time-reversed operation of an initial propagating mechanical perturbation will be demonstrated. This procedure generates a counter-propagating wave that interferes with the initial one, creating a time-localized standing wave. Thus, by a second application of a damping pulse, we are able to totally annihilate the wavefield. This idea will be finally discussed for tailoring broadband waves via selective annihilation or concentration of their monochromatic components.

The third part of this thesis concerns the study of liquids that are in the Leidenfrost state. This phenomenon occurs when a liquid is placed on a substrate whose temperature is much higher than the boiling point, creating an insulating vapor layer that prevents the contact between the hot substrate and the rest of the liquid [7]. Very small volumes of liquid have a quasi-steady dynamics but larger volumes are unstable and create chimneys due to the increase of the vapor pressure in the bottom part of the liquid [8]. Here, we will propose a mechanism to stabilize these liquids thanks to a controlled evacuation of the insulating vapor. We experimentally demonstrate that a perforated solid substrate can totally suppress the appearance of chimneys, with a remarkable stabilization of the levitated liquid during the slow evaporation process. We also do numerical simulations to solve the Navier-Stokes equations coupled with capillary forces. They corroborate the stabilization mechanism and allow us to extend our analysis to more complex geometries. Finally, we will see that thanks to an asymmetric drain of vapor we can drive the liquid motion. This represents a new method to propel liquids in the Leidenfrost state as an alternative to the well-known ratchet-based propelling mechanisms [9], [10].

1

Shape recognition via random explorations

1.1 Introduction

In this part of the thesis, we are interested in developing a simple strategy to evaluate and recognize a region by means of a random exploration. This problem will be addressed by using the powerful tools provided by statistical geometry, which are going to be applied to the study of random explorations of bounded domains. One remarkable result of this branch of mathematics is the Cauchy formula, initially given for the mean chord length of random distributed lines crossing a convex region [1]. An interesting fact is that this formula was also derived by Dirac [11], when he was working on the Manhattan project because the mean chord length resulted to be a crucial parameter for achieving stable nuclear reactions [12]. Surprisingly, this invariant property holds in the case of random motions, which has been recently demonstrated in [3], and experimentally verified in multiple physical systems, for instance the mean traveled distances of populations of animals that enter and exit a region [13], [14], or the mean path length of light after being scattered by a complex medium [15]. We will demonstrate that Cauchy's formula remains also valid for the case of arbitrary closed-loop trajectories provided that no trajectory can be completely enclosed by the domain [4]. Below this threshold, the mean arc length differs from Cauchy's formula as it decreases with the size of the trajectory.

The area and perimeter are two invariant properties that can give us a lot of geometrical information about any 2D region. These two parameters are then the natural descriptors of any arbitrary region, and they can be the first candidates to be employed in a shape recognition strategy. The mean chord length theorem allows only to estimate the ratio between the area and perimeter for any arbitrary region in 2D. Although this ratio is already related to the macroscopic geometrical properties of the

explored region, it is not sufficient to determine its area or perimeter separately. Then, we need a second formula relating the area and perimeter of an arbitrary region to its chord length distribution. Only a second formula exists in the literature for random straight lines crossing convex shapes, which was demonstrated by Crofton [16], who was able to relate the third moment of the chord length distribution to the square of the area divided by its perimeter. Unfortunately, this formula is not valid for non-convex regions, which are ubiquitous in nature. Thus, an important theoretical work is requested in order to seek a second general statistical invariant that has to be also valid for non-convex shapes. This will be introduced and demonstrated, which represents an important theoretical achievement for shape recognition. From these two invariants, now we have access to a direct estimation of the area and perimeter of any region in 2D. Then, every 2D shape can be classified in a space representation given from these two parameters and this will become the principle of a shape recognition strategy. We will implement an experimental proof of concept of this recognition technique with a very limited robot that can move in a random oriented straight-line motion and is only capable to detect if it is inside of a projected region in 2D. Thanks to the use of these statistical invariants the robot can perform an autonomous recognition of complex regions such as the silhouettes of famous monuments. Finally, by extending this strategy to the recognition of letters and words, we will demonstrate that a blind and disoriented robot can also read a text.

1.2 Geometric probability

The first association of probability theory and geometry was done in the 17th century by Newton when he was interested in the possibility of having irrational probabilities [17]. He imagined a ball falling on a circle divided in two sectors whose areas have a ratio of 2 over $\sqrt{5}$ (fig. 1.1a). He stated that the chances to hit one of the regions are proportional to the area fraction. By doing this, he obtained an estimation of the area of each region by only counting the proportion of hits. In other words, Newton was laying the foundation for what we now know as Monte Carlo simulations [18] for the estimation of physical parameters based on random sampling.

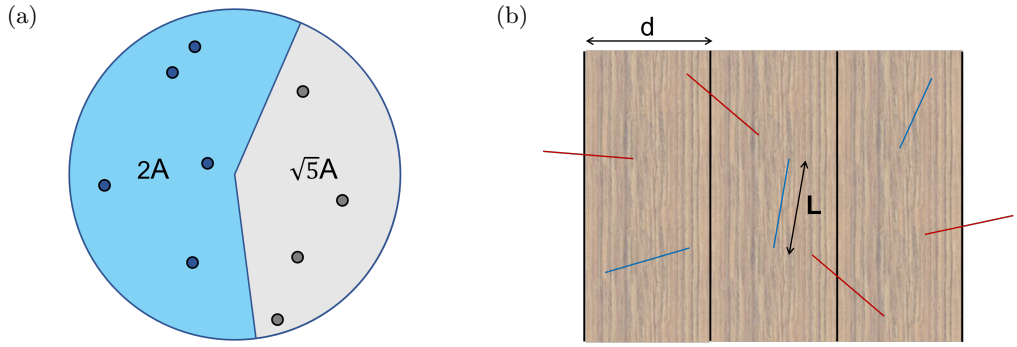

Figure 1.1: (a) Newton's ball problem. A ball is randomly thrown to a circle divided in two sectors whose areas have a ratio of 2 over $\sqrt{5}$. What is the probability that the ball ends up in one of the two sectors? (b) Buffon's needle problem. A needle is randomly thrown on a wooden floor made of parallel floorboards. What is the probability that a randomly thrown needle touches one of the floor edges?

Later on, in 1733 the French mathematician Buffon [19] formulated the classic needle problem to know the probability that a randomly thrown needle touches the edge of a wooden floor made of parallel floorboards (fig. 1.1b). He showed that the intersecting probability is $P = L/2\pi d$, where L is the needle length and d the width of the floorboards. It is noteworthy that this simple experiment allows us to estimate the fundamental mathematical constant of π. More than one century later, in 1860, another French mathematician whose name is Joseph Barbier [20], extended Buffon's result to the expected number of intersections between parallel lines and finite smooth curves.

The examples described above represent rather quite simple and curious problems that demonstrate that relevant geometric information can be obtained from the random intersection of a bounded region and basic geometrical objects such as lines, segments, curves or closed-loop trajectories. This triggered the development of a new branch of mathematics named geometric probability. This discipline, also called stochastic or integral geometry [16], studies the link between expectation of random variables and geometrical quantities such as lengths, areas perimeters, etc. Today it has become a powerful tool for different fields of research, such as steorology [21], nuclear physics [12], image analysis [22] and recently in biophysics for the study of animal behavior [14].

1.3 Cauchy's formula and extensions

1.3.1 Cauchy's theorem

One of the most remarkable results from geometric probability is the mean chord length theorem, proved by Cauchy in 1850 for the convex case [1]. Let us remind this elegant result:

Theorem 1. *If a convex shape of area A and perimeter P is crossed by random and uniform distributed lines, the mean chord length $< L >$ is proportional to the ratio between its area and perimeter. More precisely:*

$$< L >= \pi \frac{A}{P} \tag{1.1}$$

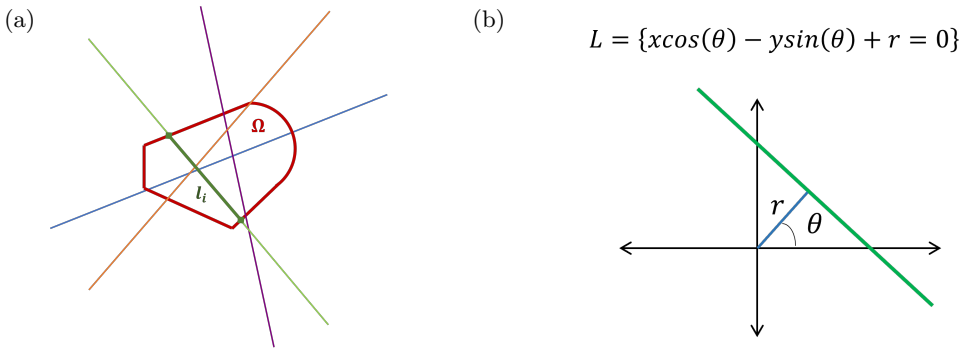

Figure 1.2: (a) Some random distributed lines intersecting a convex region. (b) Parametric representation of a line using an orthogonal coordinate $r \in \mathbb{R}^+$ and a rotation angle $\theta \in (0, \pi)$

Proof. Let us consider N uniformly random distributed lines $L = \{l_1, l_2, ..., l_N\}$ intersecting a convex region Ω (see fig. 1.2a). Any line $l_i \in L$ can be totally defined by two parameters: an orthogonal coordinate $r \in \mathbb{R}^+$, and a rotation angle $\theta \in (0, \pi)$ (see fig. 1.2b). In the limit of $N \to \infty$, the random lines will uniformly cover the region Ω. Then, this is equivalent to placing families of parallel lines with a random direction associated to the angle θ (see fig. 1.3).

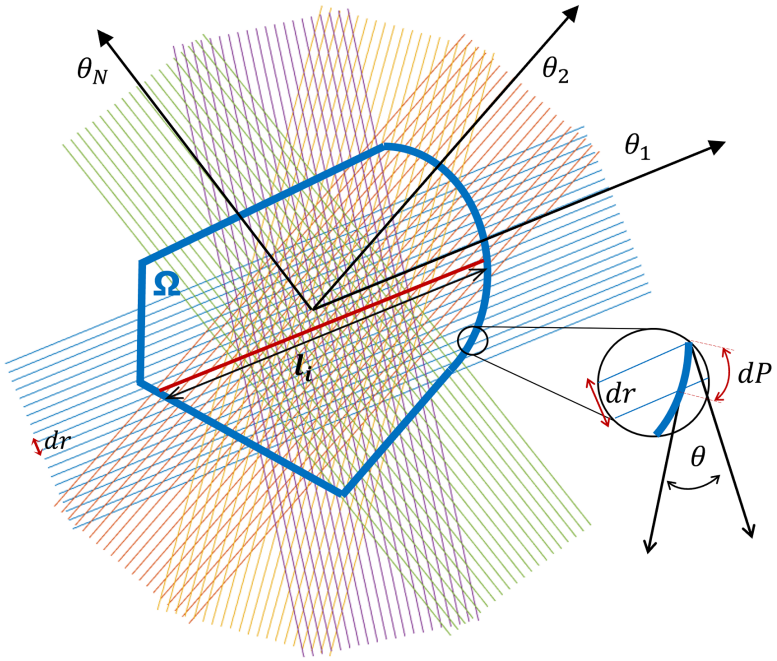

.

Figure 1.3: Equivalence of Cauchy's problem. A convex region Ω is intersected by multiple parallel beams of lines having an infinitesimal separation dr pointing at an arbitrary rotation angle $\theta \in (0, \pi)$

The mean chord length is $< l >= \frac{1}{N}\sum_{i=1}^{N} l_i$, with $l_i \in L$. The sum can be performed by adding each family of parallel lines of corresponding angle θ, whose separation is dr. Then, in the limit $N \to \infty$, the mean chord length is given by the integral:

$$< l >= \frac{\iint_{L\cap\Omega} l\, dr\, d\theta}{\iint_{L\cap\Omega} dr\, d\theta} \tag{1.2}$$

From figure 1.3 one can observe that the numerator of the previous equation corresponds to the area of the region Ω multiplied by π. By using the inset of figure 1.3 it is easy to see that a portion of the shape's perimeter dP crossed by two parallel lines satisfies the relation: $dr = dP\cos\theta$, then:

$$< l >= \frac{\pi A}{\frac{1}{2}\int dP\, \cos\theta d\theta} = \frac{\pi A}{P} \tag{1.3}$$

Where a factor $\frac{1}{2}$ has been placed in the denominator of the last equation because each line cross two parts of the boundary of the convex region Ω. This is a simple demonstration of Cauchy's formula for the mean chord length in 2D. This formula can be extended to

any dimension on space [23]. For instance, in the 3D case we have $< l >= \frac{4V}{A}$, for which a demonstration based on physical principles can be found in [24].

Surprisingly, this formula was also found by Paul Dirac and Klaus Fuchs in 1943, when they were working on the Manhattan Project. They discovered that the mean chord of a piece of fissile material is a crucial parameter for the functioning of a nuclear reactor [11]. This emphasized the physical relevance of this invariant, and later on, it found applications to other fields of research such as in stereology [21], to obtain global geometric information of arbitrary shapes, or in radiology [25], because the mean absorbed radiation of an isotropic radiating beam depends on its average traveled length in a body organ [26].

1.3.2 The Bertrand paradox

Cauchy's mean chord length formula demonstrated the power of geometrical probability to find important geometrical parameters by taking the average of random distributed variables. However, in 1889, another French mathematician named Joseph Bertrand [27] showed that the way we define a random distribution can lead us to different results of a given geometric probability problem. To illustrate this statement, let us evaluate the mean chord length of a unitary circle that is crossed by two different random distributions of lines (see fig. 1.4). On the one hand, let us consider lines defined in the parametric form by an orthogonal coordinate $r \in \mathbb{R}^+$, and a rotation angle $\theta \in (0, \pi)$. This corresponds to Cauchy's definition, then $< L >= \pi/2$. On the other hand, let us consider lines from a random point of the circle's boundary and having an arbitrary direction. By performing the numerical simulations of these two scenarios, we notice that the chords are not distributed in the same way over the circle. We can plot the corresponding mean chord length as a function of the number of crossing chords as it is shown in figure 1.4c, where we can observe that for the second distribution the mean chord length converges towards $< L >= 4/\pi$, which can also be obtained analytically [27].

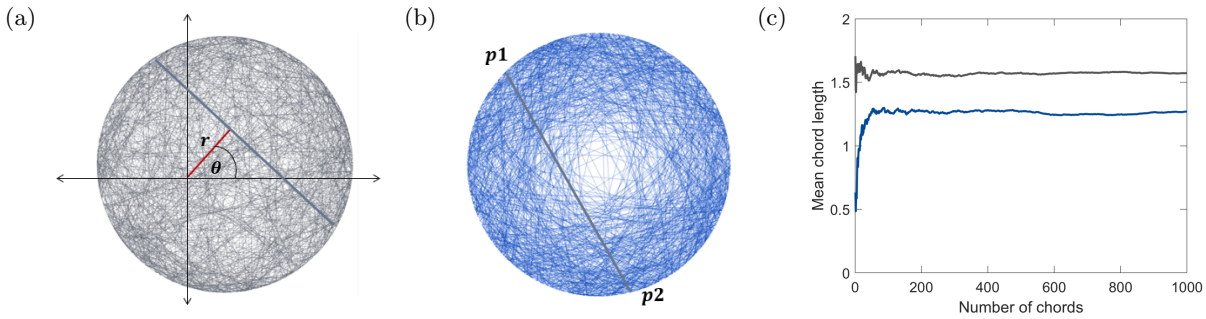

Figure 1.4: Illustration of Bertrand's paradox. The way we define randomness can lead us to different results. Intersection of a unitary circle with (a) random chords belonging to the lines defined by $(r, \theta) \in \mathbb{R}^+ \times (0, \pi)$ or (b) chords created from two random points p_1 and p_2 of the circle's boundary. (c) Corresponding mean chord length as a function of the number of chords for both scenarios.

Betrand's paradox is only a warning for the way we define a random distribution. In modern terms, a probability distribution is associated to a measure whose integral over some subspace of a measurable space corresponds to the probability for some event to take values in this subset [28]. Bertrand pointed out in 1888 that the use of the uniform measures on three different parameter spaces provides different answers [29]. By comparing the figures 1.4a and 1.4b, we can notice that only the first figure has a uniform distribution of lines without concentration on the boundary. Moreover, this distribution is invariant under rigid transformations, which is not the case for the second defined random distribution. In the following, we are going to consider only uniform random distributions that do not present a bias or preferential positioning in the space. The probability density function corresponding to this rigid invariant random distribution is called the kinematic density (see Appendix A).

1.3.3 Non-convex shapes and Brownian motion

In the previous section, the demonstration of Cauchy's formula was done by considering random and uniformly distributed lines that intersect a convex object in 2D. A natural question that arises is whether this formula remains valid for non-convex shapes or random trajectories intersecting an arbitrary domain. Examples of such scenarios are shown in figure 1.5. These questions have been already addressed in [2] and [13]. In these studies, they showed that Cauchy's formula holds for non-convex shapes, if we take the chords independently. Moreover, they also found that this invariance remains valid in the case of random trajectories, provided that they are uniformly starting from the boundary of the domain. This last result represents a

remarkable property because the mean traveled length $< l >$ in any bounded region depends only on its geometrical properties, and not on the specific details of the trajectory. Experimentalists from diverse fields of research have tested this property, for instance, biologists have verified it with different moving organisms, by measuring their mean traveled length on an explored region [14, 30]. Additionally, this result has been also verified with electromagnetic waves that are scattered by a complex medium [15], [31].

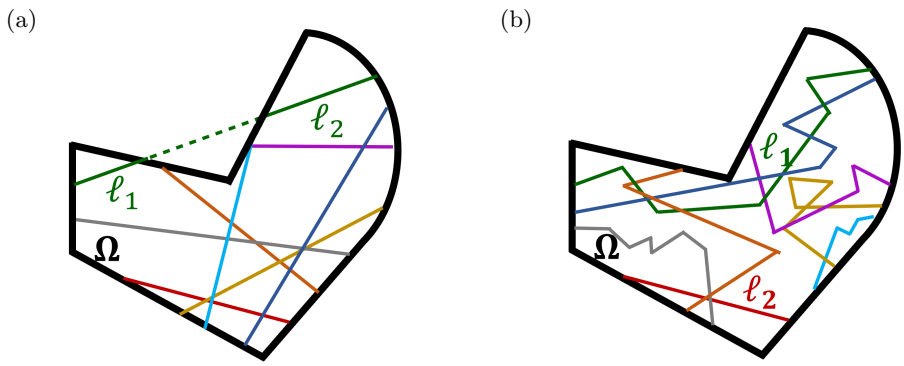

Figure 1.5: Generalization of Cauchy's formula. The mean chord length theorem is also valid in the case of non-convex regions (a) and Brownian trajectories (b). The only condition is to consider each crossing path l_i separately, even if they belong to the same trajectory.

1.3.4 Mean crossing length for finite trajectories

In the previous sections we considered trajectories entirely crossing the explored region. Another interesting problem would be the case of trajectories whose length is finite and curved. A typical physical system could be charged decaying particles placed in a magnetic field. Let us suppose that these particles can be randomly created in any point of the space and move a portion of arc of fixed length L. We can perform a numerical simulation of such a system where the explored region is a disk of radius R. In figure 1.6a we show four different simulations of the semicircular trajectories with four different lengths L normalized by the disk radius R. In figure 1.6b we plot the normalized mean arc length as a function of this parameter. The heuristic formula indicated in black fits well the trend of the mean arc length in this simple case, but for the case of more complex trajectories it is not easy to find a simple mathematical expression. The asymptotic limit corresponds to the Cauchy formula. This limit is expected because the crossing trajectories become straight lines as the curvature

decreases. Inversely, we notice that the mean arc length decreases as the arc length L decreases, demonstrating that Cauchy's theorem is not valid for finite open curves. In the next section we will analyze the case of finite closed-loop trajectories.

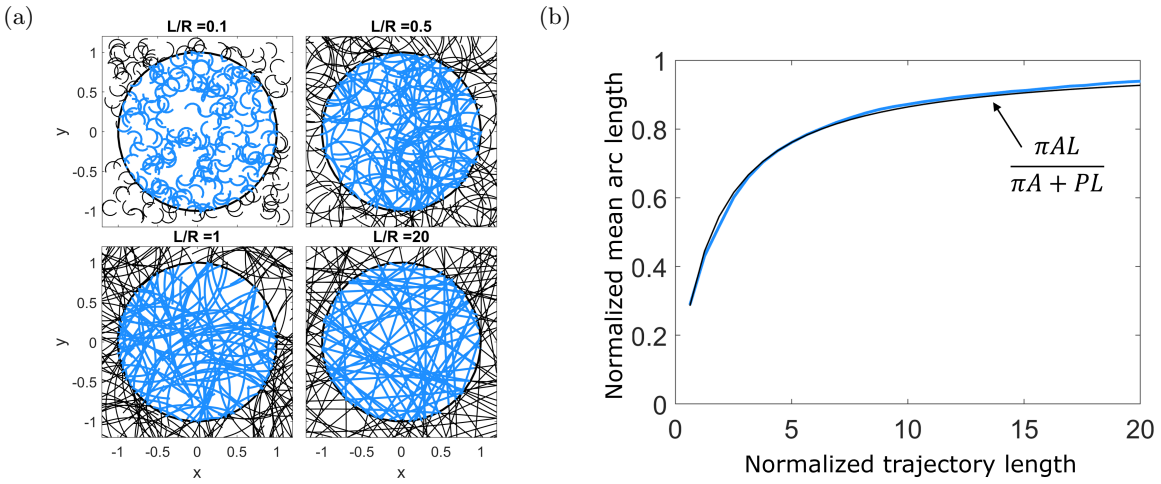

Figure 1.6: Mean arc length for half circular trajectories randomly intersecting a disk. (a) Four snapshots are shown for different aspect ratios between the arc length L and the disk radius R. (b) Normalized mean arc length as a function of the normalized trajectory length. Cauchy's formula is the asymptotic limit for arbitrary large trajectories. The heuristic formula shown in black, where P and A are the perimeter and area respectively, fits well the trend.

Mean arc length for circular trajectories

Until now, we have seen that Cauchy's formula remains valid also for random trajectories that are uniformly distributed and completely cross a bounded domain [3], otherwise, the mean crossed length decreases as a function of the trajectory length, as shown in fig. 1.6b. Another interesting case to study could be if instead of having open trajectories, we consider closed contours of finite length that randomly intersect an arbitrary bounded domain. This problem has not yet been addressed in the literature and will be studied in the following section. In this scenario, one can be interested in knowing the mean arc length and comparing it to Cauchy's formula. One can expect that if the closed-loop trajectories enclose an area which is much larger than the area of the explored domain, the mean arc length satisfies the Cauchy formula. Inversely, if the closed loop trajectories enclose an area much smaller than the explored region, the mean arc length must be close to the contour perimeter. Then, the mean arc length strongly depends on the closed-loop trajectory size, and this is going to be addressed throughout this section.

The simplest closed contours are circular trajectories, and they receive a particular interest since circular motion is ubiquitous in nature. For instance, it can be performed by electrons moving in a constant magnetic field, swimming microorganisms [32] or robots [33]. We are going to study the case of circles exploring convex and non-convex domains, separately. Numerical simulations are used to analyze the evolution of the mean arc length as a function of the size of the circular trajectories. We consider two arbitrary regions where circles of fixed radius R are randomly placed. The first region corresponds to the convex hull of the map of France and the second one is the non-convex map of Mexico.

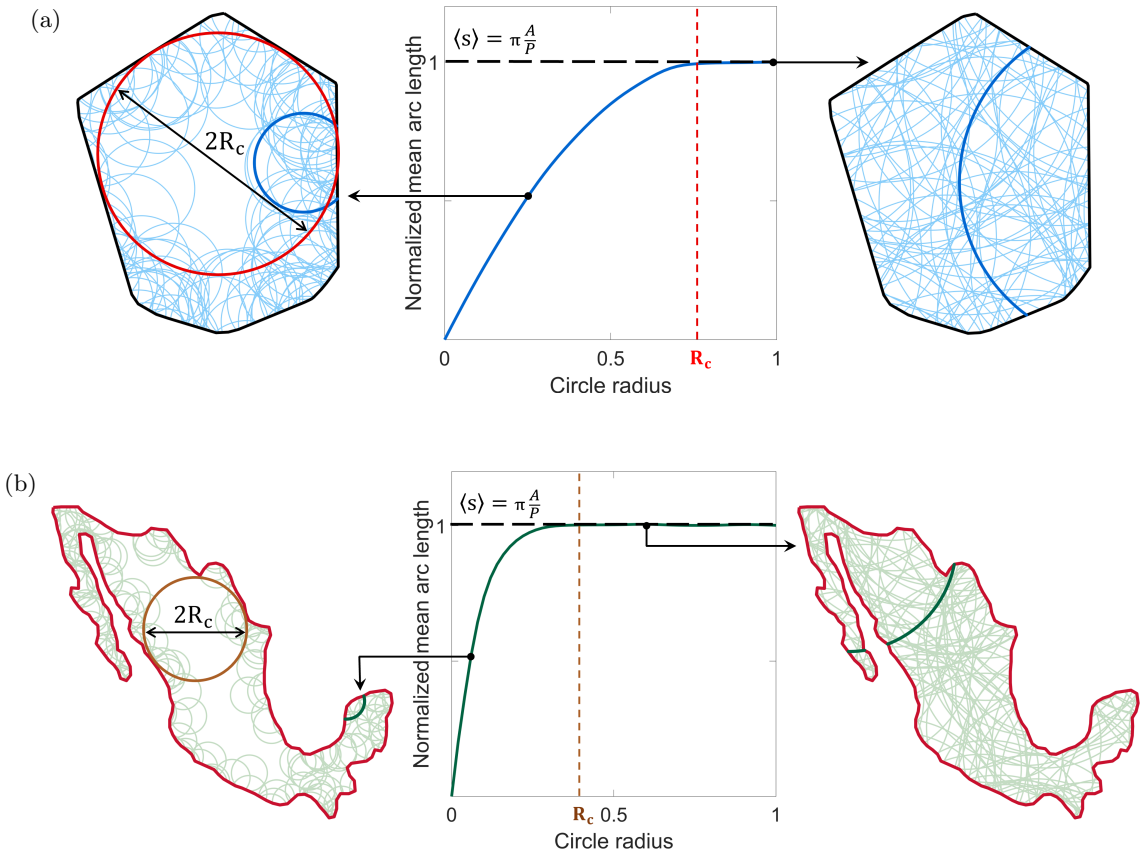

Figure 1.7: Mean arc length for circular trajectories exploring convex and non-convex regions. Circles of fixed radius R randomly explore (a) the convex hull of the map of France and (b) the non-convex shape given by the map of Mexico. In both cases, the mean arc length coincides with Cauchy's formula for trajectories whose radii are bigger than the one corresponding to the largest inscribed circle in the explored region.

Numerical simulations are performed with 10^6 circular trajectories of fixed radius that randomly intersect the domains depicted in figs. 1.7a and 1.7b, respectively. Figure 1.7a shows the evolution of the mean arc length s as a function of the radius R for circular trajectories that randomly intersect the convex hull of the map of France.

On the left of figure 1.7a we plot some intersecting arc lengths colored in blue, for trajectories of a fixed radius R smaller than the largest inscribed circle R_c (red circle). Similarly, on the right, we plot a random exploration with trajectories having a radius $R > R_c$. The numerical simulation shows that the mean arc length $s(R)$ increases from zero until reaching a plateau above a critical radius R_c which corresponds to the radius of the largest circle that can be totally inscribed in this convex domain. Surprisingly, for all the trajectories where $R > R_c$, the mean arc length verifies the Cauchy formula $s(R) = \pi A/P$ (horizontal dashed line). We remind that in the case of finite open trajectories, the Cauchy formula was only an asymptotic limit for large trajectories. Thus, this is a new remarkable property of closed contours.

In fig 1.7b, we plot the results for the case of randomly distributed circles exploring the non-convex region represented by the map of Mexico. On the left we show an example of intersecting arc lengths, colored in green, for trajectories of radius R smaller than the largest inscribed circle R_c (brown circle). On the right, we show a case where the trajectories have a radius $R > R_c$. We find a similar evolution, compared to the previous case, for the mean arc length s as a function of the radius R for intersecting circles.

From these simulations, we have verified numerically that Cauchy's formula can be extended to circular trajectories of finite length, provided that their radius is larger than the radius of the largest inscribed circle in the domain. Now let us see what happens with more complex trajectories.

1.3.5 Mean arc length for closed-loop trajectories

In order to acquire an intuition for the case of complex closed-loop trajectories, we perform more simulations for these types of contours that are randomly crossing an arbitrary domain. Figure 1.8 shows two domains having the shape of a chess Rook and Pac-Man, respectively. These domains are crossed by randomly distributed trajectories having the shape of a chess Knight (fig. 1.8a) and of a Ghost (fig. 1.8b), respectively. In figure 1.8c, we plot the normalized mean arc length, for both cases, as a function of the ratio of the contour area over the region area.

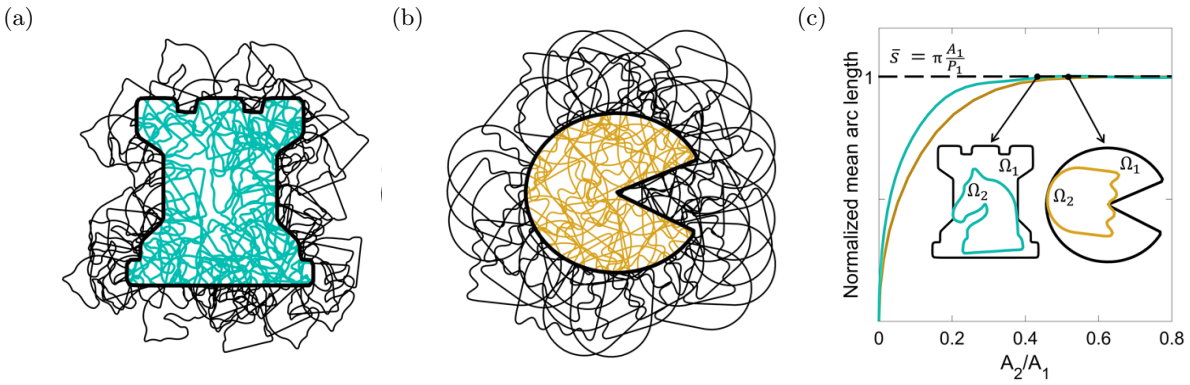

Figure 1.8: Examples of exploration of domains in the shape of (a) the chess Rook and (b) a PacMan with trajectories in the shape of a chess Knight and a Ghost respectively. (c) Evolution of the corresponding normalized mean arc length as a function of the relative areas of the two domains A_1/A_2. The inset figures show the largest fully inscribed trajectories, and their corresponding point. The horizontal dashed line represents the normalized Cauchy formula.

From the numerical simulations, we observe that the evolution of the mean arc length remains like the one obtained with circular trajectories, recovering Cauchy's formula if no trajectory can be totally inscribed inside the explored domain. This behavior motivated us to demonstrate the following theorem:

Theorem 2. *For random distributed and not fully inscribed closed-loop trajectories crossing an arbitrary region of area A and perimeter P, the mean arc length $< s >$ satisfies the Cauchy formula:*

$$< s >= \pi \frac{A}{P} \tag{1.4}$$

Proof. The proof of this theorem is more technical, requiring several concepts from integral geometry and two auxiliary theorems given by Blaschke and Poincaré [16]. For this reason, the detailed demonstration is found in Appendix A. This is done on purpose to be focused on the physical applications of these powerful mathematical results.

Reciprocal explorations

The closed trajectories also form a closed domain, so the role of the random contours and the explored domain can be interchanged. Let us analyze this scenario with the domains depicted in figure 1.9. One has the shape of an egg (domain Ω_1) and the other the shape of a chicken (domain Ω_2).

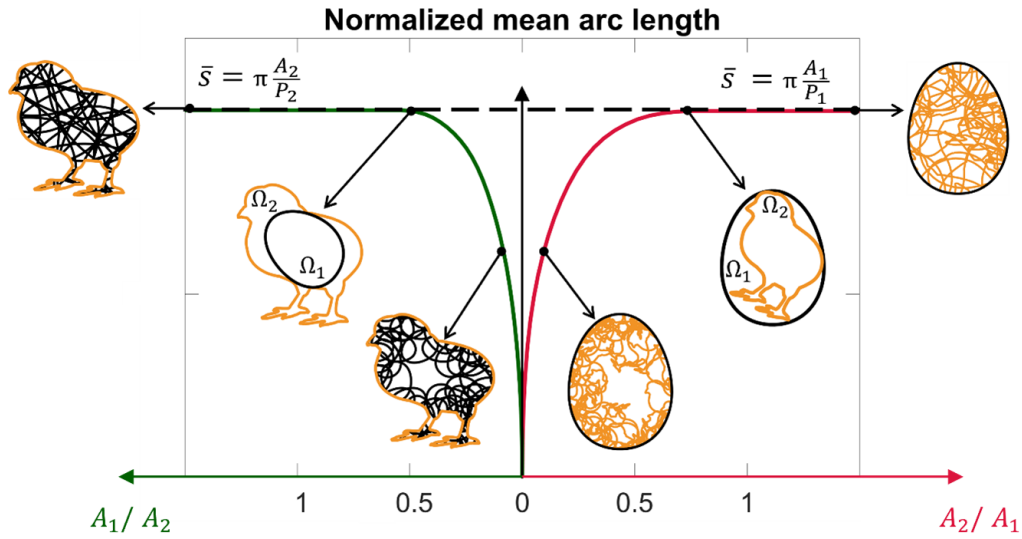

Figure 1.9: Mirrored graphs of the evolution of the normalized mean arc length as a function of the relative area for domains in the shape of an egg Ω_1 and a chicken Ω_2 explored by 10^5 random contours $\partial\Omega_2$ and $\partial\Omega_1$, respectively. The insets show examples of realizations in the two asymptotic regimes and also the largest fully inscribed contour. The horizontal dashed line indicates the corresponding Cauchy's formula.

First, we can consider the egg-shaped region being crossed by 10^5 random distributed chicken-shaped replicas of area A_1. Then, we can perform the reciprocal exploration, where a chicken-shaped region is crossed by 10^5 random distributed egg-shaped replicas of area A_2. The mirror plots shown in 1.9, illustrate the evolution of the normalized mean arc length as a function of their area ratio. Both curves are qualitatively similar to the ones previously presented with a steady increase from zero to a plateau satisfying the generalized Cauchy's formula $s = \pi A_i/P_i$, where A_i and P_i are the area and perimeter of the explored domain $i = 1, 2$, respectively. The mean arc length increases as a function of the closed-loop trajectory size and a plateau, corresponding to Cauchy's formula, is reached for trajectories greater than the largest inscribed one.

Thus, by performing a random exploration of an arbitrary domain with arbitrary closed-loop trajectories, we are able to get relevant information regarding the maximum size of the scaled contour that can be fully inscribed in the domain. We can compare this analysis with Hadwiger's criterion [34, 35]. This gives a sufficient condition for a domain Ω_1 of area A_1 and perimeter P_1 to be contained into a second domain Ω_2 of area A_2 and perimeter P_2. If their areas and perimeters verify the following inequality: $2\pi(A_1 + A_2) - P_1P_2 > 0$, then the smallest domain can be totally inscribed in the second domain. However, this is only a sufficient but not necessary condition [16]. In our case, thanks to a random sweeping through the replicas of a second domain, we can predict

exactly when one of the regions can be fully inscribed in the other. This result can be useful for studies of packaging optimization.

1.4 A new invariant for straight motion

Cauchy's formula is one of the major achievements of geometric probability that is valid even for arbitrary trajectories that randomly cross a domain. This important result gives us the ratio of the area to the perimeter of a region in 2D or the ratio of the volume to the area of a domain in 3D. However, this invariant is not enough to obtain the area and perimeter, or the volume and area, separately. Then, we need a second formula or invariant from a random exploration, in order to estimate these geometrical parameters. In this section we will introduce a second invariant for the case of straight motion. A second formula was discovered by M. Crofton [36] but, unfortunately, it is only valid for convex shapes. Here, we will introduce a more general invariant that simplifies to Crofton's formula if the explored domain is a convex shape.

1.4.1 Crofton's theorem

Important developments of geometric probability are also due to a British mathematician named Morgan Crofton [19], he introduced the notion of measure for the set of random distributed lines that intersect an arbitrary domain in 2D [16]. By using this concept, he found another way to demonstrate Cauchy's formula and, later on, this allowed him to find a second invariant for the case of convex sets. Let us recall this remarkable result:

Theorem 3. *For any convex region $\Omega \in R^2$ of area A and perimeter P crossed by random and uniform distributed lines, the third moment of the chord length distribution $< L^3 >$ is:*

$$< L^3 >= 3\frac{A^2}{P} \tag{1.5}$$

Proof. The demonstration of this important theorem is found in B (obtained from [16]).

1.4.2 Evaluation of convex shapes

Let us consider a convex shape in 2D of area A and perimeter P, which is crossed by random and uniform distributed lines. The mean chord length is given by Cauchy's

formula: $< L >= \pi A/P$. The third moment of the chord length distribution is given by Crofton's formula: $< L^3 >= 3A^2/P$. Then, if we divide both equations we obtain:

$$A = \frac{\pi < L^3 >}{3 < L >} \tag{1.6}$$

In addition, if we divide Crofton's result by the square of Cauchy's formula we get:

$$P = \frac{\pi^2 < L^3 >}{3 < L >^2} \tag{1.7}$$

1.4.3 Limitations of Crofton's formula

Crofton's formula relates the third moment of the chord length distribution of a convex domain to its area and perimeter. One can wonder if this formula is also valid for non-convex regions. A simple counter example would shatter any hope for this generalization. Let us consider an annular region whose inner and outer radii are $R_1 = 1$ and $R_2 = 2$, respectively (see fig. 1.10a). According to Crofton's formula, the expected third moment is $< L^3 >= 3[\pi(4-1)]^2/(2\pi(2+1)) = 9\pi/2$. One can perform a numerical simulation to evaluate the third moment of the chord length distribution. This is shown in fig. 1.10b, where we observe that $< L^3 > \neq 9\pi/2$. This simple counterexample shows that Crofton's formula does not apply to non-convex regions.

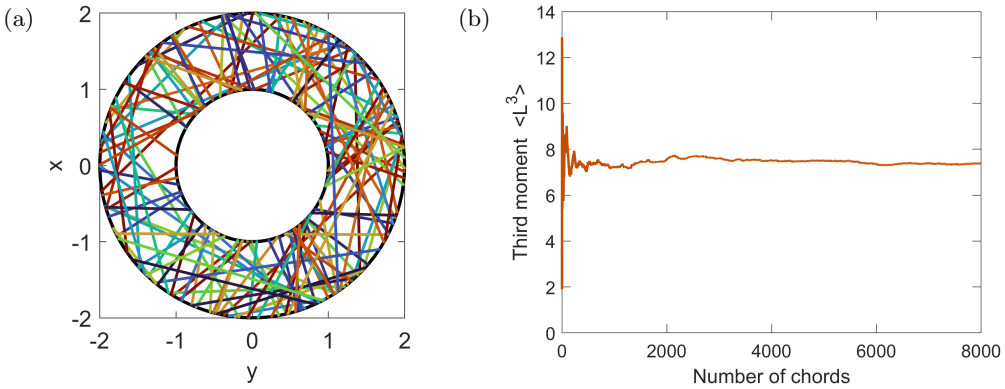

Figure 1.10: Crofton's formula does not apply to non-convex shapes. A simple counterexample is given. (a) Uniformly distributed random chords in an annular region. (b) Third moment of the chord length distribution as a function of the number of crossing chords. The plateau value differs from the one predicted by Crofton's formula.

1.4.4 A new invariant for non-convex regions

Until now, we have shown that the random crossing of a convex region by straight lines can give us a direct estimation of its area and perimeter. However, this cannot be generalized for arbitrary regions because only Cauchy's formula is also valid for non-convex shapes. Here, we will introduce a more general invariant for the case straight-line motion randomly intersecting non-convex domains in 2D. Instead of using the chord lengths, we consider the lengths for all the possible segments given from each crossing line (see fig. 1.11). In Appendix C we demonstrate the following theorem:

Theorem 4. *Let us consider an arbitrary region $\Omega \in \mathbb{R}^2$ of area A and perimeter P, which is crossed by randomly distributed lines. A point belonging to a line L is identified by its curvilinear abscissa ℓ along the line. For every crossing line we enumerate the points where the line enters and exits the domain. We denote by $(e_i)_{i=1...N}$ the entrance points and by $(s_i)_{i=1...N}$ the exit points, as shown in fig. 1.11. The following relation is verified for any arbitrary shape:*

$$\beta = \frac{\langle \sum_{k,j} |s_k - e_i|^3 - \sum_{k,j} |s_k - s_i|^3 - \sum_{k,j} |e_k - e_i|^3 \rangle}{\langle \sum_{k,j} |s_k - e_i| - \sum_{k,j} |s_k - s_i| - \sum_{k,j} |e_k - e_i| \rangle} = \frac{3A}{\pi} \tag{1.8}$$

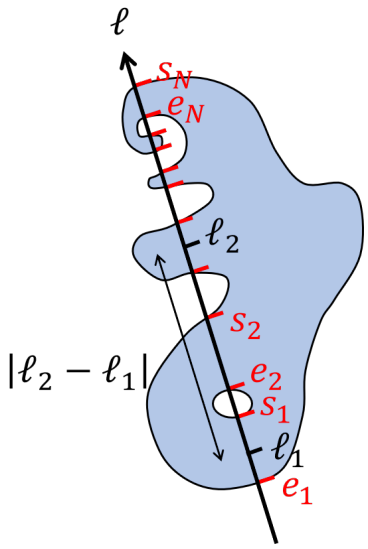

Figure 1.11: A non-convex shape crossed by a line. A point belonging to this line is identified by its curvilinear abscissa ℓ. We denote by $(e_i)_{i=1...N}$ the entrance points and by $(s_i)_{i=1...N}$ the exit points.

Proof. The demonstration is given in the Appendix C.

One can note that in the case of convex regions, the left member of eq. 1.8 simplifies to the ratio between Crofton and Cauchy formulas. Then, we can demonstrate Crofton's theorem from this new invariant.

1.4.5 Evaluation of non-convex shapes

Let us consider now a non-convex shape in 2D of area A and perimeter P, which is crossed by random and uniform distributed lines. From the new invariant denoted β in eq. 1.8 we have:

$$A = \frac{\pi\beta}{3} \tag{1.9}$$

We can use this result in Cauchy's formula, which is also valid for non-convex shapes. Then, the perimeter is obtained:

$$P = \frac{\pi^2\beta}{3 < L >} \tag{1.10}$$

1.5 Application to shape recognition

Many branches of science need to measure, analyze and recognize geometrical objects. For instance, the main goal of radiology is to evaluate the health state of an organ and look for a characteristic shape of a well-known pathology (see fig. 1.12). There exist different physical methods that are implemented worldwide, most of them use ultrasound or electromagnetic beams to perform the analysis. These techniques require an oriented evaluation of the shape and employ cross sections in different directions to fully reconstruct the region of interest [37]. This is possible through the use of certain mathematical methods, for example, the Radon transformation [38].

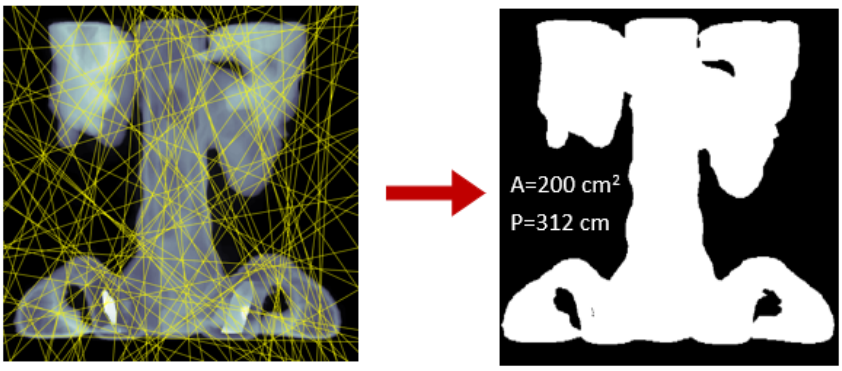

.

Figure 1.12: X-Ray beams intersecting the cross section of a non-convex region. Area and perimeter measured by processing the binarized image and using a scale factor

If we cannot get a full reconstruction of the analyzed shape, the global geometric characteristics such as the area and the perimeter of the object in 2D, or its volume and surface in 3D, provide useful information of interest for many practical applications. This problem can be addressed from the point of view of geometric probability, without the need of a sophisticated technology to fully reconstruct the region of interest.

Thanks to the application of the formulas shown in the previous sections, we will see that any arbitrary shape can be evaluated by means of a random ballistic exploration. Moreover, once we find the area and perimeter of the explored region, we can define a simple way to distinguish a shape from other ones taken among a list of known objects (a shape dictionary). The analysis will be done for regions in 2D but this can be extended to 3D by replacing the corresponding equations for the statistical invariants, in the same way as it has been done for Cauchy and Crofton formulas in [39].

1.5.1 Experimental implementation

An interesting field of application for these powerful statistical results could be robotics. A simple disoriented robot could now measure any arbitrary shape thanks to a random exploration. This strategy can be implemented with simple robots, who can have small memory capabilities, simple mechanical motion, and only a few sensors to interact with the environment. Due to their simplicity, these kinds of robots have been intensively used to study collective phenomena under multiple configurations [40–43]. In figure 1.13, three examples of small robots are depicted. In fig. 1.13a, we show a

hexbug. This 4 cm size robot is made of a small vibrator connected to battery and a soft asymmetric mechanical support. It converts the vibrations into a propelling force. In fig. 1.13b, we show a M5Stick-C robot, which is a 5 cm size robot made of a Esp32 microcontroller connected to a mechanical support that has 4 rotating motors. The speed and direction of each motor can be individually controlled to generate complex motion. In addition, this robot can be customized, for instance, by placing a boundary detector and a light intensity sensor on the top. In fig. 1.13c, we show a kilobot, which is a 3 cm size robot who has a simple mechanical support made of 3 fixed legs. It employs 2 vibrators connected to a battery to generate different types of motion. An infrared sensor and a light sensor are added to be programmed and communicate with other robots.

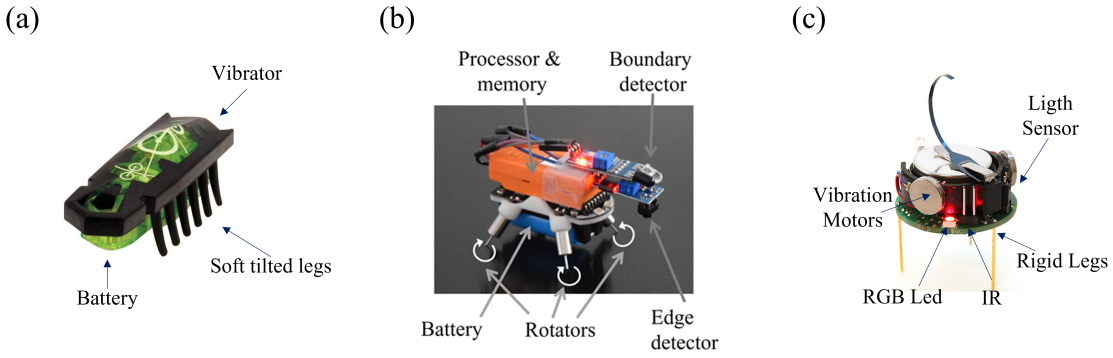

Figure 1.13: Some robots employed in physics. (a) A hexbug. This is a 4 cm size robot made of a small vibrator connected to battery and a soft asymmetric mechanical support. It converts the vibrations into a propelling force. (b) A M5Stick-C robot. This is a 5 cm size robot made of an Esp32 microcontroller connected to a mechanical support that has 4 rotating motors. The speed and direction of each motor can be individually controlled to generate complex motion. Some sensors can be added, in this case a boundary detector and a light intensity sensor. (c) A Kilobot. This is 3 cm size robot which has a simple mechanical support made of 3 fixed legs. It employs 2 vibrators connected to a battery to generate different types of motion. An infrared sensor and a light sensor are added to be programmed and communicate with other robots.

Initially, we started the experiments with a Kilobot and also a M5Stick, but we they cannot perform straight-line motion during a long period of time. According to our recognition strategy, we need a random oriented ballistic motion to be able to employ the formula presented in equation 1.8. Otherwise, the mean chord length theorem is the only statistical invariant also valid for random motion. In this case it would correspond to the mean path length traveled within the surface. Unfortunately, this only gives us a ratio between its area and perimeter, without retrieving both parameters separately. The only solution was to find a robot able to perform straight-line motion. To achieve

this, it needs to use motor encoders for controlling the velocity on each side of the robot. We found a perfect candidate for such a task, and this is the commercial robot named Sphero (see www.sphero.com for more info). Due to its easy programming environment based on JavaScript and the presence of few sensors, this robot has been used for physics and electronics demonstrations during the last years [44], [45]. A picture of this robot is shown in (fig. 1.14a). The Sphero is a 7 cm size robot in the form of a transparent robotic ball whose internal technology can be seen through its acrylic shield. It has two motor encoders who are capable of performing an almost perfect straight-line motion. It also has a 2mm diameter light sensor, an internal clock and an accelerometer. The built-in battery can be charged with an inductive-based charger and its base has to be connected through a USB port. Depending on the working speed, this robot can be moving during a time ranging from 1 to 4 hours.

We decided to use the sphero robot because it has several features that make him an appropriate robot to be working with. Let us highlight some of them. It is constructed with a strong polycarbonate shell that resists impacts. The working speed can be programmed between 1 to 50 mm/s. It has a Bluetooth connection with a range of 30 meters, allowing it to communicate with a computer or any smart device. It has internal multicolored LEDs. It is programmable through many programming languages based on intuitive blocks, but also on JavaScript.

1.5.2 Experimental setup

We project different convex and non-convex figures on the floor with an overhead illumination sent by a video projector. The robot is restricted to move in a bounded arena much larger than the projected figure size. Then, the robot performs a series of uncorrelated straight motions in this arena. An example of a random exploration of an Eiffel tower is shown in fig. 1.14. After calibrating the light sensor, the robot can detect whether it is inside or outside the projected shape. It records the time spent within the region and it is converted to a series of chord lengths $l_1, l_2, ...l_n$ for each crossing line (see fig. 1.14a), then, it randomly changes the orientation to generate a new straight motion and start the process again. Thanks to a simple algorithm, which is detailed below, the robot is able to perform a recognition of the explored shape among a list of previously stored shapes (see fig. 1.14b).

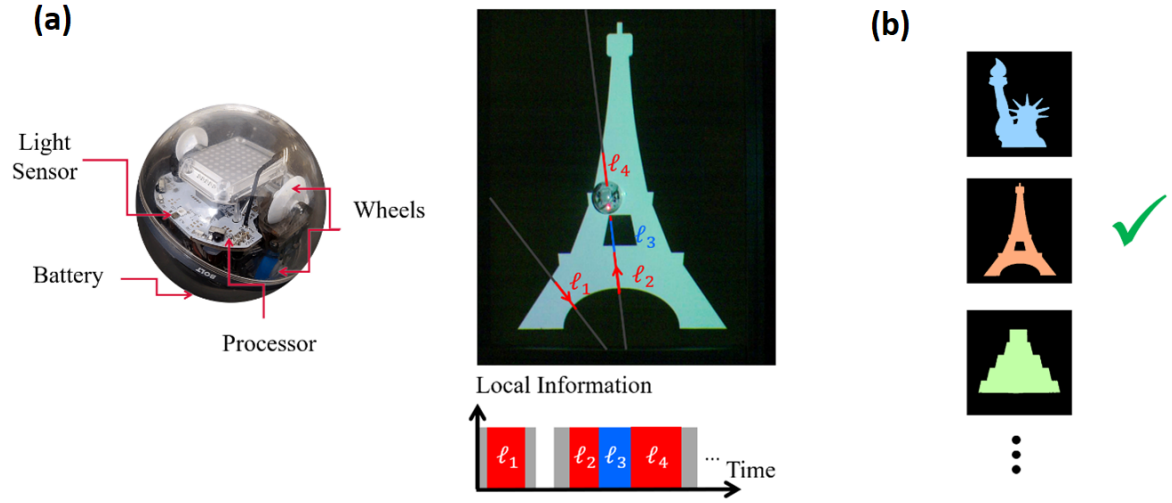

Figure 1.14: Experimental implementation of shape recognition with a simple sphero robot. (a) Main components of the Sphero robot and examples of two random crossing lines with their decomposition in inner (red) and outer (blue) chords. (b) Recognition strategy by comparison of the measured area and perimeter with the corresponding values of the stored shapes.

The robot light sensor is programmed to flash its built-in LED when it is inside of the projected region. In order to verify the uniform distribution of the robot's presence within the region, an external camera is placed on the top and it records the robot's motion during the whole exploration, which lasts about 4 hours. For each exploration consisting of one thousand crossing lines, we superpose the frames taken every 10 s. This is shown in (fig. 1.15), where we can observe a uniform distribution of the light dots, corresponding to a uniform exploration of the regions by means of the random oriented straight motion performed by the robot.

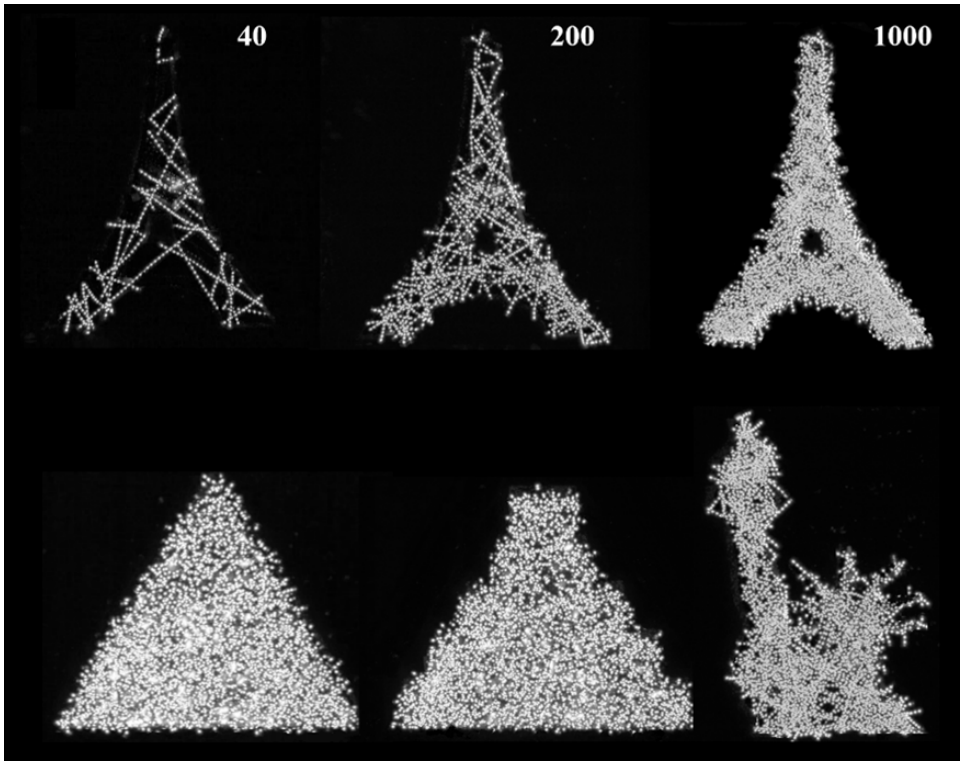

Figure 1.15: Superposition of robot's led position that flashes when the robot is inside the explored region. These images were taken with an external camera to verify the uniformity of robot's presence on the explored shape. On the top, we show the superposition of 40, 200 and 1000 lines intersecting the Eiffel tower silhouette. On the bottom, we show the superposition of 1000 lines intersecting a triangle, a pyramid and a statue of Liberty, respectively.

1.5.3 Shape recognition strategy

The area and perimeter are simple geometrical parameters that can now be estimated for arbitrary regions using the formulas we demonstrated in the previous section. From the recording done with the external camera, we can reconstruct the chord length distribution and compare with the estimation made by the robots and the theoretical one. Only an analytic expression is found in the literature for regular polygons [46]. In the case of non-convex regions, an analytic expression of the chord length distribution is difficult to obtain. However, an approximation can be obtained using numerical simulations. The case of an equilateral triangle intersected by randomly distributed straight lines is illustrated in fig. 1.16a, where we show the comparison of the theoretical probability density function and the experimental histogram for the chord length distributions.

(a) (b)

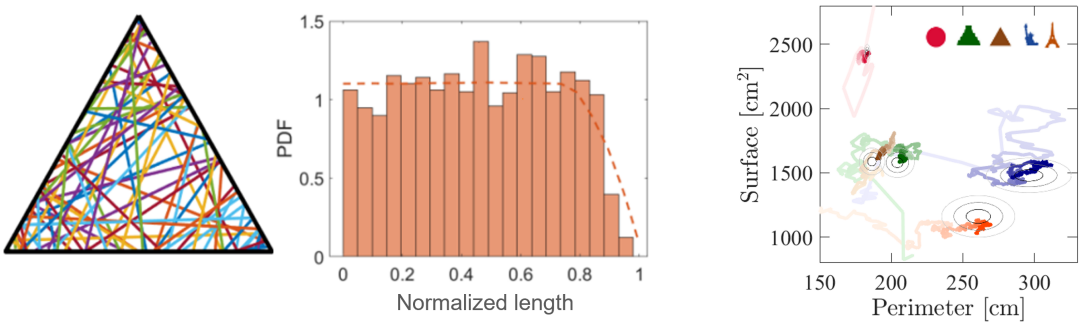

Figure 1.16: Recognition strategy based on chord measurements. (a) Some random distributed lines intersecting an equilateral triangle and the corresponding chord length distribution histogram compared with the theoretical curve (red dashed line). (b) Convergence trajectories for each explored shape in a perimeter-surface representation, as the number of crossing lines N increases (increasing the line contrast). The ellipses represent the statistical confidence limits for 90%, 95% and 99% and they were estimated by Monte Carlo simulations.

For each scanned object we have an estimate of its area and perimeter as a function of the intersecting lines. This can be represented in a Perimeter-Surface color plot, as shown in figure 1.16b for the shapes experimentally projected. A curve of a given darkening color represent the time evolution of the estimated perimeter and surface as we increase the number of crossing lines. The ellipses placed in this plot represent the intervals of confidence with relative errors of $1, 5$ and 10 %, respectively. The statistical confidence was estimated by Monte Carlo simulations. From this plot, we observe that 1000 lines are sufficient to distinguish the experimentally explored shapes within a relative error of less than 10%. At the end of the random exploration, the robot compares the estimated values with the ones stored in its dictionary. For each explored shape present in the dictionary the robot displays on its screen a schematic of the recognized shape. If no shape was recognized, the robot displays a question mark. In figure 1.17, we show the recognition examples for the Eiffel tower, a triangle and a circle.

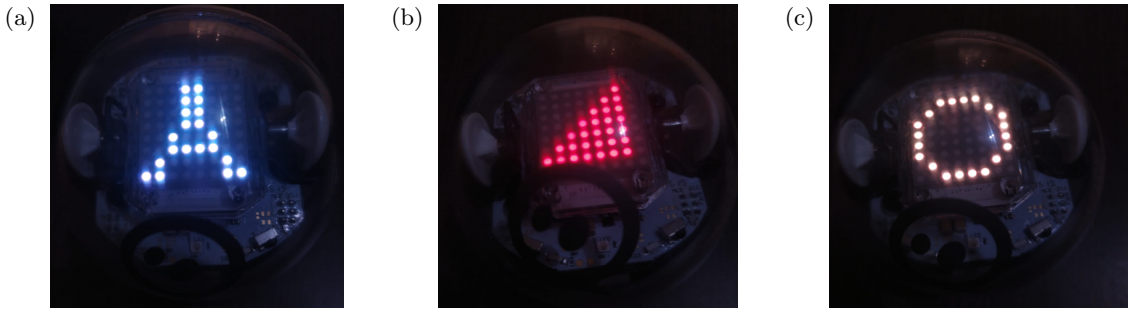

Figure 1.17: Recognition results. After crossing the explored shape with 1000 randomly distributed lines, the sphero's LED matrix draws the shape that was recognized. Here we show the recognition of the Eiffel tower, a triangle and a circle. If no shape was recognized it draws a question mark.

1.5.4 Convergence analysis

The Sphero has a limited memory and cannot store all the chord lengths. Thus, it has to perform an iterative estimation of the region's area and perimeter by using the formulas given in the previous sections. After each time the robot performs a new straight motion, it updates the area and perimeter values by computing the averages corresponding to formulas given in eqs. 1.6 to 1.10. In figure 1.18, we plot in bold solid line the area and perimeter experimentally estimated, as a function of the number of crossing lines. We superpose, in light color, the results obtained from numerical simulations of 100 different starting points.

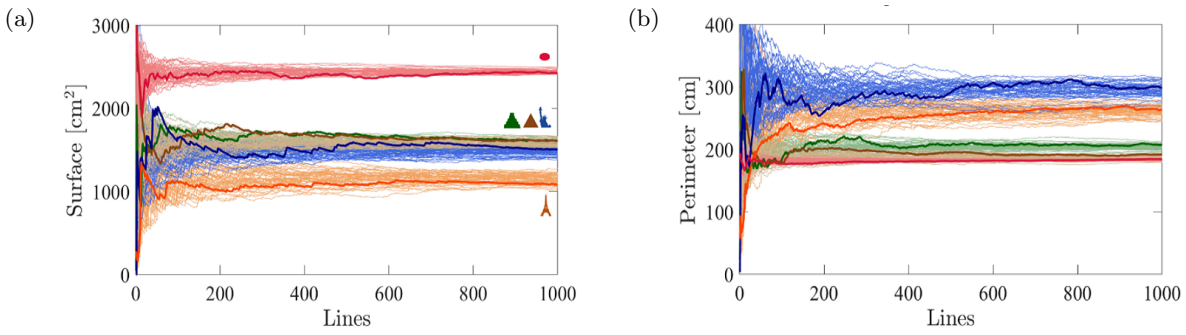

Figure 1.18: Convergence comparison between 100 simulations for each shape and a single robotic implementation. Estimated (a) surface and (b) perimeter as a function of the number of crossing lines

From the numerical simulations we can plot the relative error estimation for the area and perimeter as a function of the number of crossing lines. These errors are plotted in a

logarithmic axis in figs 1.19a-b to show the power law trend.

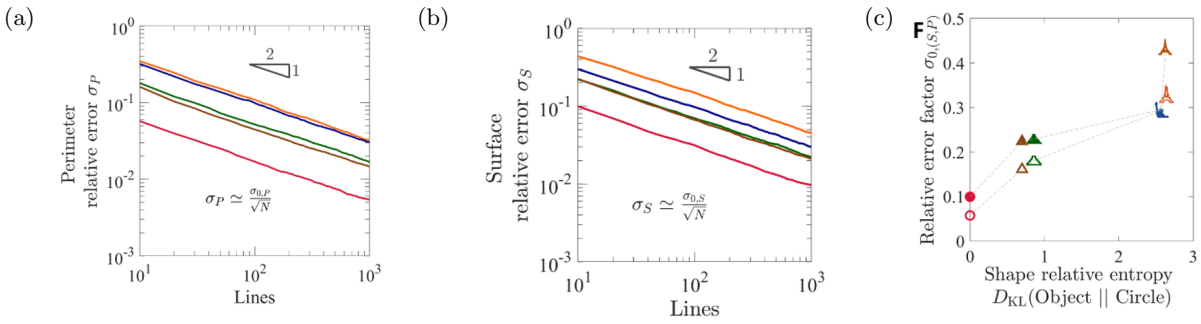

Figure 1.19: Logarithmic plots for the relative error in the estimation of the region's (a) area and (b) perimeter, as a function of the number of crossing lines. The insets show a power law of $-1/2$ with a prefactor depending on the complexity of the region. (c) Relative error as a function of the Kullback-Leiber divergence compared to a circle.

From the previous plots, we observe that the relative error is inversely proportional to the square root of the number of crossing lines, as depicted in the insets of these figures. This trend is expected because the fluctuations should converge as $1/\sqrt{N}$ [47]. The error prefactors for the surface (σ_{0S}) and perimeter (σ_{0P}) represent the initial relative error of the corresponding explored shape. It seems that this prefactor increases with the qualitative complexity of the shape. One can note that the circle has the smallest prefactor and the Eiffel Tower has the largest one. The Kullback-Leibler divergence D_{KL} can be used as a quantitative estimate of the complexity of a shape. This parameter measures a type of relative entropy between the probability distribution and a second one Q used as a reference. It is defined as $D_{\mathrm{KL}}(P\|Q) = \int_{-\infty}^{\infty} p(x) \log \frac{p(x)}{q(x)}\, dx$, where p and q are the corresponding probability densities. In our case, we compute the Kullback-Leibler for the chord length distribution of each figure compared to the one corresponding to the circle. In figure 1.19c we plot the prefactor error for the surface (up) and perimeter (down) as a function of the Kullback-Leibler divergence given for each figure compared to the chord length distribution of a circle. This plot gives a quantitative estimate of the correlation between the prefactor value and the complexity of the explored shape. From this figure, one can observe that the error prefactors σ_{0S} and σ_{0P} increase from the simplest shape, a circle, which has a rotational invariance, to the most complex shape, the Eiffel Tower.

1.5.5 Invariance under rigid transformations

Some evaluated shapes can be composed of disconnected objects and the equations eqs. 1.6 to 1.10 remain valid provided that the perimeter and area are replaced by the

sum of perimeters and areas, respectively. In figure 1.20 we compare the convergence in the estimation of the surface and perimeter of projected smileys composed of two circular eyes and a mouth. A robot was placed on the arena and bounces for several hours. Then, we analyze the illuminated regions corresponding to a rigid transformation of the initial smiley. The estimated area and perimeter converge similarly towards the same theoretical value with an error of less than 10% when the averages are made with 800 random intersecting lines. This agrees with the fact that the area and perimeter are geometrical invariants under rigid body transformations such as translations, rotations, mirrors, and combinations of them. Then, all the figures obtained by rearrangements in space will have the same point in the perimeter-surface plot. This is going to be a relevant property for analyzing more complex shapes.

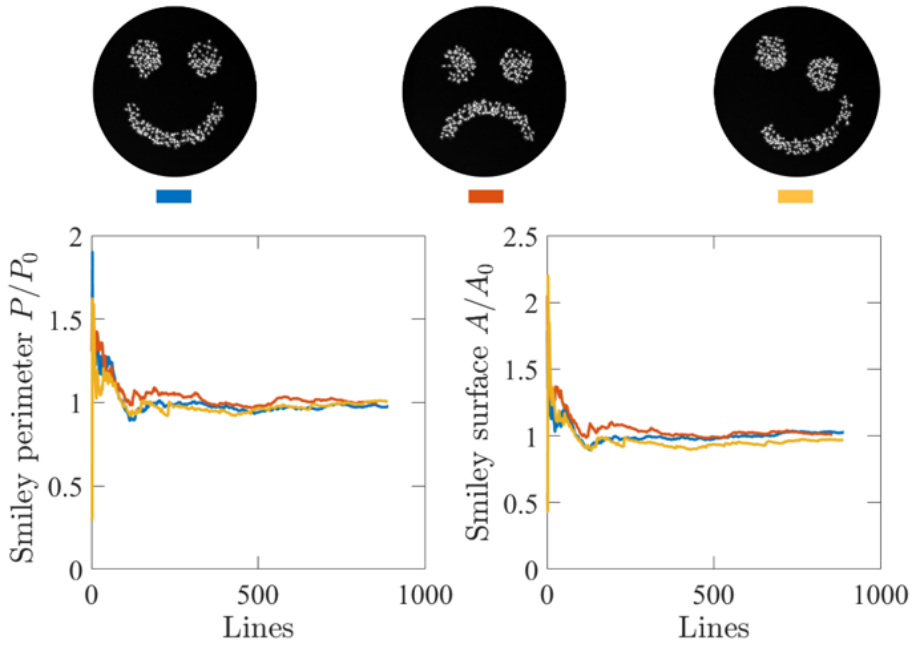

Figure 1.20: Invariant convergence under rigid transformation. Different states of a smiley present similar convergence for the estimation of the area and the perimeter of the region as a function of the intersecting lines.

1.5.6 Reading strategies

The recognition strategy based on the perimeter-surface space representation of an arbitrary 2D object is restricted to groups of figures which remain different after the application of any rigid transformation. If we consider the uppercase letters of the Latin alphabet and these forms are projected on the floor, we can perform the same robotic

exploration as before, to estimate their area and perimeter. For each letter, we obtain a different point in the perimeter-surface plot shown in fig. 1.21a. This allows us to distinguish the letters by means of a random ballistic exploration. It is important to note that this recognition is not possible if, instead of taking the uppercase letters, we use the lowercase letters. This is because, in this case, some letters would be a rigid transformation of another one (for example the letters d and b), retrieving exactly the same point in the perimeter-surface plot.

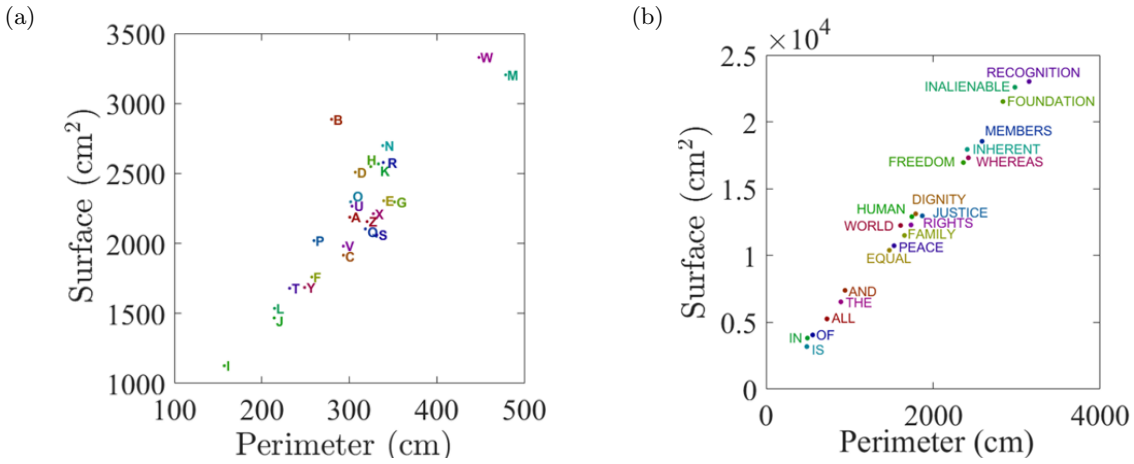

Figure 1.21: Recognition strategy for letters and words from a text. (a) The uppercase letters of the Latin alphabet and (b) the first words of the preamble of the Universal Declaration of Human Rights have a unique point in the perimeter-surface space representation.

We can extend this recognition strategy to distinguish words belonging to a text. In Fig. 1.21b we plot the perimeter and surface of the words contained in the preamble of the Universal Declaration of Human Rights [48], which plays the role of our word dictionary. We find that all the words can be separated in this diagram. To illustrate this, let us analyze the convergence for the area estimation of the word *FREEDOM* by means of a random ballistic exploration. We have two ways for estimating the area of this word. The first possibility would be to consider each word as a single object to be recognized. The second possibility is to consider the word as an object composed of several letters that can be individually recognized. To illustrate this, in figure 1.22a we plot an arbitrary line that crosses the letters O and D. In the individual exploration, after exiting the letter O, an estimation of its area and perimeter is performed, then the robot enters the letter D and when it exits this shape a new estimation of its area and perimeter is performed. In contrast, in figure 1.22b the exploration is performed throughout the full word which is considered as a single object.

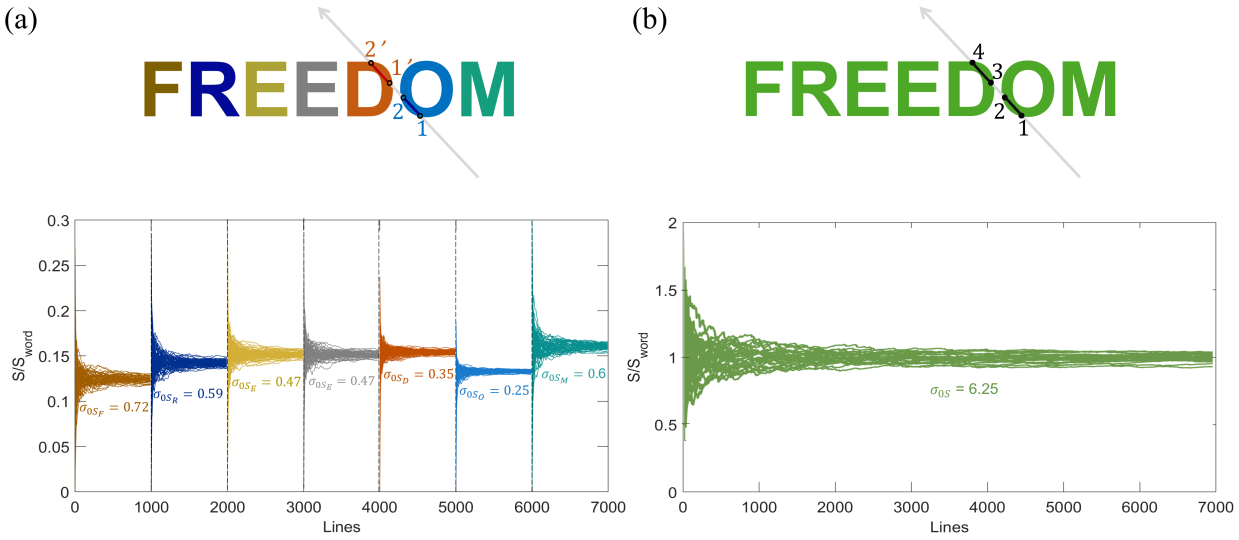

Figure 1.22: Convergence comparison for the surface estimation of the word FREEDOM as a function of the number of crossing lines. (a) Each letter is independently explored, and the corresponding area is estimated. From Monte Carlo simulations we obtain the error prefactor σ_{0S_i} for each letter. (b) The word is considered as a single shape to be randomly explored. Monte Carlo simulations give us the error prefactor σ_{0S}.

In order to compare the convergence of both strategies, in figs. 1.22, we plot the results of Monte Carlo simulations for the surface estimation as a function of the crossing lines. In figure 1.22a, we show the individual convergence plots for 1000 lines crossing each letter. Each plot corresponds to the estimated surface of each letter, normalized by the whole word surface S_{word}. Below each plot we show the obtained error prefactor σ_{0S_i}, where $i = F, R, ..., M$. Their corresponding relative error as a function of the crossing lines follows the law $\sigma_{S_i} = \sigma_{0S_i}/\sqrt{N}$. In figure 1.22b, we show the analogous convergence plot for 7000 lines crossing the whole word FREEDOM, and we also show the obtained error prefactor σ_{0S}. The relative error as a function of the crossing lines follows a similar law $\sigma_S = \sigma_{0S}/\sqrt{N}$. One can note that in the case of individual surface estimations, the error accumulates and the final relative error would be $\sigma_S = \sum \sigma_{0S_i}/\sqrt{1000} \approx 9\%$. On the other hand, in the case of a global exploration, the final relative error is $\sigma_S = \sigma_{0S}/\sqrt{7000} \approx 7\%$. This demonstrates that the surface estimation convergence is faster when we take the word as a single 2D object. This is due to the fact that if we choose a letter-by-letter strategy, the perimeter and surface area computation accumulates the uncertainties associated to the individual recognition of each letter.

1.6 Conclusions and perspectives

In this part of the thesis, we have shown that we can evaluate and recognize an arbitrary 2D object by means of a random ballistic motion. We employed some important results from geometric probability that were initially given for convex regions, but they have been recently extended for non-convex regions and Brownian motion. Additionally, we have extended Cauchy's formula for closed-loop trajectories. After achieving relevant mathematical developments, we found a new general invariant for a random ballistic exploration. This allowed us to return to the initial problem of evaluating and recognizing shapes in 2D. The combination of this new formula with Cauchy's theorem leads us to a direct estimation of the area and perimeter of any shape.

For each explored region, we associate a representation in the perimeter-surface plot. This is a very simple, but powerful way to distinguish a 2D object among a group of shapes. The proposed strategy is feasible because if we randomly take two arbitrary objects in 2D, the probability for them to superpose in this space representation is very small. This technique has been capable of recognizing complex figures, such as the silhouettes of some famous monuments and it was also extended to read letters and words from a text.

The proposed strategy does not require any knowledge of the absolute or relative position, nor of the direction of movement. The only requirement is to have a uniform random exploration of the region of interest. These ideas could find applications in micro-robotics where the memory capabilities are very limited and no global information can be provided. Thanks to the measurement of local quantities, a robot is able to recognize shapes and give relevant global geometric information about the region.

A possible extension of this work could be the combination of this strategy with machine learning. In particular, we can employ the algorithms used for clustering analysis to achieve an unsupervised recognition strategy. This would reduce the number of random crossing lines needed to distinguish a shape in the perimeter-surface space representation. The use of Gaussian Mixture Models could be a good alternative to achieve this goal.

2

Time reversal and wave engineering with damping pulses

2.1 Introduction

Damping is ubiquitous in nature and is present in most physical systems in which it is usually associated with a dissipation of energy [49]. This energy loss can be transferred to the environment in form of heat, or converted into another type of energy [50]. Damping is specially relevant for the understanding of vibrations and wave phenomena, where diverse dissipation mechanisms are encountered [51].

In this chapter, we are going to study some interesting applications of an active mechanical system in which elastic waves can propagate. This medium can perform a sudden and strong time-localized damping change for an initial propagating wave. We will demonstrate that in the limit of a high damping shock, it totally stops the wave, maintaining only the wavefield, while its time derivative is set to zero. This action generates two counter-propagating waves, one of them being, up to a factor of one half, the time-reversed version of the initial propagating wave. This represents a counter-intuitive effect because damping is usually associated with the irreversibility of a physical system , since it breaks the time-reversal symmetry of the governing equations of motion [52], [53], [54].

We will illustrate this new time-reversal mechanism with numerical simulations and an experimental proof of concept is provided with a system composed of repelling magnets that levitate on a tunable air cushion. This experimental system behaves like an elastic medium where longitudinal waves can propagate, and a damping pulse can be applied from the transverse direction to stop the wave. This action retains the wavefield and annihilates its time derivative, generating the two counter-propagating waves.

After introducing this new time-reversal mechanism, we will investigate what happens if we apply several damping pulses at specific times. We will show that the consecutive application of damping pulses can totally destroy a monochromatic wave, and in the case of broad band waves, the spectrum can be tailored thanks to a selective annihilation of specific wavelengths.

We will start by recalling a few important concepts regarding the time-reversibility of wave phenomena and the common techniques that are employed to perform time-reversal of waves.

2.2 The time-reversal invariance

At the microscopic level, the motion of particles is often well described by an interacting potential, which depends only on the relative position between them (due to electrostatic or magnetic forces). Then, their governing equations of motion, given from Newton's laws, are invariant under a time-reversal transformation. This means that if we could invert the velocity of each particle at a given time, we would expect to recreate exactly the same initial configuration of this system of particles. This idea was proposed by Loschmidt in 1850 [55], [56], to criticize the kinetic theory of gases as being incomplete to predict the irreversibility stated by the second law of thermodynamics [57]. The apparent paradox was solved in the XXth century [58], by considering the velocity of each particle as a random variable, which makes the system highly sensitive to the initial conditions. This implies the impossibility of reconstructing the original state due to the exponentially increasing position error as a function of time [59].

The second Newton's law of motion represents only an example among other equations in physics that are invariant upon time-reversal. Another example is given from the equation proposed in 1840 by D'Alembert [60], when he was studying the vibrations of an elastic string. Since then, it has been found that diverse physical phenomena can be well described by the so-called wave equation:

$$\Delta\phi - \frac{1}{c^2}\frac{\partial^2\phi}{\partial t^2} = 0 \tag{2.1}$$

where ϕ is a scalar or vector-valued function of the space and time coordinates, which is named the wavefield, and Δ is the Laplacian operator. We can observe that this equation is invariant under time-reversal transformation because if $\phi(\vec{r}, t)$ is a solution, then the

function $\phi_{Rt} = \phi(\vec{r}, -t)$ is also solution of the equation. In the case of an isotropic propagation which occurs when we have an homogeneous and stationary medium, the equation 2.1 has also a spatial reversibility because if $\phi(\vec{r}, t)$ is a solution of the above equation, then the function $\phi_{Rs} = \phi(-\vec{r}, t)$ is also solution of the equation. This is a fundamental characteristic of usual waves allowing them to follow a forward or backward propagation in space but also in time. Contrary to the case of particle systems, waves are less sensitive to slight perturbations [61], because they are governed by a linear system (when they are modeled by d'Alembert equation) and the errors do not grow exponentially with time as it is the case with particle systems. In this sense, if Loschdmidt had applied his idea to waves by inverting the time derivative of a wavefield described by D'Alembert equation, he would have noticed the refocusing of the initial propagating wave towards the source. Unfortunately, the first experimental realization of a time-reversal of waves was achieved more than one century later, when diverse mechanisms were engineered [62], [63], some of them employing sophisticated technology, while others only needing an instantaneous disruption of the wave propagation properties [5].

2.3 Time-reversal mechanisms for waves

The time-reversal of a wave does not take place spontaneously and various techniques have been developed to achieve this result for different wave systems, for instance, in the case of acoustic [64], electromagnetic [65] and surface waves [6]. These common techniques can be grouped into three categories: the phase conjugation, the time-reversal cavities and the instantaneous time-reversal mirrors. The first two mechanisms rely on the fact that any wavefield in a region of the space can be fully determined by knowing the field and its derivative on its enclosing surface [66]. The last mechanism has been recently demonstrated [5] and it requires only a sudden change of the medium properties.

2.3.1 Phase conjugation

The time-reversal mechanism obtained thanks to a phase conjugation of an initial wave front was proposed for the first time in 1948 by Denis Gabor [67], who introduced a new microscopy concept that he named "holography". This principle allows us to reconstruct an image from an interference pattern. An example of this reconstruction technique is illustrated in fig. 2.1, corresponding to the same image presented by Gabor during his Nobel prize lecture [68]. This principle is based on the fact that a monochromatic

source ϕ_m, can be mathematically expressed as the real part of the complex representation $\phi_m = \mathrm{Re}[A(\vec{r})e^{i\omega t}]$, where A is function called the phase [69]. Then, the wave associated with the conjugated phase is $\phi_c = \mathrm{Re}[A^*(\vec{r})e^{i\omega t}] = \mathrm{Re}[A(\vec{r})e^{-i\omega t}]$. We can notice that ϕ_c corresponds to the time-reversed version of the initial propagating wave ϕ_m.

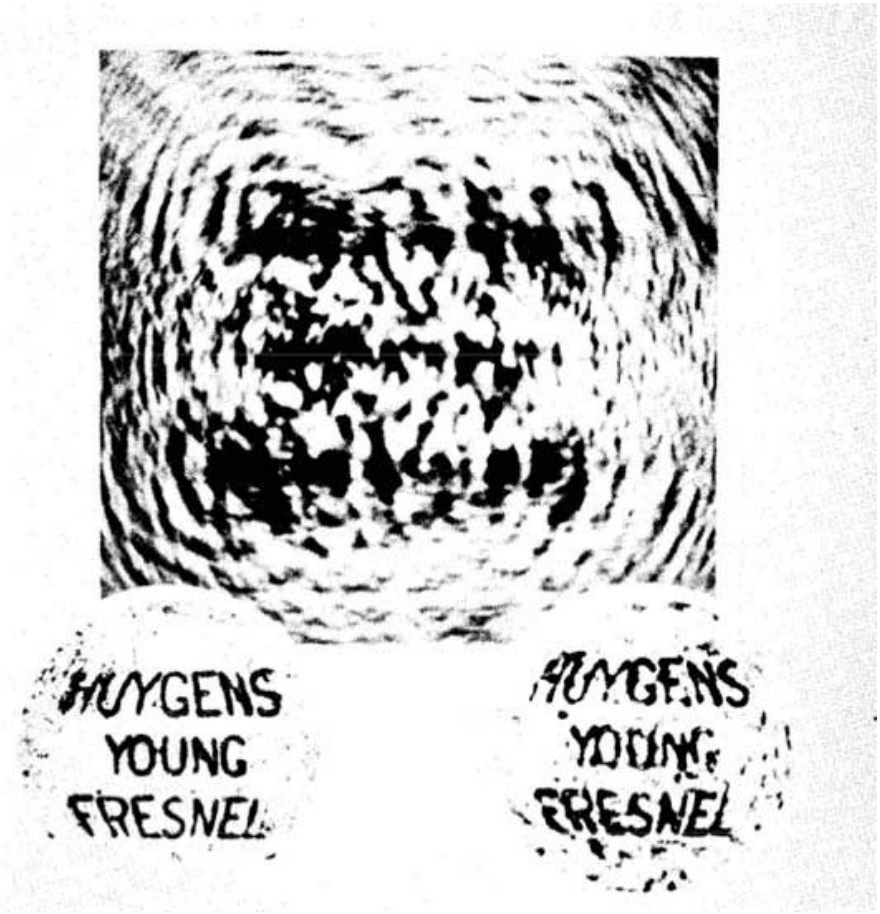

Figure 2.1: Example of image reconstruction by the principle of holography proposed by Gabor. On the left, we observe the original image and, on the right, we observe the reconstructed one. The complex image at the top corresponds to the diffraction pattern between a monochromatic source and the original image. This picture was shown during his Nobel prize lecture [68].

Gabor's idea to reconstruct an image by means of holography consisted in a two-step process, the first step was illuminating the object with a monochromatic source and recording the diffraction pattern on a photographic film (see fig. 2.2a). Then, the second step was reading the diffracting pattern [67], which was obtained by illuminating the photographic film with a plane wave similar to the first illumination to recover the superposition of the real image and a phase-conjugated version of this image at the focal plane of an objective (see fig. 2.2b). Because of this overlapping, the reconstructed

image appeared blurry, for this reason the science community lost interest in the phase conjugation technique for several years, until the invention of the laser in 1960 [70]. It allowed to exploit this idea of a reference recorded with the diffraction pattern off-axis, to create the first hologram of a three-dimensional object in 1962 [71], [72]. This highlighted the importance of the discovery made by Gabor, which led him to win the Nobel Prize in Physics in 1971 "for his invention and development of the holographic method" [73].

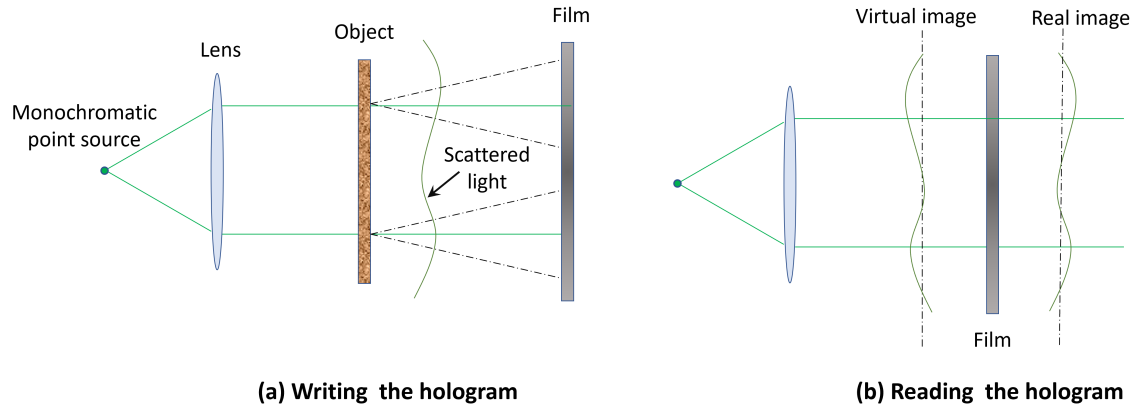

Figure 2.2: The holography mechanism designed by Gabor consisted of two steps: (a) Writing the hologram: an object is illuminated with a monochromatic source and the diffracted pattern is recorded on a photographic film. (b) Reading the hologram: the photographic film is illuminated with the same monochromatic source, and this generates a real and a virtual image of the object that overlap along the optical axis. The virtual image corresponds to the time-reversed version of the original image.

Later on, other phase conjugation mechanisms were proposed [74, 75], and they were implemented to electromagnetic and sound waves. A common configuration employs the properties of a non-linear medium to generate the time-reversed wave. This is the case of the four-wave mixing technique [76], in which an initial propagating signal wave is sent into a medium possessing a non-linearity of order 3 with two counter propagating "pump waves". The interacting waves generate a fourth wave which is proportional to the time-reversed version of the initial wave. Nowadays, there exist several alternative configurations in non-linear optics to achieve the phase conjugation [77].

2.3.2 Time-reversal cavities

The phase conjugation method was limited to the time-reversal of monochromatic waves; thus, a new mechanism was needed in order to apply it to broad band waves. This

was proposed by M. Fink and collaborators about 30 years ago [64], allowing them to refocus ultrasound waves. The idea was to record the wavefield by placing transducers on a surface surrounding the propagating region (see fig. 2.3). The propagating wave is recorded locally at the position of each transducer and their signal is sent to a computer to store them in a time sequence. Then, the time sequence is inverted and sent back to the transducers to reemit the time-reversed wavefield. From the time-reversal invariance of the wave equation, this process generates a counter-propagating wavefield in the medium that refocuses to the source. The principle of this "digital" time-reversal method is illustrated in the following figure, in the case of a heterogeneous propagating medium. This heterogeneity can be of practical relevance in reducing the number of transducers needed or to allow a sub-wavelength refocusing [61].

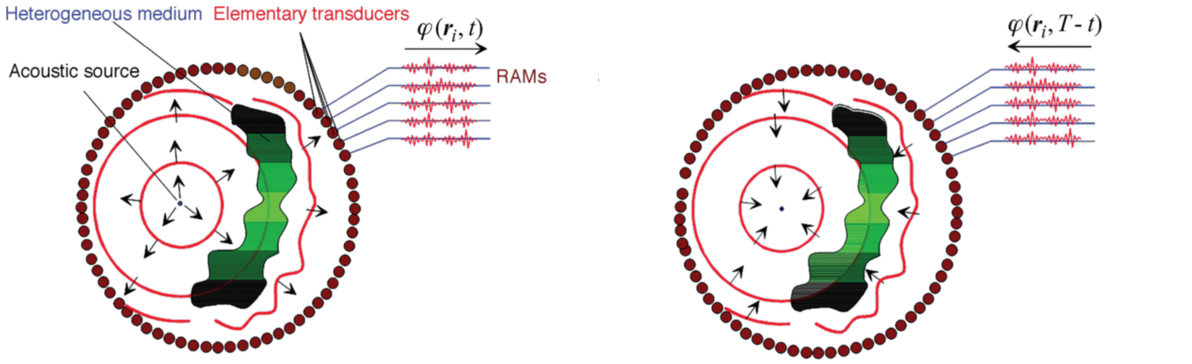

(a) At the time $t = T$, the transducers record $\varphi(r, t)$ **(b) At the time $t > T$ the transducers resend $\varphi(r, T - t)$**

Figure 2.3: Time-reversal cavity for acoustic waves. (a) First, the wave field is recorded by a network of transducers surrounding the medium. (b) Then, the signal is time-reversed on a computer and reemitted by the transducers, generating a wave that refocuses towards the source.

The previous experimental setup can be seen as a time-reversal cavity because the wave is surrounded by transducers which are able to record and then reemit the time-reversed wavefield. This idea has been exploited in nondestructive tests [78], [79], medical imaging [80], and treatments, such as the case of lithotripsy [81], thanks to the amplification of the refocusing wave returning towards the source [82]. The bandwidth of this time-reversal technique is only limited by the combination of the sensing speed of the detectors and the signal processing time [63]. This represents a relevant limitation in the case of electromagnetic waves and cannot be used in optics where the wavefield cannot be acquired.

2.3.3 Instantaneous time-reversal mirrors

The previous techniques have been extensively used to perform time-reversal of waves [83], [84], but they usually require a sophisticated technology to generate a time-reversed version of a propagating wave. A question that could come to our minds is whether there exists a simpler physical mechanism to generate a time-reversed wave from an initial propagating wave. This question has been recently answered by V. Bacot and collaborators in [5], where they demonstrated a new time-reversal technique by performing an instantaneous change of the propagating velocity. The proposed mechanism is illustrated in fig. 2.4, where a point source emits a wave packet at the time t_0 and propagates through a medium, which can be inhomogeneous. Then, a sudden spatially homogeneous disruption of the wave propagation properties occurs in the entire medium at the time $t_{ITM} = t_0 + \Delta t$. It results in the production of a counter-propagating time-reversed wave in addition to the initial forward-propagating wave. This counter-propagating wave refocuses at the source position at time $t_0 + 2\Delta t$.

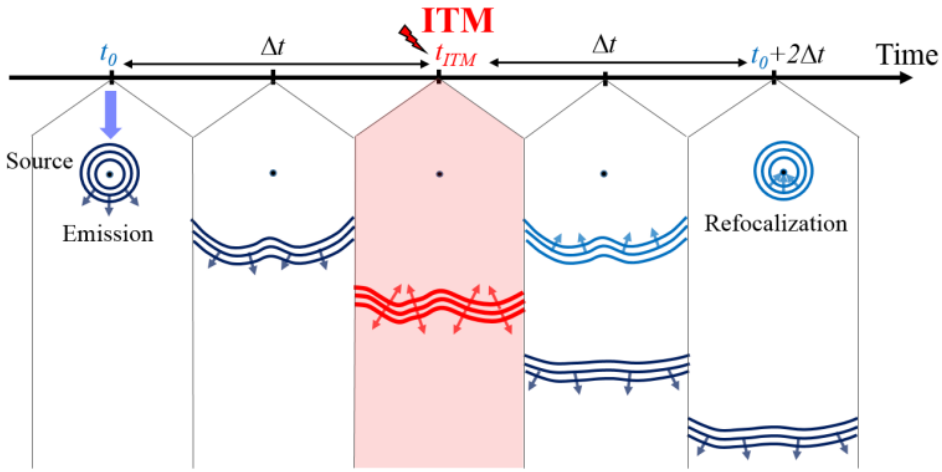

Figure 2.4: Principle of instantaneous time-reversal mirror. At the time t_0, a wave source emits a propagating wave packet in a given medium, then, a sudden spatially homogeneous disruption of the wave propagation properties occurs in the entire medium at time $t_{ITM} = t_0 + \Delta t$. It results in the production of a counter-propagating time-reversed wave, in addition to the initial forward-propagating wave. This counter-propagating wave refocuses at the source position at time $t_0 + 2\Delta t$

In [5], it has been shown that in the case of a disruption made by an instantaneous change of the propagating velocity, this generates a time-reversed wave whose amplitude is proportional to the time derivative of the initially propagating wave. Compared to the

time reversal cavities, the digital memory is replaced by an analog memory throughout the entire space. The experimental realization was done by employing gravito-capillary waves, and the instantaneous velocity change is performed with a shaker. This generates an abrupt acceleration change in the medium, creating an instantaneous disruption of the propagating velocity. An example of this time reversal mechanism is shown in fig. 2.5, in which a source having the shape of a smiley is time-reversed. This principle is general and can be applied to other types of waves. However, in the case of electromagnetic waves the propagating speed gives an experimental limitation for employing this technique as it would require an abrupt change of the refractive index for the entire medium [63].

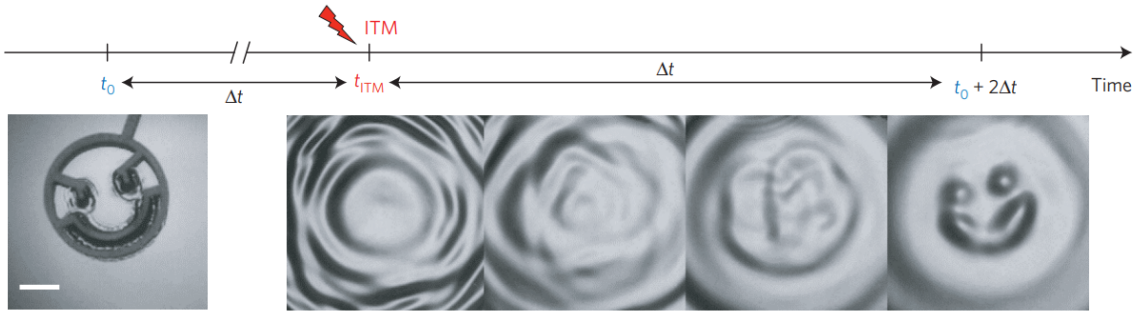

Figure 2.5: Image sequence of an instantaneous time reversal experiment with a complex source [5]. A source having the shape of a Smiley emits a divergent gravito-capillary wave. At the instant of the ITM, the wave field features a complex interference pattern in which the original shape is no longer apparent. As the time-reversed wave refocuses, the shape of the source becomes visible again. The time interval between two successive images is 26 ms.

2.4 A damping driven time-reversal mechanism (DTR)

In the previous sections, we described three relevant techniques that allow one to perform the time-reversal of an initial propagating wave. These mechanisms are based on the time-reversal invariance of the wave equation 2.1. Here, we are going to explore another simple but counter-intuitive method for time-reversing a wave, by adding a damping term to the wave equation. This is counter-intuitive because damping is usually associated with irreversibility in physical systems.

Let us imagine that we could stop a propagating wave, but totally retaining its wavefield. This would correspond to an instantaneous "freezing" of the whole wavefield at any time of its propagation. But what would happen if just after freezing this wave, we suddenly release it? This is the question that we want to address in this section.

Let us consider a wavefield $\phi(r,t)$ propagating, without damping, in a medium whose dispersion relation is $\omega_0(k)$. The wavefield can be described by the d'Alembert equation, which can be rewritten, after performing the spatial Fourier transformation [85], as:

$$\frac{\partial^2 \widetilde{\phi}}{\partial t^2}(k,t) + \omega_0^2(k)\,\widetilde{\phi}(k,t) = 0 \tag{2.2}$$

where $\widetilde{\phi}(k,t)$ is the Fourier space representation of $\phi(r,t)$. This equation is, as expected, also invariant under time-reversal transformation because if $\widetilde{\phi}(k,t)$ is a solution then, $\widetilde{\phi}(k,-t)$ is also a solution. In the case of a propagating wave where there exist multiple dissipation mechanisms, in the simplest approach they can be modeled by including a damping term which is proportional to the first order time derivative of the wavefield:

$$\frac{\partial^2 \widetilde{\phi}}{\partial t^2}(k,t) + \zeta(k,t)\frac{\partial \widetilde{\phi}}{\partial t}(k,t) + \omega_0^2(k)\,\widetilde{\phi}(k,t) = 0, \tag{2.3}$$

where $\zeta(k,t)$ is a time-dependent damping coefficient. We observe that, contrary to the previous equation, this additional term is not time-reversal invariant, thus, it can be seen as a source of irreversibility. In the following notations we will omit the dissipation k-dependence only for simplicity.

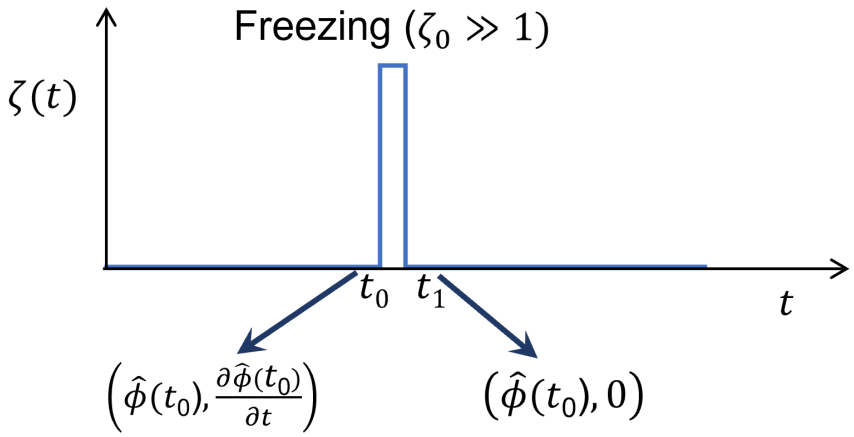

Figure 2.6: A high damping pulse applied from the time $t = t_0$ to $t = t_1$. A strong and instantaneous damping change is applied to an initial propagating wave. The state of the wavefield is changed from $\left(\widetilde{\phi}(t_0), \frac{\partial \widetilde{\phi}}{\partial t}(t_0)\right)$ by annihilation of its time derivative after the application of this damping pulse, then becoming $\left(\widetilde{\phi}(t_0), 0\right)$

First, we consider a medium where the damping coefficient is suddenly changed from

a very low value $\zeta \ll \omega_0$, at the time t_0 to a very large value $\zeta \gg \omega_0$, staying at this value until a time $t_1 = t_0 + \Delta t$, when is set back again to its original value $\zeta \ll \omega_0$. This damping term can be rewritten as $\zeta(t) = \zeta_0 \Pi(t)$, where $\Pi(t)$ is a unit rectangle function spanning from t_0 to t_1 and ζ_0 is the dissipation amplitude (see fig. 2.6).

Under this approximation, the DTR process can be interpreted as a change of the initial Cauchy conditions [86] for the time evolution of the wavefield $\left(\widetilde{\phi}(t), \frac{\partial \widetilde{\phi}}{\partial t}(t)\right)$ during the time of the application of the damping pulse. If we consider a total "freezing" of the wavefield and an annihilation of its time derivative, then at the time $t = t_1$, the new state becomes $\left(\widetilde{\phi}(t_1), \frac{\partial \widetilde{\phi}}{\partial t}(t_1)\right) = \left(\widetilde{\phi}(t_0), 0\right)$, which can be decomposed, according to the superposition principle [87], in two counter-propagating waves:

$$\left(\widetilde{\phi}(t_0), 0\right) = \frac{1}{2}\left(\widetilde{\phi}(t_0), \frac{\partial \widetilde{\phi}}{\partial t}(t_0)\right) + \frac{1}{2}\left(\widetilde{\phi}(t_0), -\frac{\partial \widetilde{\phi}}{\partial t}(t_0)\right) \tag{2.4}$$

The first term of the right member of this equation is associated (up to a factor one half) to the exact state of the incident wavefield before the DTR. It corresponds to the same wave shifted in time: $\widetilde{\phi}_{>}(t) = \frac{1}{2}\widetilde{\phi}_i(t - t_1 + t_0)$. The second term is associated with a wave whose derivative has a minus sign. It corresponds to the time-reversed wave: $\widetilde{\phi}_{<}(t) = \frac{1}{2}\widetilde{\phi}_i(t_1 - t + t_0)$. In the limit of $t_1 \to t_0$, the wavefield can be written, for a time $t > t_0$, as:

$$\widetilde{\phi}(t) = \frac{1}{2}\widetilde{\phi}_i(t) + \frac{1}{2}\widetilde{\phi}_i(2t_0 - t), \text{ for } t > t_0 \tag{2.5}$$

This damping driven time-reversal mechanism is illustrated in figure 2.7 where an initial propagating wave packet in a dispersive medium is created at the time $t = 0$ (see fig. 2.7a). Then, at the time $t = t_1$, a damping pulse is applied and the wavefield is frozen (see fig. 2.7b). The damping is then removed, resulting in the creation of two counter-propagating wavepackets with half of the amplitude of the initial one. The forward-propagating wavepacket is identical to the initial propagating one, as if no DTR was applied apart from the amplitude factor. The counter-propagating wavepacket is the time-reversed (TR) version of the initially propagating one. Thus, it narrows as it propagates, reversing the dispersion effect, until the time $t = 2t_1$ when it returns to one half of the initial profile.

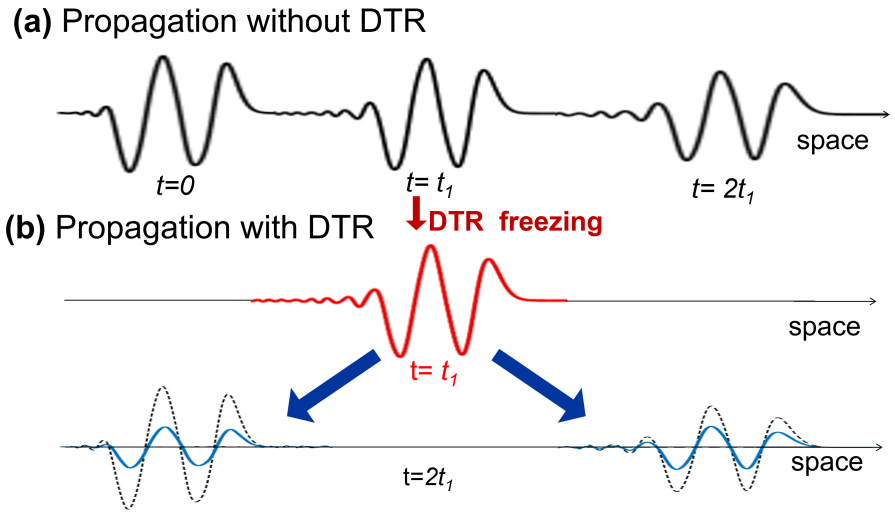

Figure 2.7: Principle of DTR. (a) Free propagation of a wave packet in a dispersive medium at times t_0, t_1 and $2t_1$. (b) The same initial propagating waves in (a) but at time $t = t_1$ a strong sudden damping pulse is applied, "freezing" the propagating wave (red curve). The pulse splits into two counter-propagating waves, each one having half of the initial wave amplitude and one of them being time-reversed. At time $t = 2t_1$, the counter-propagating wave (left) has the same initial profile (dotted line) but half of its amplitude. This also occurs with the propagating component (right), compared to the case of free propagation (dotted line).

Validity of this time-reversal mechanism

In the previous section, we analyzed the case of an infinite damping pulse applied during a very short time, now let us study the physical conditions needed to fulfill the previous approximation. A detailed analysis is provided in Appendix D and we only recover here the relevant results in order to analyze the limits of its validity for the case of a very large, but finite damping pulse.

Let us consider the application of a damping $\zeta_0 \gg \omega_0$ such that the third term of equation 2.3 can be neglected. Then, from a simple integration of this equation, between the time t_0 and $t > t_0$ we obtain the following expressions for the wavefield and its time derivative:

$$\widetilde{\phi}(t) = \widetilde{\phi}(t_0) + \frac{1}{\zeta_0}\frac{\partial\widetilde{\phi}}{\partial t}(t_0)\left(1 - e^{-\zeta_0(t-t_0)}\right) \tag{2.6}$$

$$\frac{\partial\widetilde{\phi}}{\partial t}(t) = \frac{\partial\widetilde{\phi}}{\partial t}(t_0)\, e^{-\zeta_0(t-t_0)}. \tag{2.7}$$

During this time interval, the system can be seen as an overdamped harmonic oscillator that returns quickly to a steady equilibrium state without oscillations. In this regime, the relaxation time increases with dissipation so that in the high dissipation limit, the wave amplitude does not have time to decrease. A detailed calculation shows that the amplitude decreases as $\exp\left(-\frac{\omega_0^2}{4\zeta}(t-t_0)\right)$ (see Appendix D). We find the following condition for the pulse duration $\Delta t = t_1 - t_0$, in order to retain the initial wave amplitude: $1/\zeta < \Delta\mathrm{t} < \zeta/\omega_0^2$ (See Appendix D for a detailed calculation). Then, if the damping is strong enough, the duration of the damping phase may be large compared to the period of the original wave. At time t_1, when the damping ends, the wavefield starts evolving again according to equation with the initial conditions:

$$\left(\widetilde{\phi}(t_1), \frac{\partial\widetilde{\phi}}{\partial t}(t_1)\right) = \left(\widetilde{\phi_i}(t_0), 0\right) \tag{2.8}$$

Under these conditions, we recover the same time evolution as it was predicted in the equation 2.5. In the limit of total retention of the wavefield, the damping pulse can have any duration, and when we go back to the initial damping conditions, we will always generate two counter-propagating waves. This is a remarkable result that can seem counter-intuitive but is only a consequence of the superposition principle.

2.5 An experimental proof of concept with levitating magnets

In order to experimentally illustrate the DTR mechanism, we designed a physical system able to perform a very fast time-controlled damping change for an initial wave that propagates through it. In other words, the system has to be able to suddenly "freeze" an initially propagating wave. This can be only achieved if the applied damping pulse is much faster than the propagating wave velocity. If we employ electromagnetic waves, we need a time-varying medium able to change its dielectric properties at a speed comparable to the speed of light which represents a very difficult task. If we want to use sound waves, we need a damping mechanism able to stop the molecules of the propagating medium. We could not find a straightforward implementation to fulfill a fast freezing and unfreezing of the medium compared to the wave oscillation period. Thus, we decided to create an artificial medium to perform DTR on phononic waves. We chose simple spring-like

interactions in a 2D system. However, we cannot use real springs because of their inherent damping, which prevents any time-reversal operation. The goal was to build an almost perfectly elastic medium able to perform a quick damping change, much faster than the propagating velocity of the mechanical waves that can propagate through it. If we were interested in a 1D implementation, we could have built a linear wave machine similar to the one designed by Shive in the 1960s [88]. We would only have had to design a system capable of stopping it completely at any time during its propagation. However, the 1D system cannot illustrate the wave refocusing that occurs after a time reversal operation, which generates a converging wave from an initially diverging wave. For this reason, we decided to design and create a 2D system, and the solution that came to our minds was to employ levitating magnets, which are repelling each other, creating an effective elastic medium, where oscillating and vibrating phenomena have been already observed [89]. If we place them on an air cushion, they will behave like an almost frictionless elastic medium. The only challenge is to stop all of them at once, and, for this purpose we use 4 high-speed pneumatic pistons that actuate a transparent PDMS plate to go down and stop them in less than 10 ms, achieving an almost perfect freezing of the wavefield. Several attempts were made with different configurations and porous media, but at the end, we achieved a nice experimental setup able to verify our proposed DTR mechanism. The details of the successful experimental implementation are described below.

2.5.1 Experimental setup

The experimental setup is shown in figure 2.8 and it consists of 200 magnetic disks made by gluing 5 mm diameter neodymium magnets (Supermagnete N35) on flat plastic disks whose diameter is 1.5 cm (fig. 2.8b) and their thickness is 1 mm. They are placed with the same magnetic orientation to have a repulsive interaction and they are confined within a 40 cm wide square. The boundaries of the square arena are also repulsive magnetic walls, which are filled with similar oriented magnets. This prevents the contact between the magnets and the boundaries to avoid energy dissipation. In order to have an almost frictionless system, the disks are sustained by a uniform air cushion that was obtained by injecting compressed air through a porous plate (Metapor BF100-AL). This reduces considerably the friction coefficient, allowing a small mechanical perturbation to propagate from one side of the system with a negligible energy loss. The disks were placed one by one, generating a self-organization resulting from the balance between repulsion and confinement. This is shown in figure 2.8c, where we can observe a slightly different concentration of magnets in the center. This is due to the small vertical deformation of

the porous medium as a result of the injected compressed air.

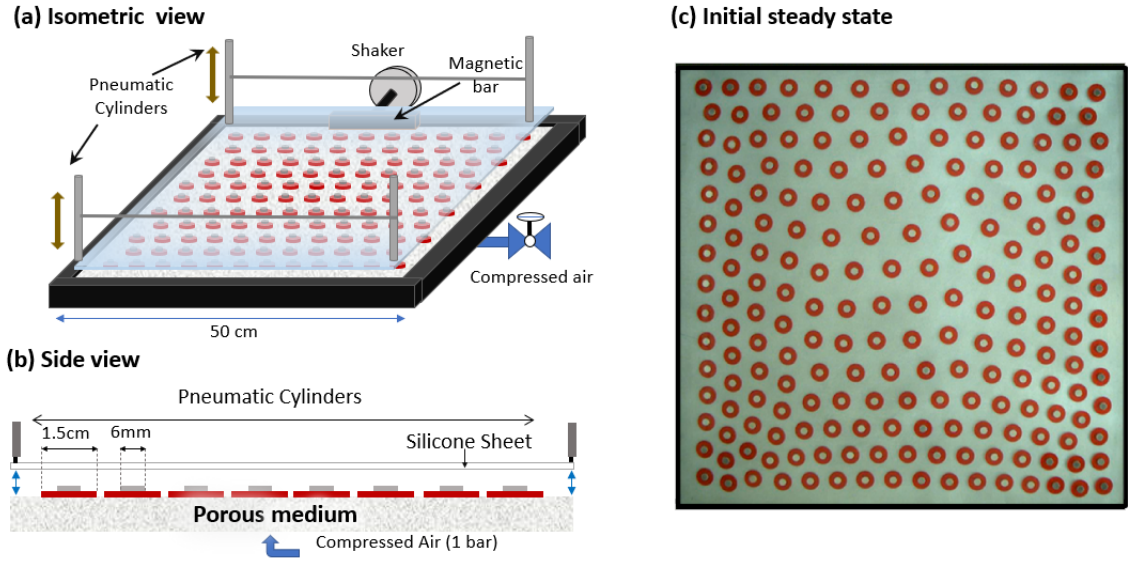

Figure 2.8: Experimental setup consisting of 200 red plastic disks with 5 mm diameter glued magnets. They have the same magnetic orientation. (a) The disks are confined in a square arena made of repulsive magnets. (b) An air cushion system is employed to drastically reduce the friction between the disks and the porous substrate. The abrupt change in damping is obtained with four pneumatic pistons that move down a PDMS sheet that totally stops the wavefield. (c) Top view of a steady self-assembled arrangement before the propagation of the mechanical excitation.

We control the amount of injected air to achieve an initial steady state, then we increase the amount of air to have a practically frictionless system. Once this equilibrium position is reached (see fig. 2.8c), mechanical excitations are sent through the magnetic array by moving a 12 cm wide magnetic bar that is placed on one edge and is also magnetically repulsive (see fig. 2.8a). The mechanical excitations are sinusoidal arches of amplitude equal to 1.9 $\pm$ 0.05 cm and a duration of 0.6 $\pm$ 0.01 s. This generates a traveling mechanical perturbation moving with a velocity of around 20 cm/s which is slow enough to be stopped by means of pneumatic actuators. The high damping pulse is generated with a vertical actuation of a transparent PDMS sheet that can go down to stop the system in less than 10 ms. It totally stops the wave field during 0.35 $\pm$ 0.05 s, then, it goes up again, releasing the magnets in less than 10 ms. The evolution of the system is recorded with a camera Basler acA1300-200uC at 50 fps, and the images are analyzed in Matlab, in order to track the disks positions over time.

2.5.2 Numerical simulations

We also performed numerical simulations of our experimental system. The levitating repulsive lattice of magnets was modeled as frictionless particles with spring-like interactions, and we implemented a Velocity-Verlet algorithm to solve the individual equations of motion. The details of this sympletic algorithm are given in [90]. The mechanical excitations were simulated by moving 12 cm of the upper boundary, with the same oscillating excitations as we did experimentally. The damping pulse in the simulations corresponds to a reset of the particle velocities, retaining only the positions from the time t_0 to t_1, corresponding to the duration of the experimental damping pulse. This corresponds to the high damping approximation where $\tau_0 \gg \omega_0$.

2.5.3 Experimental and numerical results

An experimental realization of a DTR of a single mechanical excitation is illustrated fig. 2.9a, where we plot in red the emission trajectories and, in green, the refocusing trajectories. We can observe that the individual time-reversed trajectory of each particle does not perfectly overlap the corresponding initial one. This is due to the small noise added by the damping pulse. Here, we are interested in measuring the average displacement of the particles around the source to quantify the quality of the time reversal operation. In fig 2.9b, we plot the average longitudinal displacement for the magnets surrounding the excitation source (disks with dark blue circles in 2.9a). The "freezing" is performed between the times $t_0 = 0.60$ s and $t_1 = 0.95$ s.

The application of a DTR produces a counter-propagating mechanical excitation with a time-reversed profile relative to the initial propagating one, with approximately one half of the initial amplitude. We also plot the results obtained from numerical simulations, considering harmonic interactions (dashed lines), showing a good agreement with the experimental observations. A comparison is made between the DTR case (green plot) and the case of a free propagation (red plot), where only a small vibration of the source is observed. A DTR of a double mechanical excitation was also experimentally achieved and the results are shown in fig. 2.9c, in which the damping pulse occurs between the time $t_0 = 1.35$ s and $t_1 = 1.75$ s. The DTR generates the time-reversed version of the initially propagating wave with approximately one half of the initial amplitude. As it was done for the case of a single pulse, the evolution is also compared with the free propagation (red plot). The dashed lines correspond to the results obtained from numerical simulations.

2.5.4 Validation and discussion

A way to measure the quality of the DTR is to calculate the experimental and numerical fidelities. This is performed by computing the normalized cross-correlation between the initial excitation profile from $t = 0$ to $t = t_0$ and the time-reversed profile after $t = t_1$. In figs. 2.9d-e we plot the normalized cross-correlations corresponding to the time reversal of a single, and a double mechanical excitation, respectively. In both figures, we observe a maximum in the cross-correlation when the back-propagation time equals the forward-propagation time. It reaches a value of 0.44 and 0.45, for the experiments with one and two excitations pulses respectively, in close agreement with the expected value of 0.5, in the case of an ideal elastic system. The minor discrepancy is presumably due to the remaining friction between the magnets and the porous substrate as well as the imperfection of the freezing process, adding a small noise in the magnets position during the DTR operation.

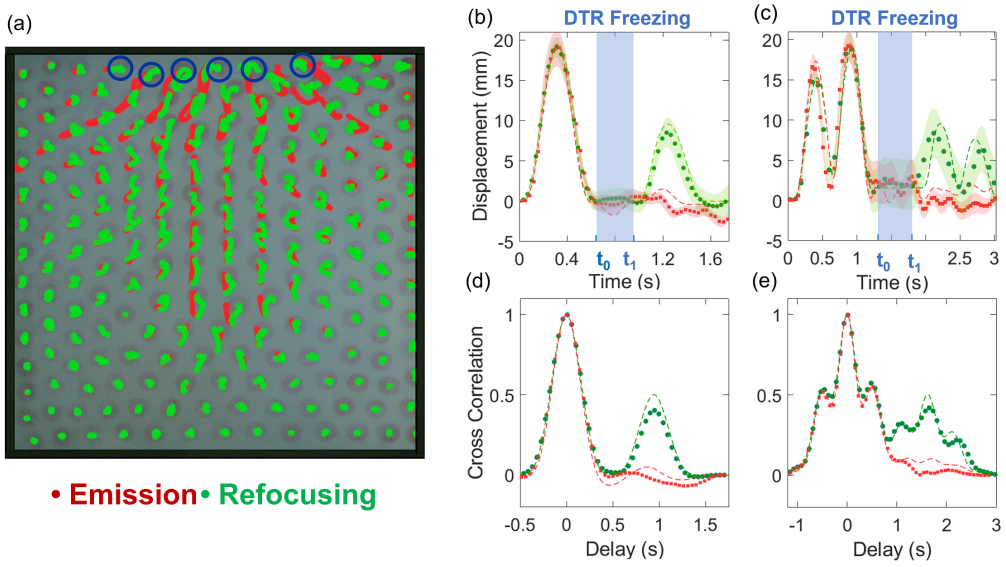

Figure 2.9: DTR of a mechanical wave with a single pulse profile (a) and a double pulse profile (b-c). Time evolution of the mean displacements in the longitudinal y direction of the six blue disks surrounding the excitation source. Experiments with a DTR performed between time t_0 and time t_1 (green circles) and control experiments without DTR (red square). The dashed lines correspond to the results obtained from numerical simulations. (d-e) Cross-correlation between the initial excitation profile from $t = 0$ to $t = t_0$ and the time-reversed profile after $t = t_1$. Each plot corresponds to the time reversal of a single, and a double mechanical excitation, respectively.

We have achieved an experimental demonstration of DTR of elastic waves that propagate through a lattice composed of levitating magnets. The propagating waves can

be written as a superposition of the normal vibration modes for this crystal. Then, they can be seen as traveling phonon waves. The kinetic energy associated with the time derivative of the field $\frac{\partial \widetilde{\phi}_i}{\partial t}$ vanishes when the high damping is activated, while the potential energy associated with the wavefield $\widetilde{\phi}_i$ remains unchanged. In the case of an initially propagating wave, the energy of the wave is equally partitioned between potential and kinetic energy. Thus, half of the initial energy is lost in the DTR process, resulting in a quarter of the initial energy being refocused to the source, while another quarter is diverging from it.

If instead of a traveling wave, we have a standing wave, the effect of the DTR would depend on its applied time, since the wave energy alternates between kinetic and potential. In the following sections we will discuss this idea to tailor the amplitude and spectrum of an initial wavefield by successive applications of DTRs.

2.6 Wave engineering via damping pulses

In the previous sections we have introduced a counter-intuitive method to perform damping-driven time-reversal of waves (DTR). We demonstrated that the application of an abrupt time-localized damping pulse to an initial propagating wave splits it in two counter-propagating waves with half of the amplitude before the DTR. As these waves move in opposite direction, they can interfere. In this section, we are going to analyze what happens if we perform multiple DTRs to the initial propagating wave. We will see that a time-controlled application of successive DTRs allows us to annihilate specific monochromatic components of a broadband spectrum. This can be useful to tailor any wave field by filtering only the frequencies we are interested in.

2.6.1 Standing waves created via DTR

A standing wave can be created thanks to a DTR operation. To illustrate this, let us consider a simple monochromatic traveling plane wave $\phi_i(x,\ t) = A\sin(kx - \omega t + \varphi)$, as shown in fig. 2.10, and we apply a DTR at the time $t_0 = 0$. Then this wave splits, according to eq 2.5, in the two following counter-propagating waves:

$$\phi(x,t) = \frac{A}{2}\left[\sin(kx - \omega t + \varphi) + \ \sin(kx + \omega t + \varphi)\right],\ \text{for}\, t > 0 \tag{2.9}$$

which can be rewritten as:

$$\phi\left(x,t\right)=A\sin\left(kx+\varphi\right)\cos\left(\omega t\right),\ \text{for}\, t>0 \tag{2.10}$$

This corresponds to a standing wave whose energy oscillates between potential and kinetic with an oscillating period $T = 2\pi/\omega$. Hence, the DTR operation applied to this monochromatic wave, generates a standing wave whose total energy is half of the initial energy, which can be verified by averaging the last equation over a period T. This standing wave generation based on a DTR is shown in the following figure.

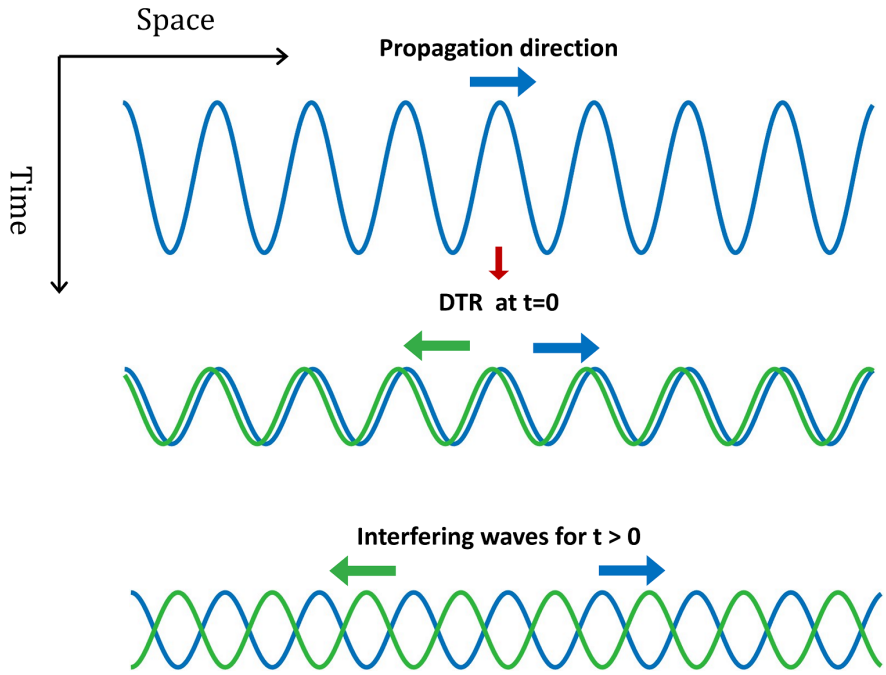

Figure 2.10: The application of a DTR to a monochromatic wave generates a standing wave that oscillates between kinetic and potential energies.

A DTR applied to a quasi-monochromatic wavepacket

A monochromatic source is ideal and due to duration limitations [91], a real source can only generate finite quasi monochromatic pulses, as the one depicted in figure 2.11. In this case, a DTR operation will create two counter-propagating monochromatic pulses that interfere only when there exists overlapping between them. This is illustrated in figure 2.11, where a source starts to send a monochromatic pulse at the time t_0, which propagates through space. At the time $t_0 = 1.5$ s, a DTR operation is performed creating two counter-propagating waves that interfere.

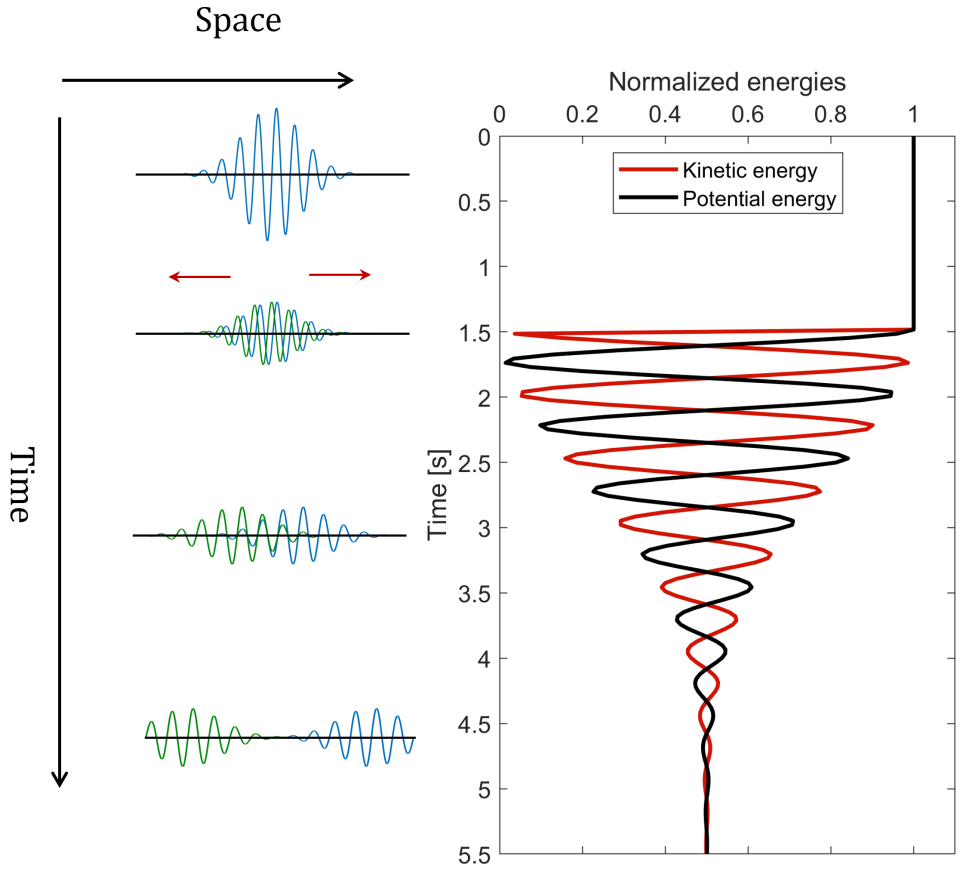

Figure 2.11: (left) A DTR opperation to a monochromatic pulse generates two counter-propagating wave pulses that interfere for a finite period. (right) During this interfering period, the total energy oscillates between kinetic and potential energy until the time when the wave pulses are separated enough to reach one half of the initial kinetic and potential energies.

On the left part of fig. 2.11, we plot the evolution of these wave pulses at different times. On the right, we plot the sum of their potential and kinetic energies, which oscillate when the counter-propagating pulses interfere. Before and after the interference period, both energies are constant because there is no overlapping between both waves. This is expected from the wave splitting given by the eq. 2.5, which predicts two counter-propagating waves, each one having one half of the initial amplitude.

2.6.2 Wave annihilation by applying two DTRs

In the previous section, we have shown that if we apply a DTR at the time $t = 0$ to an initial propagating monochromatic wave $\phi_i(x,\ t) = A\sin(kx - \omega t + \varphi)$, we generate the standing wave $\phi(x,t) = A\sin(kx+\varphi)\cos(\omega t)$ which has the same oscillating period $T = 2\pi/\omega$. Then, if a second DTR is applied at the time $t = t_0$, this standing wave splits, according to eq. 2.5, in two standing waves:

$$\phi(x,t) = \frac{A}{2}\sin(kx+\varphi)[\cos(\omega t) + \cos(\omega(2t_0 - t))] \text{ for } t > 0 \tag{2.11}$$

If the second DTR is applied at the time $t_0 = T/4 = \pi/(2\omega)$, we have:

$$\phi(x,t) = \frac{A}{2}\sin(kx+\varphi)\left[\cos(\omega t) + \cos(\pi - \omega t)\right] = 0,\ \text{for } t > \frac{T}{4} \tag{2.12}$$

Then, we achieve a total annihilation of the wavefield by applying the second DTR at the moment when the wave energy is purely kinetic.

If a the second DTR is applied at the time $t_0 = T/2 = \pi/\omega$, we have:

$$\phi(x,t) = \frac{A}{2}\sin(kx+\varphi)\left[\cos(\omega t) + \cos(2\pi - \omega t)\right],\ \text{for } t > \frac{T}{2} \tag{2.13}$$

In this case, we recover the initial standing wave: $A\sin(kx+\varphi)\cos(\omega t)$. Then, the application of a second DTR at this time does not have any effect on the wavefield that was present before its application.

This idea can also be implemented in the case of monochromatic wave packets, but in this case the wave annihilation would not be perfect. The reason is because the finite extension of the wave packets prevents the total destructive interference of the oppositely propagating wave fields (see fig. 2.12). However, if the amplitude of the remaining wavefield is much smaller compared to that of the initial traveling wave, we note that the initial wavefield is almost annihilated. In figure 2.12, we show the results of a numerical simulation where a monochromatic Gaussian pulse of period T is generated at the time $t = 0$. At the time $t = t_0$, a first DTR is applied, generating two counter-propagating pulses with half of the initial amplitude. They interfere and, during this interference period, a second DTR is applied at a precise time. If it is applied at the time $t = t_0 + T/4$, the wave field will be almost annihilated. However, if the second DTR is applied at the time $t = t_0 + T/2$, corresponding to the moment of constructive interference, the wave field does not suffer any change. This happens because no kinetic energy is present at

this moment, then, the application of a second DTR at this moment does not have any effect, and both waves continue their motion as if nothing had happened.

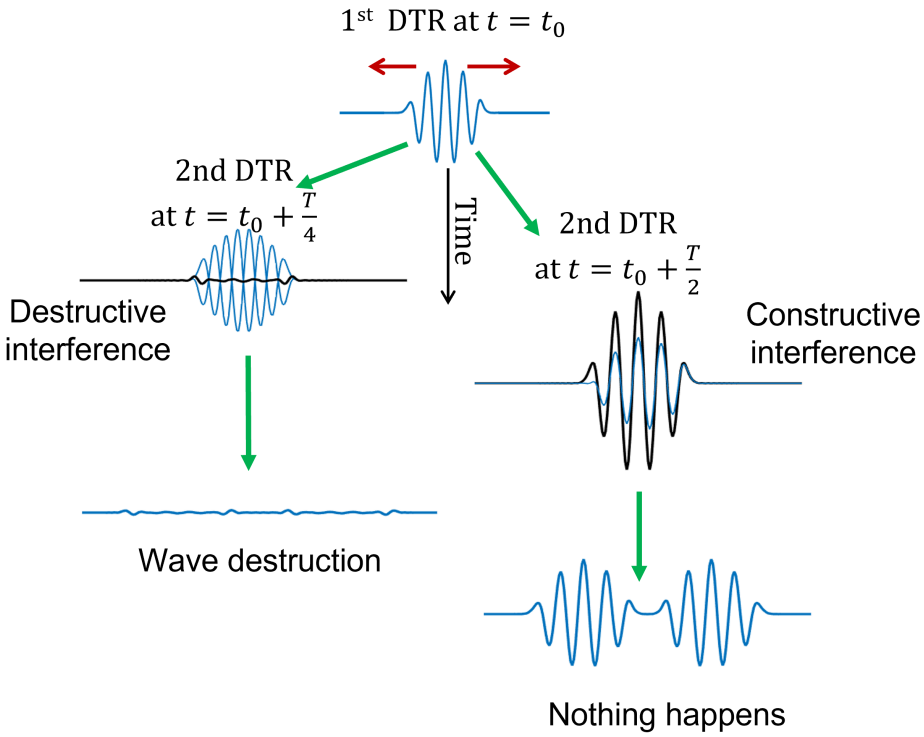

Figure 2.12: Two DTRs applied to a quasi-monochromatic wave packet. The first DTR applied at the time $t = t_0$ generates two counter-propagating waves that interfere when they are spatially overlapping. If a second DTR pulse is applied, the wave amplitude can be controlled depending on the time when this damping pulse takes place. For an application time corresponding to destructive interference (left), the second DTR annihilates the wavefield. For an application time corresponding to a constructive interference (right), the second DTR does nothing to the wavefield.

This can be easily understood from the fact that standing waves are alternating between kinetic and potential energy. We know that they reach their maximum amplitude when they have zero kinetic energy and they reach their maximum velocity when they have zero potential energy. We can do an analogy with a pendulum's motion, whose position has the same mathematical expression as a stationary wave, with oscillations between potential and kinetic energies. In this sense, the position of an oscillating pendulum of natural angular frequency $\omega = 2\pi/T$, can be seen as a monochromatic standing wave of period T. The first DTR applied at $t = t_0$ resets the oscillation, starting now from this point. Then, the pendulum's motion will be totally

stopped if a second DTR is applied at the time $t = t_0 + T/4$. This analogy is depicted in the following figure.

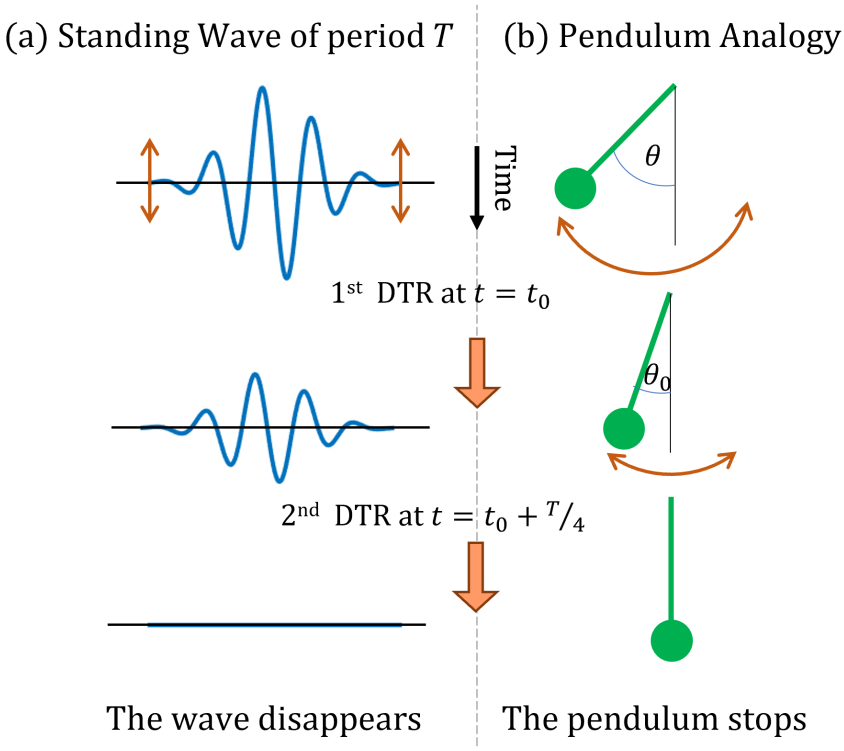

Figure 2.13: A monochromatic standing wave of period T can be seen as an oscillating pendulum whose natural frequency is $\omega = 2\pi/T$. After the application of a first DTR at $t = t_0$, the oscillation starts now from this point and will be totally stopped if a second DTR is applied at the time $t = t_0 + T/4$. This would correspond to a pendulum being in its maximum kinetic energy position, then, the second DTR will stop it forever.

2.6.3 Case of two monochromatic components

Let us consider now two sources emitting plane waves whose angular frequencies are ω_1 and ω_2, with $\omega_2 > \omega_1$. A traveling wavefield is: $\phi_i(x,\ t) = A\sin(k_1 x - \omega_1 t + \varphi_1) + B\sin(k_2 x - \omega_2 t + \varphi_2)$, where A and B are the amplitudes associated with each source. Then, after a first DTR applied at the time $t_0 = 0$ the wavefield becomes:

$$\phi(x,t) = A\sin(k_1 x + \varphi_1)\cos(\omega_1 t) + B\sin(k_2 x + \varphi_2)\cos(\omega_2 t),\ \text{for}\, t > 0 \qquad (2.14)$$

If we apply a second DTR at $T_1/4 = \pi/(2\omega_1)$, the first wave component is annihilated, and a part of the second wave component remains if and only if it does exist an integer $n \in \mathbb{N}$, such that $\omega_2 \neq \omega_1(1 + 2n)$.

On the other hand, if we apply a second DTR at the time $T_1/2 = \pi/\omega_1$, the first wave remains unaffected while the second wave component is annihilated if and only if $\omega_2 = \omega_1(1/2 + n)$, where $n \in \mathbb{N}$

Thus, a second application of DTR can be used to control the relative amplitude of any monochromatic wave if it is applied at the correct time. This technique can be useful for filtering the undesirable monochromatic components of a wavefield.

Chromatic filtering case of two quasi-monochromatic sources

The previous idea can be applied to the case of two monochromatic wave packets whose angular frequencies are ω_1 and $\omega_2 = \frac{3}{2}\omega_1$, respectively. To illustrate this, we perform a numerical simulation in 2D, with two sources emitting monochromatic wave packets whose angular frequencies are ω_1 and $\omega_2 = \frac{3}{2}\omega_1$, respectively. Each extended source can be considered as a superposition of point sources that are emitting a Gaussian radially propagating monochromatic pulses similar to the one shown in figure 2.11. We solve the wave equation at each time step by employing a centered finite difference scheme satisfying the Courant-Friedrich-Levy stability criterion, as detailed in [92].

In figure 2.14, we show the snapshots corresponding to the results of the simulation of two monochromatic wave packets that start to emit at the time $t = 0$. The moon-shaped source emits a wave packet at a frequency $w_1 = 10$ Hz and the sun-shaped source emits a wave packet at a frequency $w_2 = \frac{3}{2}\omega_1 = 15$ Hz. The wavefield is composed of the superposition of both sources and propagates through space. At the time $t = 1.5$ s, a first DTR is applied, splitting each monochromatic component in two counter-propagating waves. Then, a second DTR is applied at the time $t = 1.5 + T_1/2 \approx 1.53$ s, which annihilates one of the monochromatic components, corresponding in this case to the yellow wave, initially emitted by the sun-shaped source. The only remaining wavefield corresponds to the superposition of the monochromatic component initially emitted by the moon-shaped source and its time-reversed version that was generated at the time $t = 1.5$ s, both having one half of the initial propagating amplitude at the moment when the first DTR took place. Finally, at the time $t = 3$ s we observe a refocusing of the time-reversed wavepacket which will recover the shape of its corresponding source (the moon). We additionally observe the pattern corresponding to the initial traveling wave that only underwent an amplitude change after the application of the first DTR. The superposition of both waves causes a slight distortion during the refocusing process at $t \approx 3$ s.

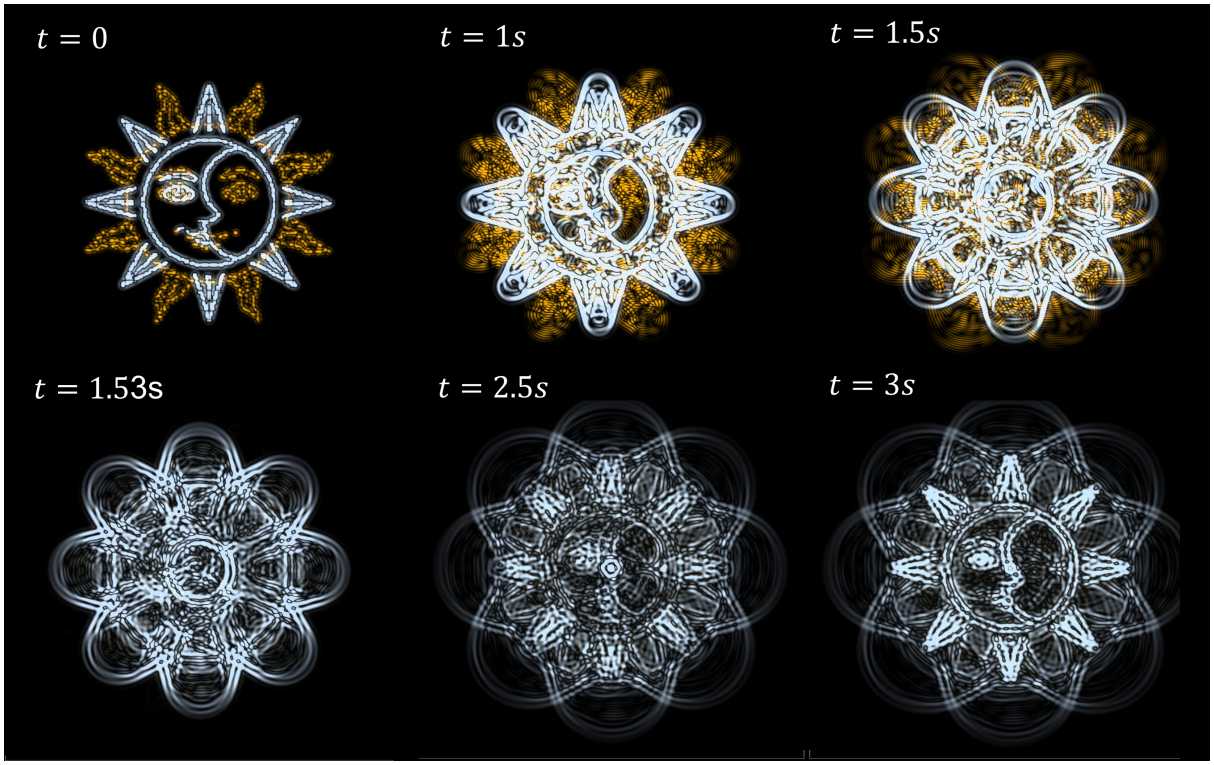

Figure 2.14: Chromatic filtering of a quasi-monochromatic wave packet. At the time $t = 0$ s, a moon-shaped source emits a wave packet at an angular frequency $w_1 = 10$ Hz and a sun-shaped source a wave packet at an angular frequency $w_2 = 3w_1/2$. A double DTR is applied with a time delay of $T_1/2 = \pi/w_1$. Both wave packets are damped by a factor 1/2 after the first DTR. The second DTR leaves the counter-propagating waves associated to w_1 unchanged, while annihilating the waves associated to w_2.

2.6.4 Spectral tailoring of a broadband wave

We can directly extend our "wave killer" strategy discussed in the previous sections to the case of a broadband wave. This is possible because a broadband wave can be seen as a linear combination of monochromatic wave sources having different frequencies ω_s. Then, the wavefield can be written as:

$$\phi\left(x,t\right) = \int_{w_1}^{w_2} A\sin\left(kx - \omega_s t + \varphi\right)\mathrm{d}w_s, \text{ for } t < 0 \tag{2.15}$$

After applying a first DTR at the time $t = 0$ the wavefield becomes:

$$\phi\left(x,t\right) = \int_{w_1}^{w_2} A\sin\left(kx + \varphi\right)\cos(\omega_s t)\mathrm{d}w_s, \text{ for } t > 0 \tag{2.16}$$

which corresponds to a superposition of standing waves. According to our previous

analysis, a monochromatic wave component having the angular frequency $\omega_l \in [\omega_1, \omega_2]$ is annihilated if a second DTR is applied at $t = T_l/2$. Consequently, this will also annihilate all the monochromatic components of angular frequency $\omega_s = \omega_l(1+2n)$, with $n \in N$ such that $\omega_s \in [\omega_1, \omega_2]$. This second DTR will also considerably decrease the amplitudes of the monochromatic components that are close to these values (see fig. 2.15). However, the second DTR does not have any effect on the monochromatic components whose angular frequency is $\omega_r = \omega_l(2n)$, with $n \in N$ such that $\omega_r \in [\omega_1, \omega_2]$ (see fig. 2.15).

In order to illustrate this spectral tailoring, we perform a numerical simulation with the normalized spectrum shown on the left part of the figure 2.15, where an arbitrary monochromatic component ω_l is chosen and we apply two consecutive damping pulses. The first DTR occurs at the time $t = 0$, re-scaling the spectrum energy by a factor of one half (dashed line of fig.2.15). The second DTR occurs at the time $t = \pi/(2\omega_l)$. The resulting spectrum after these two DTR operations is shown on the right part of the figure 2.15. One can note that the monochromatic components with corresponding angular frequencies $3\omega_l$ and $5\omega_l$ are also annihilated. However, the monochromatic components whose angular frequencies are $2\omega_l$ and $4\omega_l$ remain with the same amplitude as before the application of the second DTR.

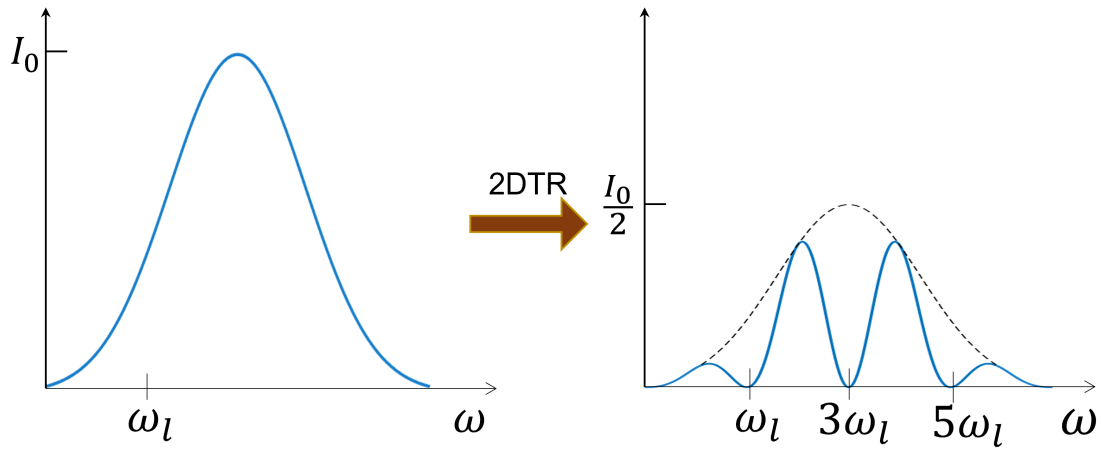

Figure 2.15: Spectrum tailoring by consecutive applications of two DTRs. The annihilation of a monochromatic wave component ω_l will automatically annihilate all the monochromatic components of angular frequency $\omega_s = (1, 3, 5, ...)\omega_l$. However, the monochromatic components of angular frequency $\omega_r = (2, 4, 6, ...)\omega_l$ remain with the amplitude obtained after the first DTR (black dashed line).

2.6.5 Discussion

The selective monochromatic annihilation for a polychromatic source can be easily understood by performing again a pendulum analogy. In this case, the first DTR generates a superposition of multiple standing waves described by the equation 2.16, which can be associated with multiple pendulums, each one having an oscillating period $T_s = 2\pi/\omega_s$, with $s \in \mathbb{N}$ (see fig. 2.16). If a second DTR is applied at the moment when a pendulum has a maximum kinetic energy, it will be stopped forever. This will be also the case for all the other pendulums that also reach their maximum kinetic energy at the time of the second DTR. However, the pendulums that are at the maximum amplitude at the time of the second DTR, will not suffer any effect and they continue their motion as if nothing had happened.

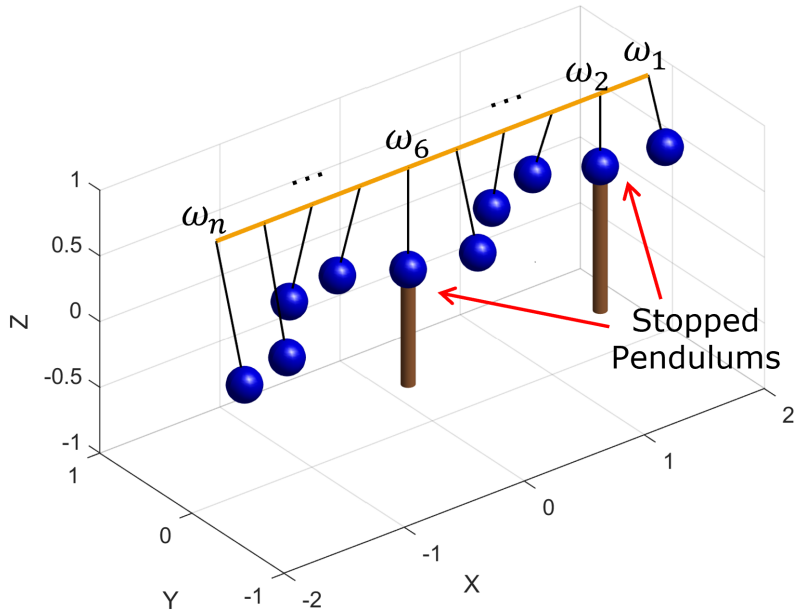

Figure 2.16: Analogy between a polychromatic source and multiple pendulums. After applying a first DTR to a polychromatic source, standing waves can be interpreted as multiple oscillating pendulums having the same frequencies. Then, if a second damping pulse is applied, the pendulums that synchronize at the moment when they have the maximum kinetic energy will be stopped.

2.7 Conclusions and perspectives

In this chapter, we introduced a counter-intuitive way to perform time-reversal of waves by means of time-controlled damping pulses. This complements the instantaneous mirror techniques [5], where a sudden disruption in the propagating medium generates two

counter-propagating waves. In our case, the Cauchy analysis in terms of initial conditions allowed us to predict the evolution after the application of a high damping pulse. In the limit of a high damping shock, we modify the initial conditions of a propagating field $\left(\phi_i, \frac{\partial \phi_i}{\partial t}\right)$ to $(\phi_i, 0)$, then, as a consequence of the superposition principle, the DTR produces two counter-propagating waves $\frac{1}{2}\left(\phi\left(t_0\right), \frac{\partial \phi}{\partial t}\left(t_0\right)\right) + \frac{1}{2}\left(\phi\left(t_0\right), -\frac{\partial \phi}{\partial t}\left(t_0\right)\right)$. One of these two waves is proportional to the time-reversed version of the initial propagating wave, and the other one is proportional to the initial propagating wavefield. The DTR is a general concept that could be applied to any type of waves by means of an abrupt damping change of the corresponding wave field. For instance, in optics, this could be done by abruptly changing the conductivity of the medium [93], in acoustics by using an electric-actuated change of the medium rheology [94].

In contrast with the instantaneous mirror approach based on wave velocity changes [5, 6] and standard digital time-reversal methods [95, 96], the backward-propagating wave is directly proportional to the TR of the original. From that perspective, the DTR has thus no spectral limitations and can be applied to broadband wave packets. This results in higher fidelity and enhanced broadband capabilities compared to other methods. The limitation in time-reversing wide spectral range comes from the ability to freeze the field sufficiently fast in comparison with the phase change in the wave packet. This restricts the maximum value for the angular frequency $\omega_0 \ll \zeta$ and also represents a challenge for time-reversing electromagnetic waves.

In the work presented here, we studied only the regime corresponding to a high damping pulse. It is evident that other regimes exist and do not allow a complete retention of the wavefield, then, they will only generate a partial reversal of the wavefield. These interesting regimes could be the subject of future research, where we could make an analogy with the propagation of waves in time varying media, a fast-growing field of research that has focused attention in recent years, with relevant applications in the case of electromagnetic waves [97].

Finally, we present an interesting application of the DTR when it is performed on waves that propagate in a homogeneous medium. We have shown that consecutive DTRs can annihilate specific monochromatic components and tailor a broadband wave. Thus, we have conceived a new absorbing mechanism that can be interpreted as a type of "spectral hole burning", which is widely used in spectroscopy [98].

3

Stabilization and propulsion of Leidenfrost puddles

3.1 Introduction

In this chapter, we study a new mechanism to stabilize a well-known active system: a liquid in the so-called Leidenfrost state [7]. This phenomenon can be observed when a liquid is deposited on a solid surface whose temperature is much higher than the boiling point for that liquid. There is an instantaneous formation of an insulating vapor layer at the interface between the substrate and the liquid, preventing the direct contact between these phases. Then, the evaporation process takes place very slowly, allowing a tiny droplet to last several minutes in the liquid state before being totally evaporated by the hot substrate. This phenomenon is counter-intuitive because the temperature of the substrate is much higher than that of the boiling point and the evaporation rate is suddenly decreased. A liquid in the Leidenfrost state can be considered active because it needs a constant flux of energy from the substrate in order to maintain itself in a state of levitation by means of a permanent generation of vapor under the liquid.

Liquids in the Leidenfrost state have a very rich dynamics which has been the subject of numerous fundamental and applied studies, as a result of the persistent interaction between the solid, liquid and vapor phases [99–108]. Moreover, due to the absence of contact between the liquid and the solid substrate, the liquid phase has a very high mobility and several propelling mechanisms have been engineered [8, 9, 109].

In the case of liquids that are deposited on flat substrates, only small droplets are stable during the evaporation process [110], whereas large volumes of liquid are unstable because of the overproduction of vapor under the liquid [111]. This vapor can constantly deform and move a large volume of liquid in all directions, generating an agitated state

with no preferential direction of motion. Moreover, after exceeding a characteristic size, we observe a random formation of bubbles which release the vapor pressure. These bubbles are created from the bottom part of the liquid and can eventually burst. When the puddle-shaped Leidenfrost liquids present these Rayleigh-Taylor type of instabilities, they enter in the so-called chimney regime [8, 110].

Here, we are interested in designing a mechanism to stabilize big amounts of liquid that are naturally unstable in the Leidenfrost state. It has been already shown that the chimney regime can be suppressed by increasing the concavity of the surfaces where the liquids are placed [103, 106, 112]. However, the liquids deposited on these concave surfaces can develop other instabilities, for instance, the breathing mode [113], and the star-shaped oscillating patterns [114]. This motivated us to propose a new method to stabilize large volumes of liquid in the Leidenfrost state, preventing also these oscillating instabilities. To achieve this, we got a rather simple idea: decreasing the pressure of the insulating vapor layer that is supporting the levitated liquid. In order to do that, we need a way to release a small fraction of the generated vapor below the liquid. This stabilizing mechanism is going to be addressed throughout this chapter. Finally, we will see that a slight modification can allow us to perform a directed propulsion of arbitrary big volumes of liquids.

This chapter is organized as follows. First, we will start with a brief introduction to this fascinating phenomenon, describing its most relevant dynamics. Then, we present the stabilizing mechanism for large liquid puddles deposited on flat surfaces with holes to release the vapor pressure. This is experimentally validated with water deposited on hot aluminum substrates that were perforated employing a homemade open source computerized, numerical controlled (CNC) drilling machine. Finally, by performing a slight modification of the stabilizing mechanism, we will show that directed motion can be achieved for the whole levitated liquid. This represents an alternative method to the ratchet symmetry-braking based [10], and other propelling mechanisms [115, 116], without any size restriction for the levitated liquid.

3.2 The Leidenfrost phenomenon

A very interesting and rather counter-intuitive phenomenon can be observed in the kitchen if we place a water droplet on a very hot pan, compared to the boiling point of water (see fig. 3.1). Instead of having a very quick evaporation, we will be surprised

to observe that the droplet remains as if it was not touching the plate. Indeed, the droplet levitates on a cushion of vapor that prevents the contact between the droplet and the hot surface, resulting in a very slow evaporation. The first observation of this phenomenon was reported by Herman Boerhaave in 1732 [117], however, it was named after Johann Gottlob Leidenfrost, a German doctor who did the first detailed description of this phenomenon in 1756 [7].

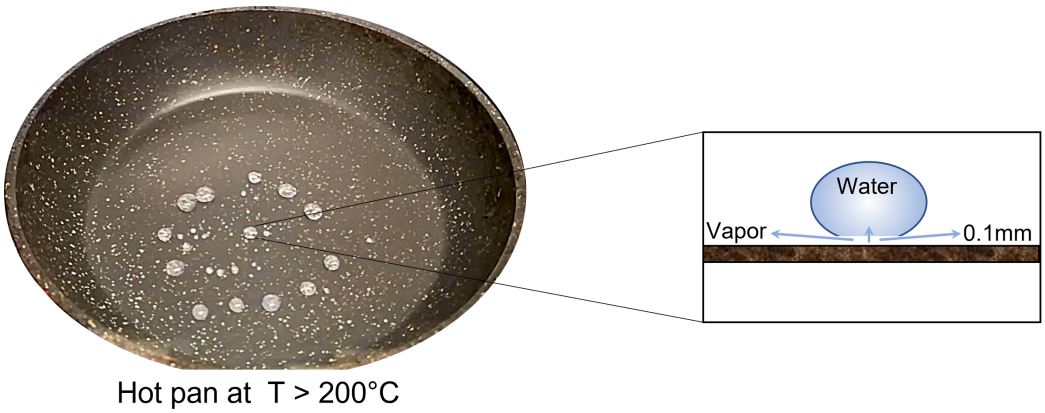

Figure 3.1: Leidenfrost phenomenon in the kitchen. When water droplets are deposited on a pan heated above 200°C they levitate on a cushion of vapor that supports the rest of the liquid.

Due to the very low thermal conductivity of the vapor, this layer insulates the rest of the liquid from a direct contact with the hot substrate. Thus, the drop evaporates much slower than if the temperature of the plate was close to the boiling point. The Leidenfrost phenomenon can be also observed when liquid nitrogen is spread on the floor. The room temperature is much higher than the boiling point for this liquid (-195 °C at 1 atm), then, the heat transferred from the ground instantaneously evaporates the lower part of the drop of liquid nitrogen, creating an insulating cushion of gaseous nitrogen that lifts the rest of the liquid.

During the last decades, the Leidenfrost phenomenon has been extensively studied under different conditions and experimental configurations [8], resulting in diverse dynamics for the levitated liquid. Examples of the different scenarios that appear are: oscillating star-shaped patterns [118], random production of bubbles in the so-called chimney regime [110], and self-propelling droplets [9]. Moreover, the Leidenfrost effect has been also observed on liquid substrates [119] and sublimating solids [120]. Much effort has been made to understand the underlying mechanisms of the Leidenfrost phenomenon because of its relevance for diverse engineering applications, in particular

those related to liquid based heat transfer [100, 121, 122], drag reduction [105, 123], transport of liquids [101, 124] and energy harvesting [125, 126].

The Leidenfrost temperature

The Leidenfrost temperature of a liquid is usually defined as the temperature corresponding to the abrupt change in the evaporation rate as the temperature of the substrate changes [8] (which can be solid or liquid). Several studies showed that the minimum temperature to achieve the Leidenfrost state depends directly on the physical properties of the heated liquid [127], the surface on which the liquid is deposited [128, 129], the ambient conditions associated with the boiling point of the liquid [130, 131] and gravity [132]. For the case of flat polished solid substrates, the Leidenfrost temperature for water ranges from 150 °C to 210 °C [128], whereas modified metallic surfaces can reach a Leidenfrost temperature above 1000°C [133]. Finally, when the heated substrate is a viscous liquid, it results to be very close to the boiling temperature of the levitated liquid [132].

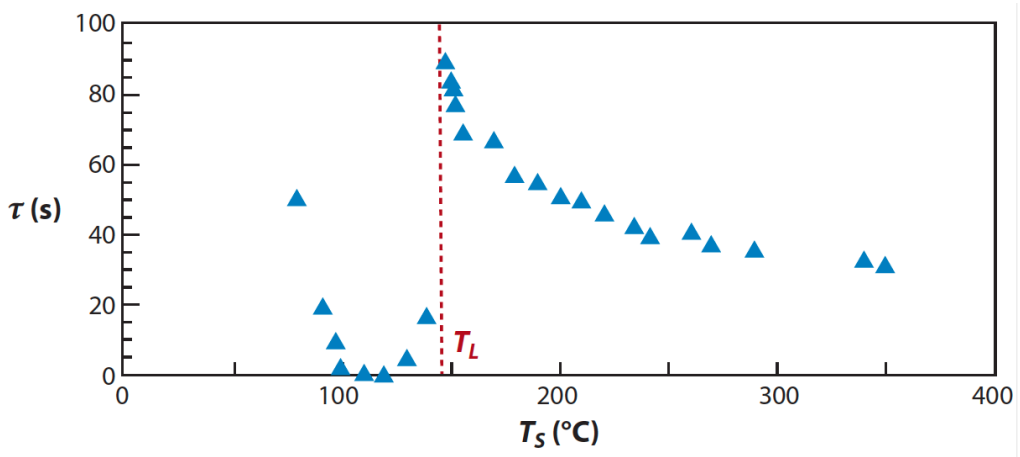

Figure 3.2: Lifetime measurement τ as a function of the substrate temperature for the case of a water droplet of radius $R = 1$ mm which is deposited over a polished aluminum plate (adapted from [8]). We observe a sharp increase at the temperature T_L for which a thick film of vapor sets between the plate and the liquid, preventing the whole evaporation of the liquid. This temperature is defined as the Leidenfrost Temperature.

3.3 Different dynamics

Liquids in the Leidenfrost state can develop different dynamics due to the interaction between the vapor and liquid phases, combined with the substrate and liquid properties. Here, we are going to recall the most important dynamics reported in the literature.

3.3.1 Stable regime

The stable regime corresponds to an absence of liquid agitation or rapid deformations due to the instability of the interface. Thus, the surface of the drop seen from above is a disk which slowly decreases during the evaporation process without changing its shape. Such a state can be seen as a sequence of perfectly quasi-steady non-wetting scenarios where a liquid is placed on a superhydrophobic surface [8]. Small volumes of liquid in the Leidenfrost state can develop a quasi-steady surface evolution when they are placed on smooth surfaces. Droplets in such a state acquire a spheroid or puddle-like shape, according to their characteristic length compared to the capillary length of the levitated liquid, denoted λ_c. This physical parameter corresponds to the ratio between surface tension and gravitational forces, and it is defined as $\lambda_c = \sqrt{\frac{\gamma}{\rho g}}$, where γ is the surface tension of the fluid interface, ρ is the density of the liquid, and g is gravitational acceleration.

Spherical droplets

When a droplet is smaller than the capillary length, surface tension forces dominate over gravity and the liquid takes the shape that minimizes the area for a given volume. Therefore, the droplet shape is almost spherical, as depicted in figure 3.3a, for a millimetric droplet placed on a smooth metallic substrate heated at 300 °C [8]. Only a very small portion of the bottom part of the liquid is flattened by gravity. However, even if these tiny droplets can have a quasi-steady evaporation (that can last several minutes in the case of water), it has been shown that they can also perform a spontaneous jump at the end of their evaporation process [134].

Puddle-like shapes

A volume of liquid whose characteristic size is larger than the capillary length takes the appearance of a puddle, as it is flattened by gravity, with a typical thickness of twice the capillary length λ_c, as a result of the equilibrium between the hydrostatic and surface

tension pressures [8]. An example of this puddle like shape is shown in figure 3.3b. In the case of liquids deposited on flat surfaces, only small volumes can have a stable puddle shape, because large puddle-shaped liquids become unstable due to the Rayleigh–Taylor instability [135]. The vapor layer pushes the liquid, and a pocket of vapor can grow from the insulating layer to rise in a form of bubble with a sudden burst at the top of the liquid surface [110].

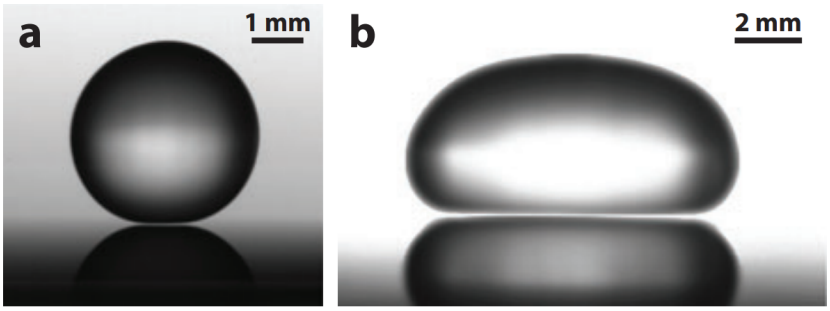

Figure 3.3: Stable shapes of Leidenfrost droplets placed on a smooth metallic surface heated at 300°C [8]. (a) Small droplets acquire a spherical shape, whereas big amounts of liquid acquire a puddle shape because they are flattened by gravity.

3.3.2 Unstable regimes

The Leidenfrost state of a liquid possesses a very high mobility due to the absence of direct contact between the liquid phase and the solid substrate. Consequently, several complex dynamics can take place if one increases the amount of deposited liquid [110,136], applies an external forcing [132, 137] or modifies the surface properties of the substrate [138], the heating mechanism [107, 139] or the ambient conditions [140]. Here, we are going to recall the three most relevant dynamics that have been intensively studied in the literature.

Chimneys

The vapor layer can become unstable for sufficiently large droplets. It creates bubbles ascending from the bottom part of the droplet with a liquid dome which eventually burst [110]. In the case of concave substrates, the vapor pocket transported by this chimney can eventually travel towards the edges, before bursting and generating strong oscillations for the levitated liquid [141]. These chimneys are created as a result of the Rayleigh-Taylor instability that occurs when a fluid of high density is at the top of another one of lower density [142]. The gravitational force competes with the surface tension force of the

droplet when this has a radius larger than the capillary length. On flat surfaces, it has been demonstrated that the chimney regime appears for a flattened droplet whose radius is approximately four times the capillary length [110] [136]. Examples of puddles of liquid presenting this regime are shown in figure 3.4, where vapor bubbles distort the surface of the liquid. The outline of each bubble appears as a clear ring thanks to an external lighting. We observe that the number of generated chimneys increases with the amount of deposited liquid.

The dynamics of this chimney regime is still not fully understood, but it has been shown that variations in the shape of the substrate, and also its phase, can affect the instability [103, 106, 119]. In particular, an external forcing can be used to suppress this instability, but generating other meta-stable states [143].

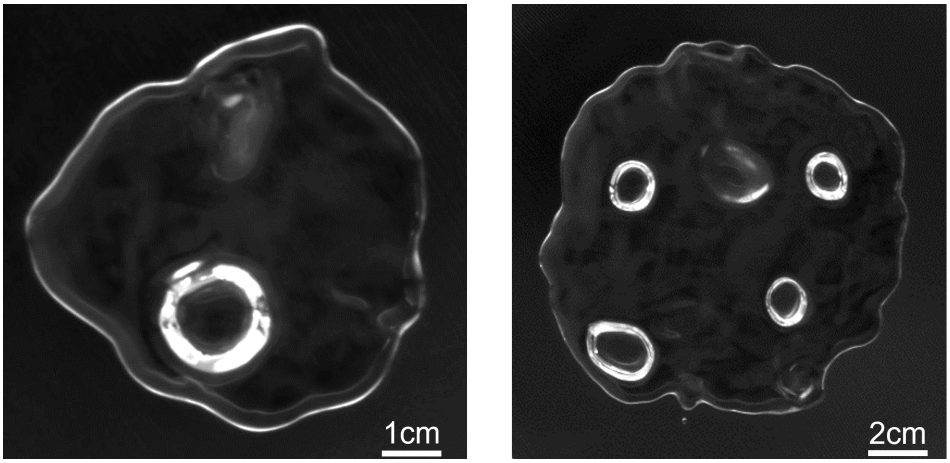

Figure 3.4: Chimney regime on flat surfaces. Large puddles of water on a slightly concave aluminum plates heated at 300 °C present the formation of bubbles that suddenly burst. The number of chimneys increases with the amount of liquid that is deposited on the hot substrate.

Oscillating stars

The formation of oscillating star-shaped patterns of a levitated liquid has been reported in the literature for different levitating mechanisms, for instance in vertically vibrated liquids placed on hydrophobic surfaces [144, 145], acoustically or magnetically levitated drops [146, 147], and drops excited with an alternating gas flow [148]. As this regime has been encountered in such diverse scenarios with different levitating mechanisms, it has been suggested that the origin of this oscillating star-shaped patterns is purely hydrodynamic, due to an oscillating thickness that gradually transmit the vibrating modes to the edges of the droplet [111]. In the case of Leidenfrost liquids this metastable state has also being encountered in concave surfaces [106], [114].

The appearance of these oscillating star-shaped patterns can be associated to a temporal modulation of the eigenfrequency modes of the drop, due to the self-forcing, thus inducing a parametric instability [149]. In the case of highly viscous liquids, the vibration transmitted from the vapor layer is considerably damped and only a few modes can appear [150]. Examples of these star-shaped patterns are depicted in figure 3.5, corresponding to the case of Leidenfrost drops placed on concave aluminum surfaces heated at T = 350 °C. The oscillation modes with n = 2 to n = 13 are shown when the lobes are at their maximum displacement [118].

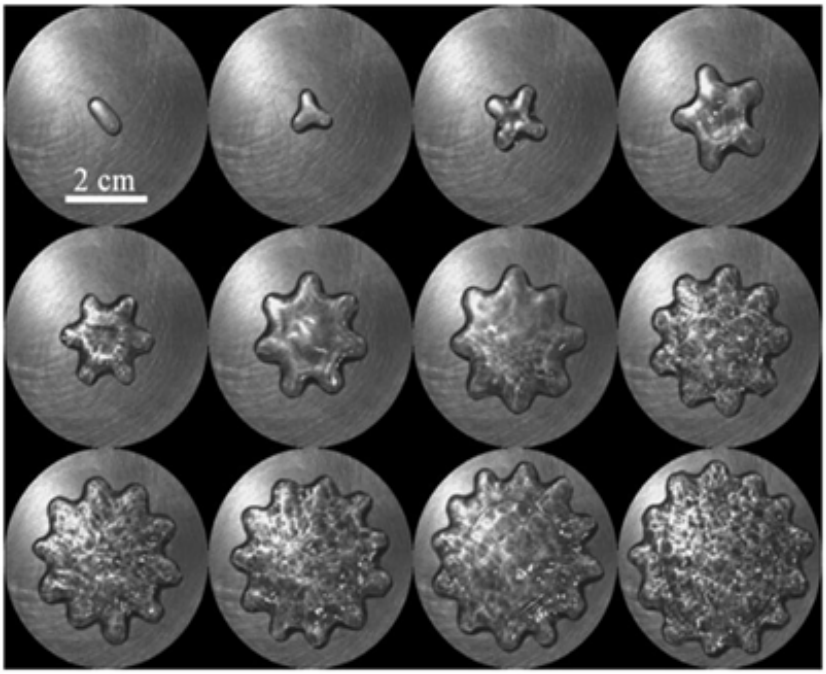

Figure 3.5: Star-shaped oscillation patterns of Leidenfrost drops placed on concave aluminum surfaces heated at T = 350 °C. Oscillation modes with n = 2 to n = 13 are shown when the lobes are at their maximum displacement. The scale bar corresponds to 2 cm [118].

Self propulsion

The Leidenfrost droplets are a very good example of an almost frictionless system. They can be set in motion by means of a simple symmetry breaking of the vapor flow coming out from the insulating layer that prevents the contact between the liquid and the substrate. A well-known symmetry breaking vapor flow mechanism was obtained by employing ratchet shaped surfaces [9]. These devices induce self-propulsion for small droplets in the opposite direction to the teeth orientation as it is shown in figure 3.6a. Diverse configurations based on the same propelling principle have been studied [102, 120, 151, 151, 152]. Additionally, other symmetry breaking configurations have been achieved

by engraving herringbone patterns on solid substrates [153] (fig. 3.6b) , turbine inspired shapes [154] (fig. 3.6c) and micro-surface tailoring (fig. 3.6d) [138,155,156]. Furthermore, in recent studies, instead of applying a modification of the substrate topography, a directed vapor flow has been obtained by means of a selective heating [139] or a temperature gradient [107]. Examples of some of these propelling mechanisms are shown in figure 3.6.

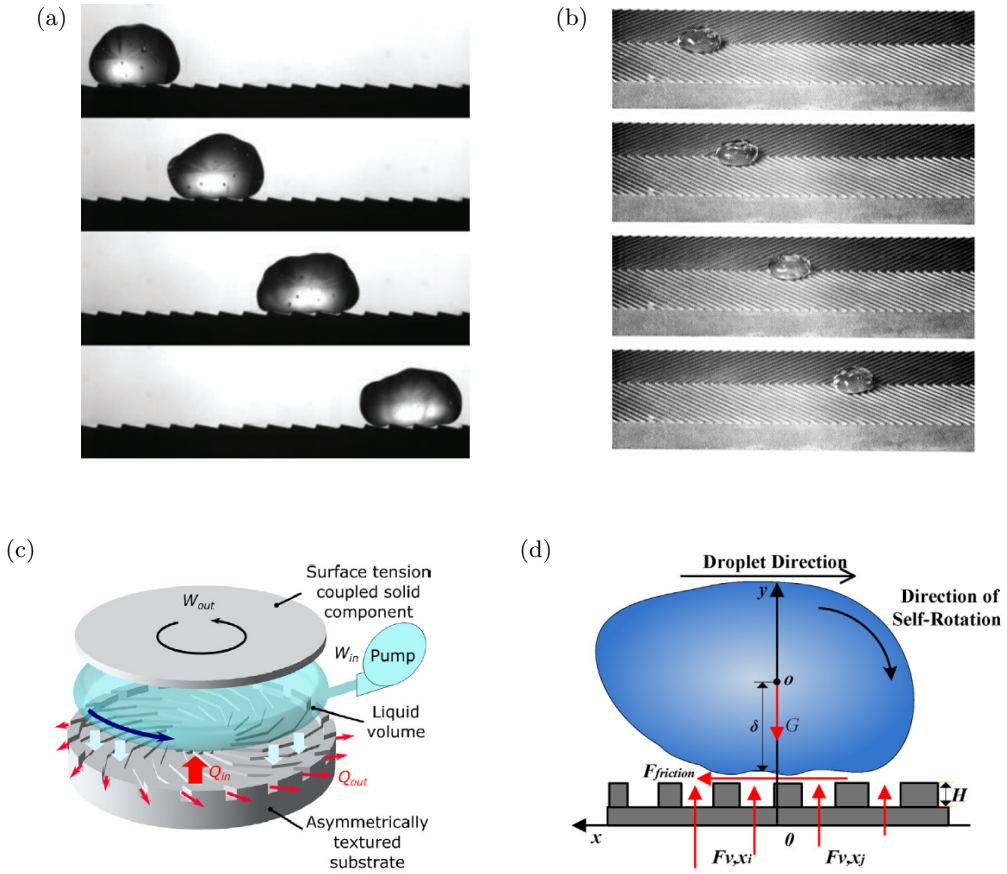

Figure 3.6: Several propelling mechanisms have been engineered for propelling small volumes of liquid. (a) Linke's device appearing in [8]. A liquid drop placed on a hot ratchet with teeth of depth a = 0.2 mm and length L = 1.5 mm, moves in the direction shown in the snapshots. The time interval between the successive pictures corresponds to 40 ms. (b). Self-propulsion on a herringbone [153]. A drop of acetone self-propels when it is placed on the axis of a hot herringbone engraved in brass heated at T=400 °C. Each herringbone channel has a depth H = 0.2 mm and a width W = 1 mm. The wall thickness between channels is 0.2 mm. The time interval between the images is 0.2 s. (c) A continuously operating Leidenfrost rotor [154]. The liquid is supplied through a pump to have a constant amount of liquid in Leidenfrost state. The substrate engraved with a turbine-inspired pattern rectifies the vapor to produce work, which is observed on the rotation of the solid component placed at the top of the liquid. (d) Self-propulsion mechanism for a Leidenfrost droplet placed on a hot surface with wettability gradient [155]. Schematics for the mechanism of directional droplet motion on a micropillared surface with an increasing spacing.

3.4 Stabilization with a perforated substrate

On flat surfaces, it has been demonstrated that a Leidenfrost droplet becomes unstable for a critical radius of around four times the capillary length [110] [136]. Above this size, a volume of vapor will grow and eventually burst, as a result of the Rayleigh-Taylor instability [110] in the so-called chimney regime. In the literature, it has been shown that big amounts of liquids can be stabilized by placing them on concave surfaces [103, 106] which suppress the Rayleigh-Taylor instability [114]. Examples of this stabilizing mechanism are shown in figure 3.7, where big amounts of liquid are placed on a conical surface (a) and a concave ring (b). Both concave surfaces are able to suppress the chimney regime, but other meta-stable states can take place [106]. In the case of a levitated torus, polygonal instabilities can take place, as a result of the competition between surface tension and inertial forces [157].

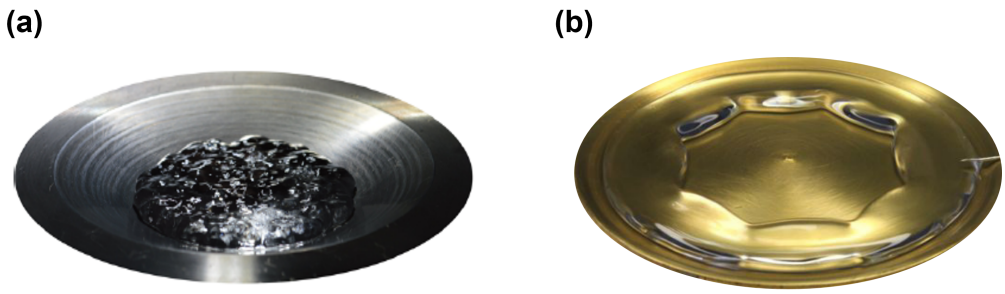

Figure 3.7: Large amounts of liquid suppress the chimney regime when they are placed on concave surfaces. (a) Levitating water placed on a conical shape [106]. The liquid presents high mobility on the conical shape without generating any bubble. (b) Levitating tori of water showing a polygonal pattern that is formed at the inner side of the tori, without the appearance of chimneys [103].

Here, we are interested in the possibility of creating another mechanism for stabilizing large amounts of liquids instead of using concave surfaces. The key idea is decreasing the overpressure induced by the vapor that would otherwise destabilize the bottom part of the liquid by enabling it to be released through another path. In the case of a liquid placed on a hot concave surface, the lateral escaping of vapor can prevent the chimney formation but the concavity has to be increased as we increase the volume of levitated liquid [106]. Furthermore, other metastable states may appear, for instance, star and polygonal shapes [103, 106]. If instead of a lateral vapor flow, the vertical downward direction could be used to release the vapor, this would prevent the formation of chimneys and avoid destabilization due to the lateral drag. This mechanism would also stabilize the

levitated liquid as a result of a local pressure drop. This can be achieved by doing small perforations connected to external ambient pressure. However, the perforation size must be limited and properly chosen to maintain the liquid layer as a competition between the hydrostatic pressure, the surface tension and the vapor pressure.

Let us analyze in more detail this stabilizing mechanism based on small perforations to release a small fraction of the generated vapor under the drop. A qualitative comparison of the evaporation dynamics for a liquid in the Leidenfrost state deposited on a flat surface and on a perforated surface is depicted in figure 3.8, where a droplet of radius larger than 4 times the capillary length λ_C is deposited. In the first case, the instability grows creating a bubble that can burst through the liquid surface [110], whereas in the second case, the vapor drained through the orifice releases excess pressure, which prevents the formation of bubbles. However, this orifice could deform the bottom part of the liquid surface, due to the pressure difference between the liquid and the vapor escaping through it. Then, a quantitative analysis is needed in order to estimate the maximum hole size.

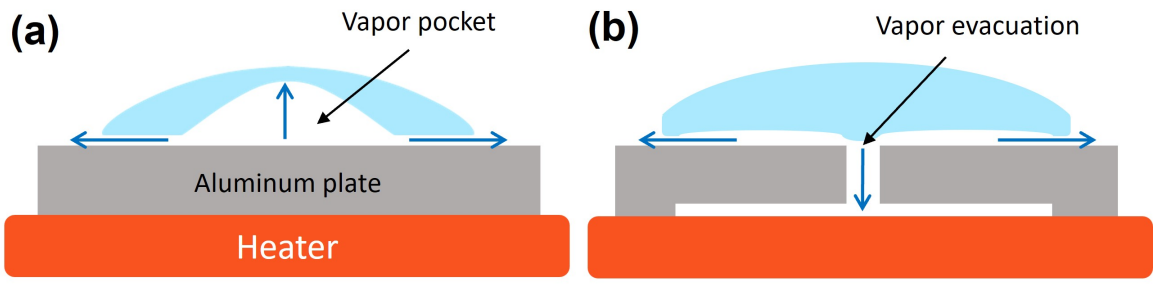

Figure 3.8: Shape of a droplet whose radius is larger than 4 times the capillary length λ_c (a) Without any escaping mechanism, a bubble grows from the central part of the liquid and bursts. (b) The droplet is stabilized by releasing part of the vapor generated from the bottom part of the liquid.

3.4.1 Maximum perforation size

The droplet shown in fig. 3.8b could be "sucked" by the hole due to the pressure difference between the bottom part of the liquid and the pressure inside the hole, which can be considered to be close to the atmospheric pressure. Let us consider a cylindrical hole of radius R_h and a hemispherical deformation of radius R above this hole, whose protuberance thickness is ϵ. These parameters are sketched in the following figure.

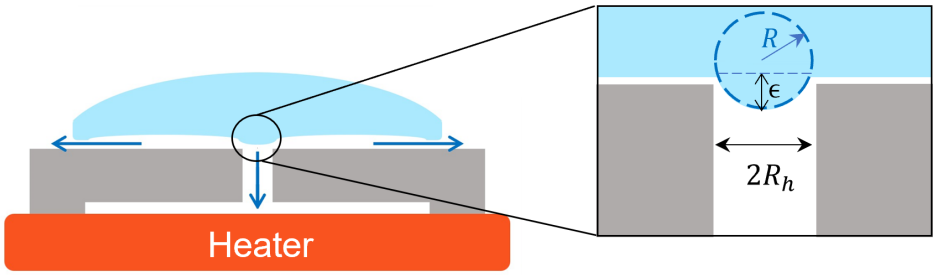

Figure 3.9: Hemispherical deformation on the bottom part of a Leidenfrost droplet placed on a holed substrate. A portion of this hemisphere of thickness ϵ is going to be deformed and pop out to compensate the hydrostatic pressure.

The equilibrium between the hydrostatic and surface tension forces gives us:

$$\rho g(2\lambda_C + \epsilon) = 2\gamma/R \tag{3.1}$$

The limit case of the previous equation corresponds to a dripping state of the liquid, where $\epsilon = R$, totally filling the hole radius R_h. Then, by replacing these parameters in the previous equation we get a second-degree equation for the hole radius R_h:

$$R_h^2 + 2\lambda_C R_h - 2\lambda_C^2 = 0 \tag{3.2}$$

This equation has two solutions: $R_{h1} = (\sqrt{3} - 1)\lambda_c$ and $R_{h2} = (-\sqrt{3} - 1)\lambda_c$. Then, the only physical solution is $R_h \approx 0.73\lambda_c$. In the case of water close to its boiling, point this corresponds to a maximum hole radius $R_h \approx 1.7$ mm.

The previous result actually overestimates the maximum perforation size that can be drilled in the substrate. The calculation was done neglecting the escaping vapor flow through the hole which generates a tangential force that could drive the liquid into the hole. Moreover, the hole size must be smaller than this limit also to prevent local boiling on the sharp hole boundary. In our experiments, we did perforations of around 1 mm in diameter.

3.4.2 Rayleigh-Taylor instability

On flat solid substrates big puddle-shaped droplets are not stable if their radius is bigger than $4\lambda_c$, and the chimney regime starts to appear as a result of the Rayleigh-Taylor

instability [135]. This value was also found in the case of droplets that are levitated on an air cushion [136] and, more recently, by means of a refined numerical study of the Leidenfrost phenomenon [158]. Here, we are going to perform a similar instability study to the one presented in [159], where they applied electric fields to suppress the instability. We consider the same axisymmetric system, including a perforation placed in the center. If the liquid–vapor interface below the Leidenfrost drop presents an unstable sinusoidal profile of the form $z(r) = \epsilon(1 + \cos(\pi r/R))$, as shown in fig. 3.10, the instability only grows if there exists an unbalance between the surface tension and the hydrostatic forces as well as the pressure drop ΔP due to the vapor loss through the orifice.

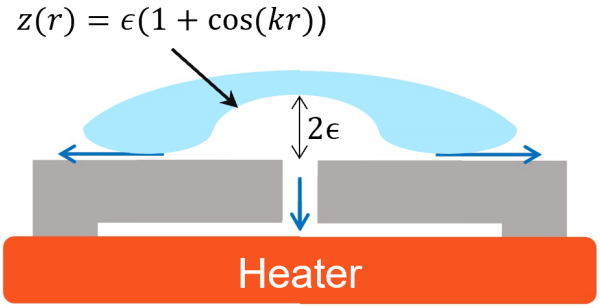

Figure 3.10: A sinusoidal perturbation growing in a perforated substrate. A bubble can grow only if the vapor pressure in the insulating layer is enough to overcome the surface tension and hydrostatic forces, as well as the pressure drop ΔP due to the vapor flow through the orifice.

By calculating the pressure difference between the center point and the edge of the vapor/liquid interface, we find the following equilibrium condition:

$$\rho g[z(0) - z(R)] + \gamma[2z''(0) - z''(R)] = \Delta P \tag{3.3}$$

The first term of the previous equation corresponds to hydrostatic pressure difference, whereas the second one corresponds to the Laplace pressure difference. After computing the derivatives, this equation simplifies to:

$$\rho g\epsilon[2 + 3(\pi\lambda_c/R)^2] = \Delta P \tag{3.4}$$

We note that in the case of $\Delta P = 0$, the equilibrium of pressures gives an estimation of the maximum stable droplet radius $R_m \approx 3.85\lambda_c$, (as found in [110]). Unfortunately, we do not know precisely the pressure drop due to the ejection of vapor through the orifice. This pressure drop depends on the flow velocities, then, we cannot easily estimate

maximum stable droplet size for a liquid placed on a perforated substrate. Nonetheless, the limit case for flat surfaces gives us an idea of the largest separation between the holes in order to prevent the formation of bubbles. However, this distance must be smaller than $R_m \approx 3.85\lambda_c$, because of the small amount of drained vapor through the orifices compared to the radial flow. A uniform hole distribution throughout the substrate will add more releasing points for the created vapor. In addition, the pressure in the vapor layer will have a spatial modulation with low pressures regions close to the position of the holes. This imposes the instabilities to occur essentially in the region between the orifices. Thus, the Rayleigh-Taylor instability is spatially restrained by the average spacing between the orifices. In figure 3.11, we show a qualitative representation of the stabilization of a big Leidenfrost puddle when the hole separation is small enough to completely suppress the Rayleigh-Taylor instability.

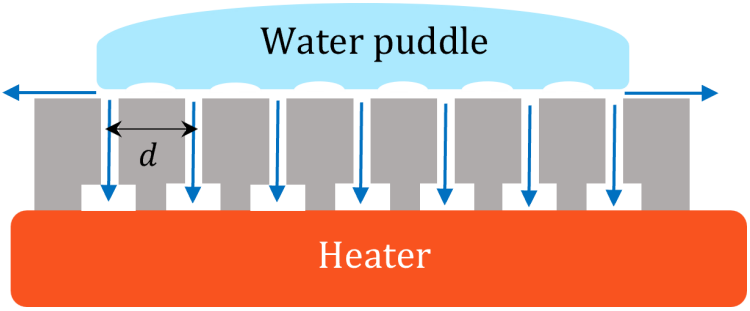

Figure 3.11: Suppression of the Rayleigh-Taylor instability for Leidenfrost puddles placed on holed substrates. A sufficiently small separation d between the holes prevents the appearance of chimneys.

3.4.3 Experimental verification

In order to verify our proposed stabilizing mechanism, we machined aluminum plates of 15 cm in diameter and 1 cm thick, with an almost negligible concavity (2 mm depth at the center). Different hole densities and distributions were obtained by drilling the plates with a homemade open-source CNC-3018 machine (see fig. 3.12a), employing a 1 mm diameter tungsten drill bit. The 3D modeling was done on OpenScad [160], then the images were converted into a g-code to be interpreted on GRBL, an open source CNC software. Figures 3.12b-c show two examples of holed substrates with different densities. The top images correspond to the top and bottom views of the same 3D design, whereas the bottom images show the top and bottom views of a final aluminum CNC machined substrate, which has higher hole density. In the bottom part of the perforated substrates, we engraved evacuation channels that connect the holes to atmospheric pressure.

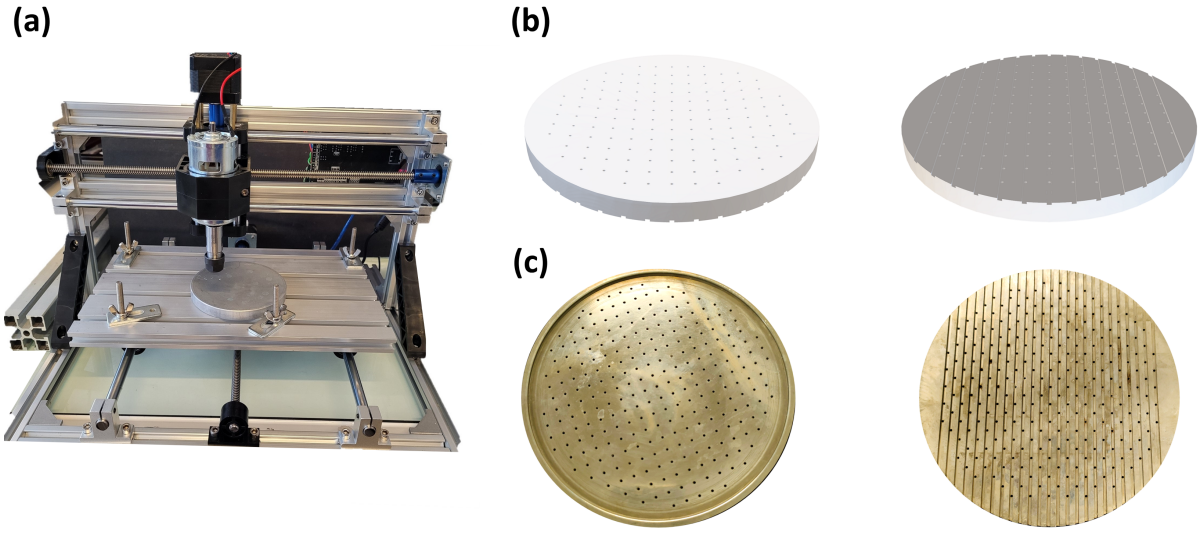

Figure 3.12: CNC machined aluminum substrates. (a) Programmable homemade CNC machine used to perforate the substrates. (b) Top and bottom views of a 3D model and (c) a final piece. Several substrates having different hole densities were machined. In the bottom part, we engraved evacuation channels that are in contact with the atmospheric pressure.

The substrates were polished and cleaned before being placed on a hot plate (Fisher Scientific, Series 11–110) at T = 400°C, corresponding to a higher temperature compared to the Leidenfrost temperature for this liquid and this substrate (around 250 °C). This temperature value also prevents spontaneous heterogeneous boiling that can occur on some perforated boundaries, due to the sharp angle geometry. We wait 15 minutes to reach a steady temperature, then, preheated deionized water at 80 °C is deposited with a syringe to get initial puddles that stabilize after a few seconds thanks to the radial flow of vapor under the liquid, but also due to the escaping vapor through the orifices that are connected to the ambient conditions.

The evaporation dynamics is recorded with a camera Basler (ac-A2040-35gc) at 200 fps, which allows us to track the individual chimney creation and bursting. Another possibility was to record the top view with an IR camera (Optris PI-400i), in order to also track the inner flows. We observe a contrasted dynamics when we increase the hole density on the aluminum substrates and for a sufficient high density, we achieved a total chimney annihilation, as shown in the infrared images of fig. 3.13, in which a puddle shaped liquid is placed on a flat substrate (fig. 3.13a) and a perforated substrate (fig. 3.13b). The infrared camera allows one to observe the temperature gradients between 85 and 95° C and the associated convection motion my means of the heat transfer between the hot substrates and the levitated liquid. When bubbles form, they appear lighter

because the thin layer of liquid heats up due to the hot vapor below whose temperature is higher than the boiling point. One can observe the quasi-steady state for the liquid when it is deposited on a perforated substrate.

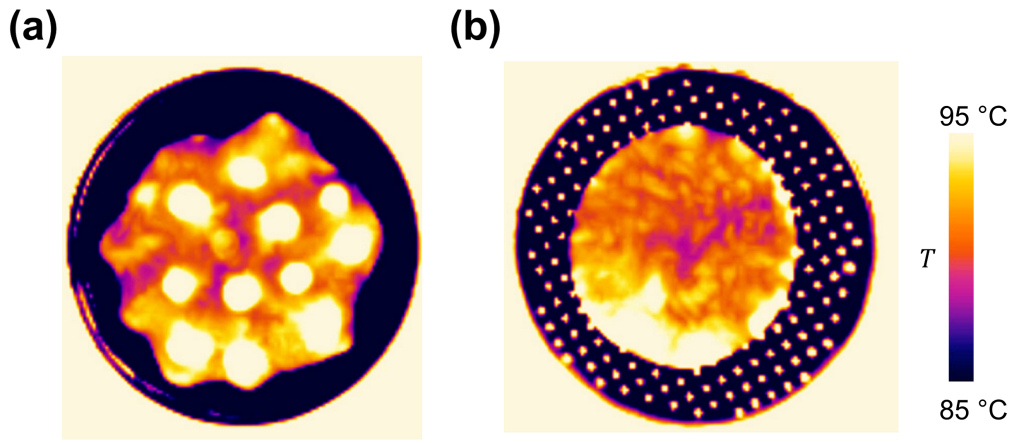

Figure 3.13: Infrared images showing the contrasting dynamics of Leidenfrost puddles. (a) A 10 cm diameter water puddle placed on a flat substrate showing yellow disks corresponding to bubbles whose temperature is approximately 95 °C. (b) A 8 cm diameter water puddle placed on a perforated substrate. The vapor flow through the orifices stabilizes the Leidenfrost water puddle on the drilled substrate. In both images, the substrates appear dark (low temperature), which is due to its IR reflection on the metallic polished surface.

A sketch of the experimental setup is shown in figure 3.14a. On the top, two cameras were placed to record visible and infrared images. In figure 3.14b, we show a comparison of the evaporation dynamics between a liquid puddle deposited on a flat plate and on a perforated plate. In both cases, the substrates were heated to reach a temperature of 400 °C. Some infrared pictures taken at the indicated times are shown to illustrate the contrast in their respective dynamics. For the non-perforated case, we observe the appearance of chimneys, whereas the holed substrate totally suppresses this regime and generates a stable slow evaporation. One can observe that the presence of holes can reduce evaporation rate compared to the flat case. However, for higher hole densities, the opposite effect is expected, as we are increasing the amount of drained vapor from the bottom part of the substrate. This is going to be discussed in the following section.

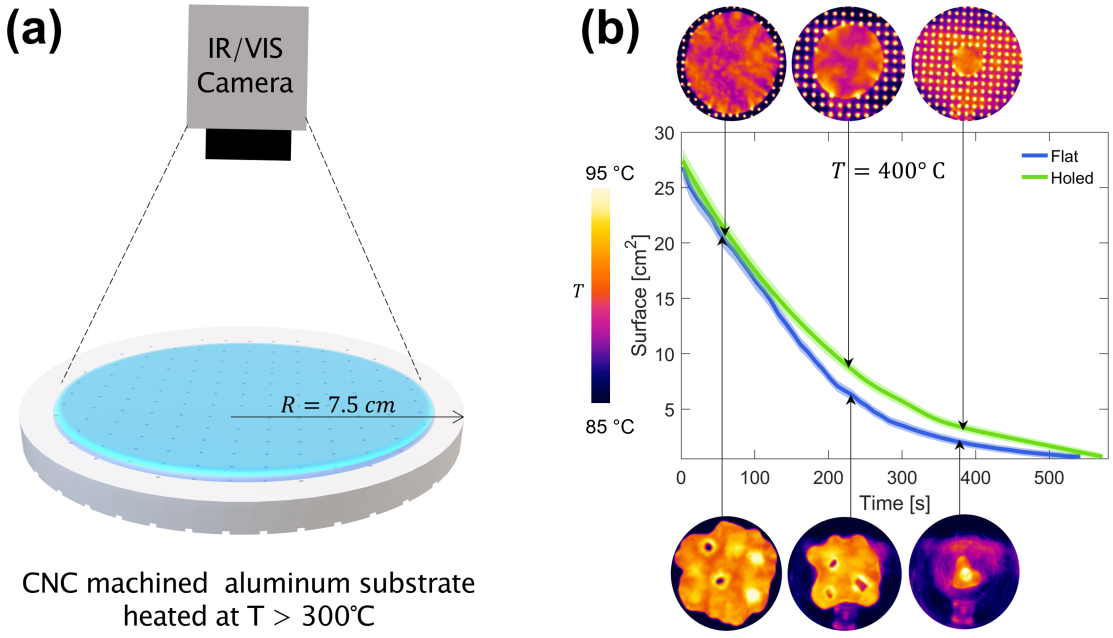

Figure 3.14: (a) Experimental setup with a visible or an infrared camera. (b) Comparison of the surface evolution for a liquid deposited on a perforated flat plate and a non-perforated flat plate which is heated to reach a temperature T = 400°C. The IR snapshots illustrate the difference in their evaporation dynamics for initial puddles of 14 cm diameter.

In order to quantify the decrease in the chimney formation as a function of the hole density, four plates with hole densities $n = 0.8, 1.2, 2$ and 2.5 hole/cm^2 were machined, then polished and heated at T= 400°C. After waiting 15 minutes to ensure thermal equilibrium, deionized water is poured on the substrates, and we follow the evaporation dynamics of puddles with same initial surface $A_0 = 34 \pm 0.1$ cm^2. We analyze the recorded videos on Matlab and we track every event corresponding to the creation or destruction of an existing chimney. In figure 3.15a, we plot the chimney production rate for the same initial puddle placed on different perforated substrates. In figure 3.15b we plot the normalized frequency of generated chimneys for averaged over 10 s. The maximum values of the histograms give us the most frequent number of chimneys present on the corresponding plate, for a given volume of liquid.

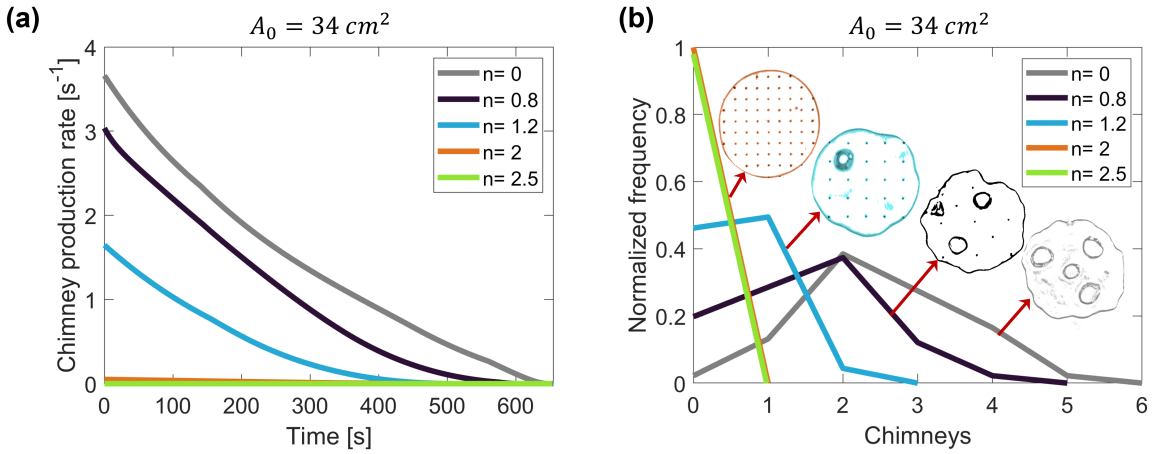

Figure 3.15: Evaporation dynamics for different hole concentrations. (a) Chimney production rate for the same puddle as a function of time. (b) Normalized frequency of generated chimneys for a puddle of area $A_0 = 34\text{cm}^2$ averaged over 10 s.

From figure 3.15a, we observe that the chimney production decreases with time as a result of the decrease of the contact area of the liquid. Moreover, the chimney production rate suddenly decreases when the hole density changes from 1.2 to 2 holes/cm^2 and is totally annihilated for hole densities larger than 2 holes/cm^2. The insets shown in fig. 3.15b, demonstrate the motion stabilization by means of this mechanism. For puddles without chimneys, the evaporation dynamics takes place in a quasi-steady state, just as the case of small droplets placed on a smooth surface [110]. Thus, we have achieved also a total stabilization of arbitrary big levitated puddles thanks to this partial evacuation of vapor under the liquid.

These results prove that the presence of holes in the substrate enabling the release of the vapor produced in the isolating layer between the puddle and the substrate can efficiently prevent the appearance of chimneys. The critical density satisfies the criterion given by the characteristic length of $4\lambda_c$ for the onset of the Rayleigh-Taylor instability (see previous section). Huge puddles can be stabilized using this technique and the maximum amount of levitated liquid is only limited by the size of our perforated substrates, but this principle can be employed to levitate arbitrary large volumes of liquid that will be only flattened by gravity, creating a liquid layer whose thickness is $2\lambda_c$.

Evaporation rate comparison

We studied the evaporation rate for the different experimental hole densities in order to be compared with the flat case. In figure 3.16, we plot the surface evolution during

the evaporation process for the same initial amount of liquid deposited on the substrates heated at 400°C. We observe that, according to the perforation densities, the evaporation rate can be slower or faster compared to the flat case, even if we have less chimney production. This variable evaporation rate can be understood from the fact that, as we increase the number of perforations in the substrate, more vapor will be released through these holes and the distance between the liquid and the substrate decreases inducing a higher rate of evaporation. However, at some point the amount of drained vapor would be higher compared to vapor evacuated by the chimneys. Thus, an optimum density can give us the slowest evaporation rate. In figure 3.16a we observe that for the available hole densities, the minimum evaporation rate is obtained for a density of $n = 1.2$ holes/cm^2. In figure 3.16b, we plot the total evaporation time for the same initial amount of liquid, for the experimental hole densities. The maximum evaporation time is obtained for a hole density $n = 1.2$ holes/cm^2, in agreement with the previous plot, confirming the existence of an optimal hole density to considerably reduce the evaporation rate of a Leidenfrost liquid.

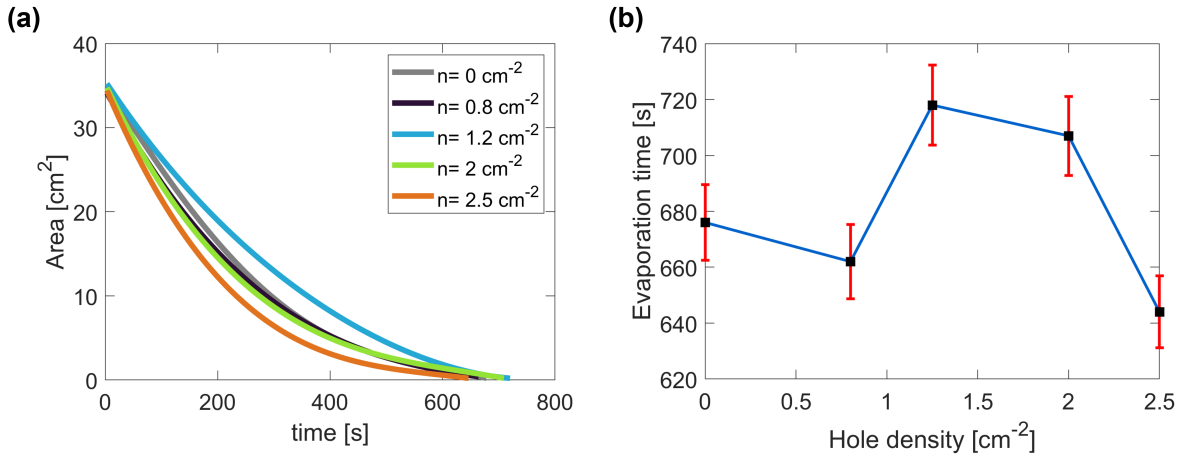

Figure 3.16: Evaporation dynamics for different hole concentrations. (a) Surface evolution as a function of time. (b) Evaporation time for the same initial volume of liquid placed on the substrates with different hole densities.

These experimental results show that with an increased density of holes, the vapor can be drained away more easily and the vapor layer is thinner which induces an increase of the evaporation rate. The decrease of the evaporation rate compared to the flat substrate is less intuitive, since a formation of bubbles should increase the thickness of the vapor layer locally and thus decrease the evaporation rate. However, the other regions of the liquid puddle are closer to the substrate and, on average, the global evaporation rate ends up being less important with a low-density perforated substrate than a flat substrate.

An attempt to reconstruct the vapor layer

The shape reconstruction of the insulating vapor layer for a liquid in the Leidenfrost state is an experimental challenge, and only an interferometric technique has been able to get a full reconstruction, employing transparent flat substrates [161]. Here, we cannot use the same interferometric method because we are working with metallic substrates. For this reason, we decided to use a technique based on total internal reflection on the lower liquid interface, where fringes are projected on a prism, which is placed on the top of the liquid. The pattern has a deformed reflection due to the liquid-vapor interface, and this is recorded with a fast camera. An example of an image obtained with this technique is shown in figure 3.17. However, the action of placing the prism on the top of liquid changes totally the dynamics as a result of the wetting on the glass surface. In particular, we noticed a random re-appearance of chimneys. In addition, this method to reconstruct the vapor layer profile is not straightforward, due to the large deformation of the interface and the constant fluctuations in space and time. However, a combination of this approach and artificial intelligence could be used to trace the geometric profile of the interface. This is a work in progress that is being developed by a group of collaborating engineers from the ESPCI.

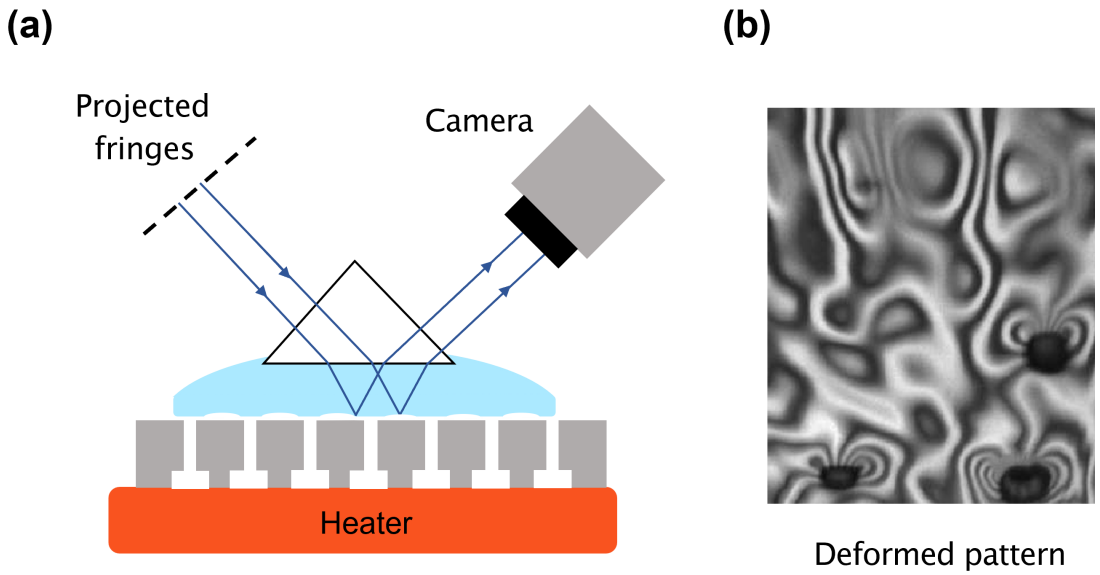

Figure 3.17: Surface reconstruction attempt of the vapor layer via the fringe projection technique. Projected fringes cross a glass prism placed on the top of the liquid and these are reflected by the deformed liquid/vapor interface. Then, the pattern is recorded by a high-speed camera. Unfortunately, the dynamics is perturbed by the hydrophilic glass surface, which induces the re-appearance of some chimney events.

3.4.4 Numerical simulations

We performed numerical simulations of the Leidenfrost phenomenon for liquids placed on holed substrates. To do that, we solved the Navier-Stokes equations adapted to these experimental conditions.

First, we consider the case of a Leidenfrost puddle placed on a single-hole substrate. This system has a radial geometry, and the liquid deformation is modeled by a Level-Set method. This technique was introduced for the first time in [162], and allows one to include the surface tension forces and track the topological changes of the interfaces. The details of this technique can be found in [163]. The main idea is to represent the interface by a certain isocontour of a globally defined function, the level set function, which is coupled with the system of partial differential equations. This method has been already used to study the Rayleigh-Taylor instability [164], and other fluid dynamics problems including capillary forces [165, 166]. The numerical simulations were done in COMSOL Multiphysics, a software based on finite element method to solve partial differential equations [167]. Our model is easy to implement, thanks to the Computational Fluid Dynamics interface. This software has been already used to simulate the propulsion mechanism for a Leidenfrost droplet that is deposited on a ratchet patterned substrate [151], obtaining a good agreement with the experiments [101]. A more refined model including thermal contributions was recently described in [158], showing very slight discrepancies compared to the model that neglect thermal effects.

The numerical simulations of the Leidenfrost puddle placed on a single-hole substrate were done with an initial spherical drop of volume $V = 32\pi\lambda_c^3$ in order to create a puddle-shaped droplet of radius $R = 4\lambda_c$, after being flattened by gravity. The droplet is placed 1 mm above the center of the holed substrate, in which we place a uniform vapor flow escaping in the vertical direction with different constant velocities in the range of $v \in [1, 10]$ cm/s. This velocity range corresponds to the typical downwards vapor velocity of a Leidenfrost droplet placed over a flat substrate [151]. In the middle of the substrate, we draw a hole of different radius $R_h \in [0, 2]$ mm. The simulations employed a non-uniform triangular mesh of variable size for the vapor and liquid phases, as their thicknesses differ from two orders of magnitude. Both phases had approximately 10^5 elements to obtain the convergence of the finite element built-in solver. The time discretization was done by selecting a time step of $\Delta t = 1$ ms, which is small enough to capture the full dynamics. Initially, the viscosity of the liquid is increased 10 times and then decays exponentially to

its real value during the first 0.5 s of the numerical simulations. This is done in order to prevent convergence crashing, in accordance with [158].

The numerical study considers a uniform vapor injection from the substrate surface that is localized below the liquid. This vapor flow will deform the droplet surface and will create similar conditions compared to the ones found in the Leidenfrost phenomenon. This comparison has been already used in [136] to predict the maximum size of drops levitated by an air cushion. It has been found that, for this levitating mechanism, the critical radius is $R_c \approx 4\lambda_c$, for which the chimney regime starts to appear. This value is approximately the same value found in [110], for Leidenfrost droplets. Thus, this numerical model can be implemented to study the Rayleigh-Taylor instability of a holed substrate to give us relevant information about the maximum hole size that can be perforated in the solid substrate. Typical Leidenfrost experiments are done with drop sizes ranging from 1 mm to a few cm. The corresponding insulating vapor layer has a thickness having two orders of magnitude smaller, which represents a computational challenge. This is the reason why we use the model without including the heat transfer between the substrate and the liquid. Thus, we only consider the liquid levitated by a cushion of vapor created at a rate fixed by the substrate temperature. Despite the simplification, this model can be useful for predicting the Rayleigh-Taylor instability, as it was done for the flat case in [136].

The figure 3.18 shows a comparison of the numerical results obtained for a spherical droplet of radius $R = 7$ mm placed on three different substrates with vapor flowing in the perpendicular direction at a velocity of 1 cm/s. This flow is redirected to the radial direction, as a result of the confinement between the liquid and the substrate. Due to gravity, the droplet acquires a puddle-like shape of radius $R_0 \approx 4\lambda_c$. In fig. 3.18a we show the formation of a chimney when this droplet is placed on a flat substrate. In this numerical simulation the chimney bursts at the center of the droplet. In fig. 3.18b, we observe that the droplet is stable on a substrate having a perforation radius $R_h \approx 1$ mm. The perforation prevents the Rayleigh-Taylor instability and no chimney is observed. In fig. 3.18c we observe an unstable regime for a droplet placed on a substrate having a hole radius $R_h \approx 2$ mm. In this case, the droplet starts dripping through the hole and, eventually, is totally drained through the orifice as a result of the liquid weight.

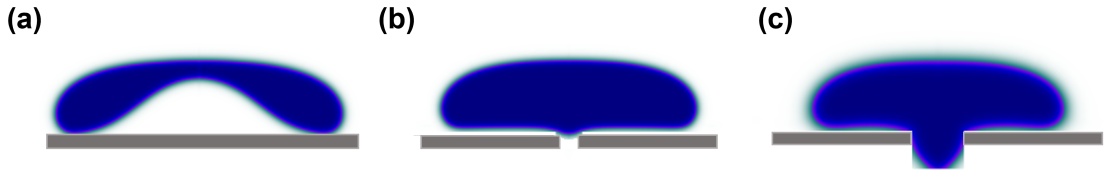

Figure 3.18: Morphology of a Leidenfrost puddle-shaped droplet of radius $R = 4\lambda_c$, placed on different substrates. The images correspond to the numerical results obtained with COMSOL Multiphysics. (a) Droplet placed on a flat surface presenting a chimney as a result of the Rayleigh-Taylor instability. (b) Stable droplet when placed on a 1 mm diameter holed substrate. (c) Unstable droplet drained through a perforated substrate with a 2 mm diameter hole.

According to the numerical simulations, the droplet can present a chimney regime if the hole size is small enough to neglect the draining of vapor through the orifice. An opposite scenario can also occur if the hole size is big enough to allow a full draining of liquid through the orifice. Between these two regimes we observe the regime experimentally studied, in which the small fraction of drained vapor can suppress the Rayleigh-Taylor instability and prevent bubble formation. The results of this numerical analysis confirm the theoretical predictions provided in the previous section. However, for the case of water, we experimentally observed that if the holes are larger than 1.5 mm in diameter some spontaneous boiling can occur on the sharp edges of some orifices. The numerical simulations were done neglecting the substrate temperature, then, they predict a larger possible perforation size without having draining of liquid through the orifices. This can be understood if we take a look of the flow of a droplet placed on a holed surface. The figure 3.19 shows the streamlines for the three different possible scenarios. Figure 3.19a shows the flow field for the case of a drop placed on a flat substrate. We observe that the vapor pushes the center area of the liquid in the upper direction and the surface tension forces cannot compensate the driven liquid that ends with a chimney explosion. Figure 3.19b shows the flow field for a drop placed on a perforated substrate with a 1 mm diameter hole. We observe that the vapor pushing the liquid is compensated by the evacuation of a part of the vapor and the shear stress forces are not big enough to create a chimney. Figure 3.19c shows the flow field for a droplet placed on a perforated substrate with a 4 mm diameter hole. In this case, we observe that the capillary and vapor pressures are not big enough to compensate the hydrostatic pressure, which drives the levitated liquid to pass through the orifice.

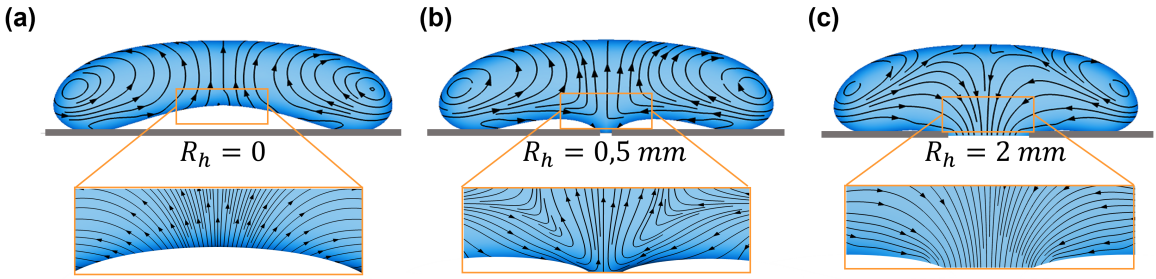

Figure 3.19: Streamlines showing the flow inside of a Leidenfrost droplet that is deposited on substrates whose perforation radius are: (a) $R_h = 0$ mm, (b) $R_h = 0.5$ mm, and (c) $R_h = 2$ mm. The close-ups are added to show the flow near the holes in more detail.

The flow field inside of Leidenfrost droplets has been recently study to understand the propelling mechanism of the so-called Leidenfrost wheels [168]. Our simulations reproduce similar inner flows even if we have neglected the thermal convection. Thus, the vapor flow under the liquid is the main responsible for creating an inner flow by means of its viscosity. The level-set method allowed us to get insight about the convection that occurs in a Leidenfrost droplet and represents a very powerful technique for a numerical analysis of this phenomenon on different substrate geometries.

3.5 A new propelling mechanism

Until now, we have shown that we are able to stabilize an arbitrary large liquid puddle by means of the vertical release of vapor in the insulating layer. In this section, we are going to show how we can take advantage of this stabilizing mechanism for also controlling the horizontal motion of a large puddle of liquid. The main idea is to break the rotational symmetry of the perforated pattern. This will induce an asymmetric flow which will propel the whole levitated liquid, as it has been already demonstrated for ratchet based propelling mechanisms [154]. In our case, we can achieve this, by drilling a swirl-shaped pattern (see fig.3.20a).

3.5.1 Experimental realization

Different swirl shaped engines were designed in OpenScad and then drilled with our homemade CNC machine. An example of a final holed patterned engine is shown in figure 3.20a. This simple asymmetric design was able to turn the whole liquid, being capable of reaching angular speeds up to around 4 rad/s (fig. 3.20c). The rotation speed

was measured by tracking the rigid rotation of a piece of paper placed on the top of the liquid (see fig. 3.20a). Additionally, it is possible to obtain the velocity field over the entire puddle using the infrared camera. In figure 3.20b, we plot the velocity field, obtained from the analysis of the IR videos with PIV-Lab [169]. The averaged flow rotation gives us a rigid rotation with a similar value compared to the paper strip technique. We also studied the influence of the substrate temperature on the rotation speed of the puddle driven with this propelling technique. Figure 3.20c shows the rotation velocity as a function of the temperature of the substrate. We observe a steady decrease of this rotation with increasing temperature.

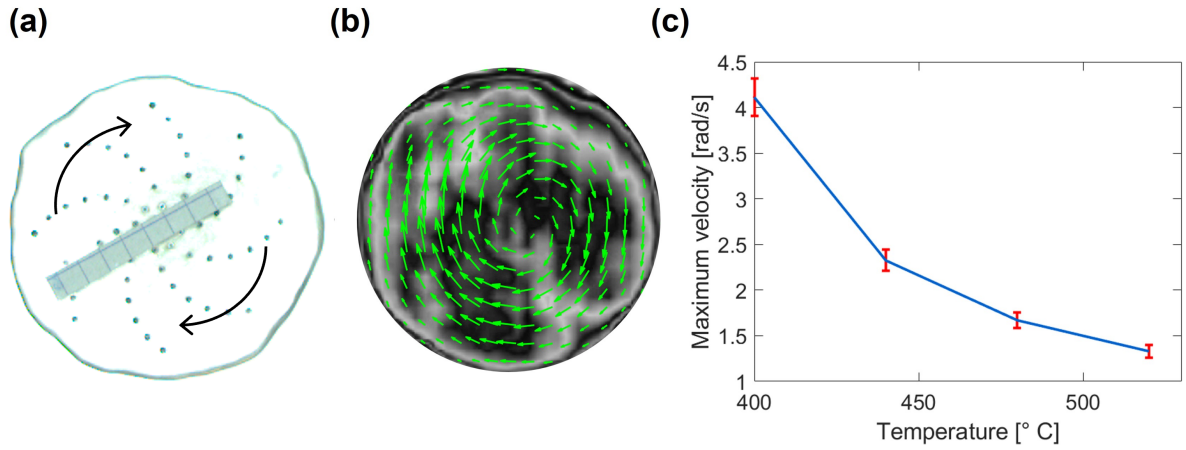

Figure 3.20: A new Leidenfrost engine for arbitrary large volumes of liquid. (a) A top picture of a big puddle of liquid that is rotating on the aluminum substrate having an asymmetric swirl-like pattern. A small piece of paper is placed on the top to track the global rotation. (b) Flow field obtained with PIVlab [169] from an IR video that follows the evolution of the turning liquid placed on this engine. (c) Maximum angular velocity for different substrate temperatures.

The rotation takes place in the opposite direction compared to the case of solid substrates that are engraved with a similar swirl-like pattern [154]. This happens because the vapor flow is the responsible propelling mechanism, originating from the creation of a shear stress which constrains the liquid to follow the vapor flow. This propelling mechanism is analogous to that encountered in ratchets and other asymmetric designs [120, 153]. For each fabricated Leidenfrost engine, we found that the maximum rotating speed decreases with the substrate temperature. This could seem counter-intuitive as we are heating more and we are getting less mechanical energy. A possible explanation is the increase of the radial flow component for the vapor at high temperature due to the increase of the net evaporation flux in the cushion layer (see fig. 3.21a).

3.5.2 Numerical simulations

We performed numerical simulations in order to study the proposed propelling mechanism. The simulations are based on the numerical model presented [151], where they neglect the liquid deformation. The thermal effects are also neglected and we consider a vapor flow going in the upward vertical direction with a velocity of 5 cm/s. The simulations were performed on COMSOL multiphysics, employing the CFD module to solve the steady version of the Navier-Stokes equations in 3D, which are enough to demonstrate a net propulsion. We consider a non-slip condition on the top layer, corresponding to the bottom part of the liquid phase, and also a non-slip condition for the bottom part which corresponds to the substrate surface. The vapor thickness is set to 100 μm, corresponding to the order of magnitude of the insulating vapor layer thickness [8].

Three different swirl-like engines were created in OpenScad, then they were imported in COMSOL. Examples of the designed engines are shown in figure 3.21, where three swirl designs with 6, 8, and 10 spiraling branches are depicted. The branch curvature was arbitrary chosen to break the rotational symmetry. The black arrows are tangential to the streamlines and indicate the direction of the vapor flow. The color map represents the pressure distribution in the insulating vapor layer. At the bottom of this figure, we place the corresponding contour plots for the vapor velocities in each respective plate, the maximum values for both colormaps are colored in red, whereas the minimum values are colored in dark blue.

The numerical simulations illustrate the competition between the outside radial escape of the vapor and its flow through the orifices. From fig. 3.21b, we note the existence of areas with a minimum flowing velocity. The radial escaping flow is isotropic and radial. It does not generate a global rotation. On the contrary, the flowing vapor that enters the swirl pattern can generate a global rotation of the levitated liquid. The liquid viscosity is the responsible of this propulsion, in analogy to what has been argued for the ratchet surfaces [151].

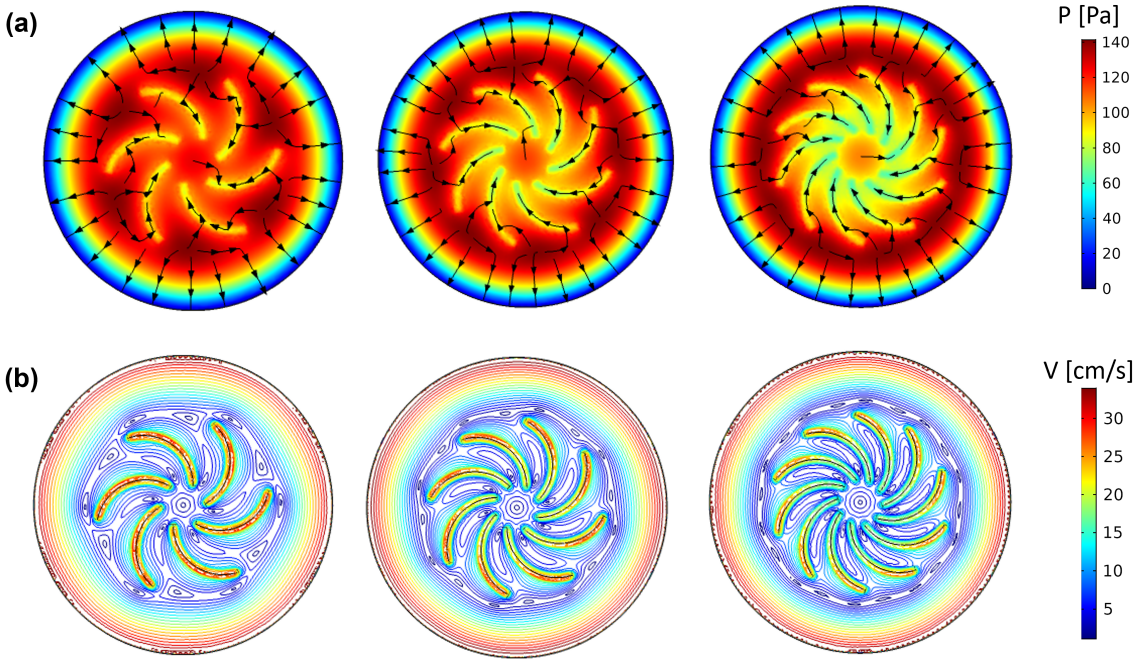

Figure 3.21: Numerical validation of the propelling mechanism due to an asymmetric evacuation through swirl-like patterns that are removed from the solid substrates. (a) Swirl engine designs with 6, 8, and 10 spiraling branches. The branch curvature was arbitrary chosen to break the rotational symmetry. The black arrows are tangential to the streamlines and indicate the direction of the vapor flow. (b) Contour plots for the vapor velocities in each respective plate. The maximum values for both colormaps are colored in red, whereas the minimum values are colored in dark blue.

3.5.3 Propulsion force estimation

Leidenfrost liquids levitate on a vapor layer whose thickness is much smaller than the characteristic liquid size. Then, the lubrication approximation [170] can be employed to estimate the propelling force of a liquid placed on a perforated substrate. This approximation is not verified inside the holes, but considering their negligible area compared to the area covered by the puddle, the global flow profile can be well described under this approximation. This will give us an order of magnitude of the torque applied to the levitating liquid.

The vapor flow can be described by the continuity equation combined with the incompressible and steady form of the Navier-Stokes equations. Under these conditions and using cylindrical coordinates, we show in Appendix E that the vapor pressure verifies:

$$\frac{1}{r}\frac{\partial}{\partial r}\left(r\frac{\partial P}{\partial r}\right)+\frac{1}{r^2}\frac{\partial^2 P}{\partial \theta^2}=\frac{12\eta v_n}{\delta^3} \tag{3.5}$$

where η is the vapor viscosity, δ the vapor layer thickness, and v_n the normal vapor flow which is emanating from the bottom side of the liquid puddle, as a result of the phase transition in the region closest to the hot substrate. One can note that equation 3.5 corresponds to Poisson's equation $\Delta P = 12\eta v_n$, whose solution can only be found numerically for a given engine geometry. In figure 3.22a, we show the results of the numerical solution of eq. 3.5 for a swirl-like engine having 8 branches, where $v_n = 1$ cm/s and $\delta = 0.1$ mm. We added the streamlines to indicate the vapor flow direction. The pattern seems more complex compared to the engine designs depicted in fig. 3.21. However, the streamlines demonstrate a clock-wise rotating motion.

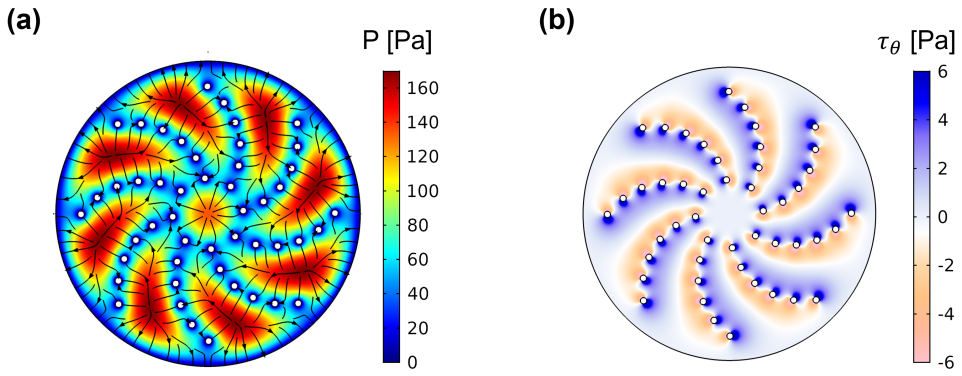

Figure 3.22: Numerical estimation of the propulsion force of a swirl-like engine having 8 branches. (a) Pressure distribution and streamlines indicating the flow direction. (b) Torsional shear stress distribution acting on the levitated liquid.

The torsional shear stress τ_θ can be approximated as $\tau_\theta \approx \eta\frac{\langle v_\theta \rangle}{\delta}$. This can be written in terms of the pressure gradient in the angular direction (see Appendix E):

$$\tau_\theta \approx \frac{\delta}{12r}\frac{\partial P}{\partial \theta} \tag{3.6}$$

In figure 3.22b we plot the torsional shear stress distribution acting on the levitated liquid, for the case of a normal vapor flow $v_n = 1$ cm/s and $\delta = 0.1$ mm. From this, we can calculate the magnitude of the total torque acting on the levitated liquid of radius R:

$$||\mathbf{T}|| = \int_0^R r^2 dr \int_0^{2\pi} \tau_\theta \, d\theta \tag{3.7}$$

This torque generates an angular acceleration α that can be obtained from the rotational law of motion, which gives us:

$$\alpha = \frac{2||\mathbf{T}||}{\rho_l \pi R^4 \lambda_c} \tag{3.8}$$

where ρ_l is the liquid density and λ_c its capillary length. From this numerical simulation we obtained $\alpha \approx 0.1$ rad/s^2, which corresponds to the maximum angular acceleration because the actual experimental system has a non-negligible friction. In our experiments we found a maximum $\alpha \approx 0.08$ rad/s^2, which was measured from the recorded videos. Thus, the angular velocity found numerically has the same order of magnitude compared to that measured experimentally.

3.5.4 Engineering the liquid motion

The propelling mechanism described above could be used to generate complex dynamics thanks to a controlled flow of the vapor from the bottom part of the liquid which, in the present case, results from the Leidenfrost effect. Let us illustrate this idea with an alternating rotation, that, in principle, would be obtained if we drill swirl-like patterns with opposite chirality on the same aluminum substrate, as shown in figure 3.23. We added a small laser-cut piece of paper in the shape of a dolphin to help the visualization of the global liquid motion. The substrate was heated to reach a stable temperature of 400°C and colored water was poured until reaching puddle radius of 14 cm in diameter. This corresponds to a bigger area compared to the drilled region. We recorded the evaporation process with the same camera that was employed in our previous experiments, and we noted that different dynamics appear according to the liquid size compared to the perforated region.

For puddles that are larger than the perforated pattern, we observed a chimney instability on the region external to the drilled area and no global rotation was observed (see fig. 3.23a). Then, when the puddle size is comparable to the one of the region having the external swirl pattern, a counterclockwise rotation occurs (see fig. 3.23b). Finally, when the puddle reaches the internal swirl of opposite chirality, a clockwise rotation takes place (see fig. 3.23c).

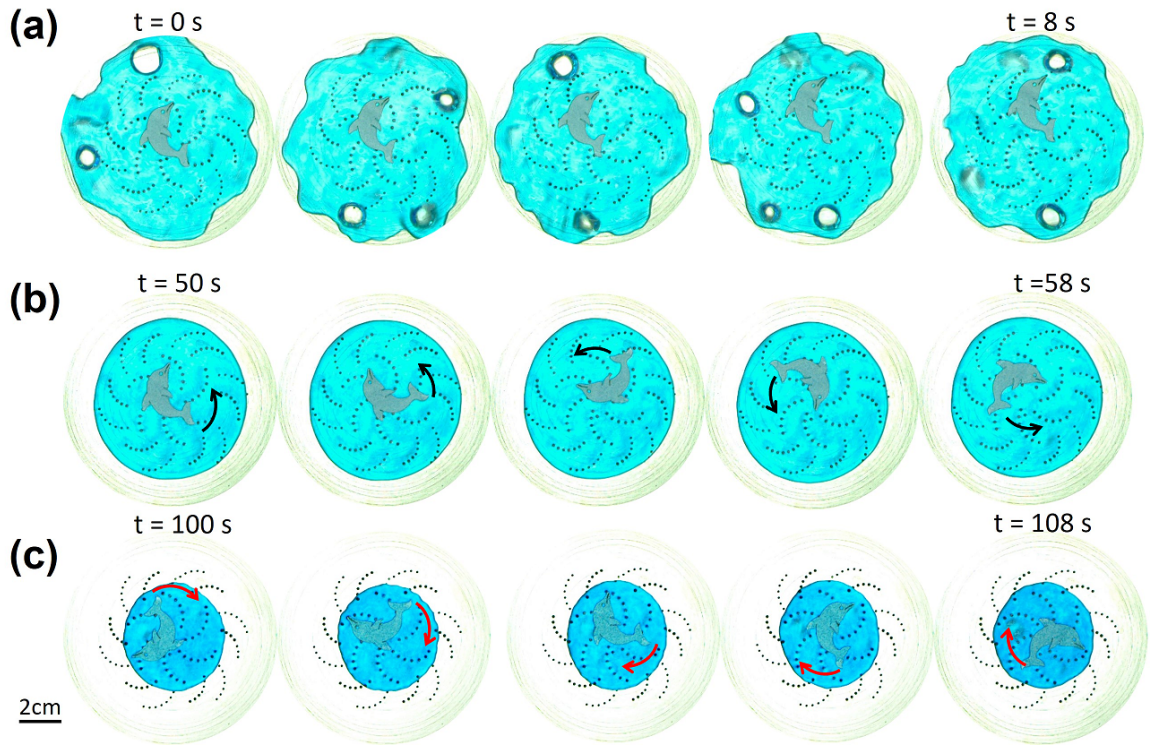

Figure 3.23: Snapshots of a large rotating Leidenfrost puddle placed on two opposite concentric swirls. (a) Levitating puddles larger than the perforated pattern present a chimney instability on their perimeter and no rotation is observed. (b) A counter-clockwise rotation occurs when the puddle size reaches the external swirl pattern. (c) A clockwise rotation takes place if the puddle fits into the internal swirl.

This was only an example of engineered liquid motion that we could design by placing opposite chiral perforated patterns. Different designed configurations can take advantage of this propelling mechanism, which could be particularly useful to control the motion of quasi-frictionless liquids. Moreover, the combination of an asymmetric pattern and some uniform perforations can lead to the creation of massive Leidenfrost engines, which could move arbitrary large levitated liquids, as there is no limitation in size for this mechanism. In the case of these large applications, we could use air cushion systems and directly pattern the surface in order to achieve any programmed motion for the levitated object.

3.6 Conclusions and perspectives

In this chapter, we were interested in stabilizing and controlling the motion of large volumes of liquids in the Leidenfrost state. This was possible thanks to a selective evacuation of a small fraction of the insulating vapor, created under the liquid, by using

a perforated substrate. We achieved a complete annihilation of the chimney regime, which is always present in large Leidenfrost puddles, by releasing a part of the vapor that nourishes the insulating layer. For each temperature, there exists a minimum hole concentration capable of preventing the bubble formation. On one hand, holes need to be small enough so that the Laplace pressure prevents the liquid to drain through the holes. On the other hand, the density of holes must be high enough to avoid the Rayleigh-Taylor instability of the lower interface of the puddle. Under these conditions, the liquid in the Leidenfrost state evolves with an almost steady evaporation.

Numerical simulations were performed with a simplified model that neglects the thermal effects and considered the Leidenfrost puddle shaped liquid as if it was levitating on a pre-existing vapor cushion. The numerical solutions of the Navier-Stokes equations, coupled with the surface tension forces, were able to give us important qualitative and quantitative insights for the maximum hole size that is needed to stabilize the levitated liquid. These simulations were also a crucial tool for demonstrating our propelling mechanism based on an asymmetric evacuation of vapor below the liquid. In the future, we can refine this model to include thermal effects, but we will need to overcome some important computational challenges. In this regime we cannot employ the lubrication approximation and we will face the full Navier-Stokes equations coupled with thermal effects and surface tension forces.

An experimental demonstration of a global directed motion for the whole levitated liquid was performed. To achieve this, we design and drill asymmetric patterns, allowing us to create a stable "Leidenfrost engine" that set in rotation arbitrary large volumes of liquids. The proposed engine represents an alternative to set into motion a liquid in the Leidenfrost state compared to the ratchet-based and other propelling mechanisms. Furthermore, this propelling method can be engineered to generate complex motions. In our case, alternating rotations were obtained by drilling swirl-like shapes of alternating chirality on the same aluminum substrate. This could be interesting for creating automatic locomotive processes in industry or increasing the complex motion capabilities for liquids.

The Leidenfrost engine efficiency could be improved, and the numerical simulations developed in this work represent a starting point. In order to get the most efficient engine, we must perform more simulations, with an exhaustive design testing of different asymmetric vapor evacuation patterns. Numerical analysis will avoid a direct experimental testing on a very limited number of perforated substrates.

Conclusions

Active systems have a rich phenomenology with multiple fields of application as it was illustrated in this thesis. We have been interested in studying three active systems that can be useful for robotic exploration, wave manipulation and propulsion liquids in the Leidenfrost state.

In the first part, we have investigated the usefulness of random motion to measure and recognize shapes without seeing them. For this purpose, we have employed the tools provided by statistical geometry. In particular, we used the mean chord theorem, which is one of the most important results of this branch of mathematics. This statistical invariant allows us to calculate the ratio between the area and the perimeter of an arbitrary region when it is crossed by straight or brownian trajectories. We extended the formula for closed-loop trajectories, which gives a criterion for knowing when a shape can be totally inscribed in a region. Afterwards, we have found a second statistical invariant which gives us the area of an arbitrary region when it is crossed by straight trajectories. By combining these two formulas, we can retrieve the area and the perimeter of an arbitrary 2D region, which can be non-convex and non-connected. We implemented this result to robotic exploration, using a simple, non-oriented robot that randomly explores an arbitrary region. We have shown that, from simple one-dimensional measurements, a blind robot can acquire global geometric information of the explored region. In this case, the robot was able to determine the area and perimeter of several explored regions, and then employed these parameters in a robust strategy to recognize the shape, using a shape dictionary. Finally, this strategy was proven to be useful for reading letters and words in a text.

In the second part, we have studied the propagation of waves through a medium capable of performing an abrupt change of damping. We showed that the application of a damping shock can create a time reversed version of an initial propagating wave. This is only a result of a quick modification of the initial conditions at the application time of a damping pulse. The initial traveling wave splits into two counter-propagating waves, one of them corresponds, up to a factor one half, to the time-reversed version of the initial propagating wave. The other one is the same initial propagating wave multiplied only by a factor of one half. This approach offers an alternative to the instantaneous time mirror technique, in which a sudden disruption in the propagating medium generates two

counterpropagating waves. We implemented this time-reversal approach using an array of repelling magnets placed on an air cushion to remove the damping. Phononic waves in this 2D crystal were time reversed by inducing a sudden freezing and release of the magnets.

The proposed time reversal mechanism is a general concept that could be applied to any type of waves by an abrupt change in the damping of the corresponding wave field. Unlike other time-reversal methods, this method has a higher fidelity, because the backpropagated wave is proportional to the time-reversed version of the initial propagating wave. From this perspective, this technique has no spectral limitations and can be applied to broadband wave packets. The only condition is to be able to apply the damping shock fast enough compared to the wavefield velocity. Then, this represents a challenge for time reversing electromagnetic waves with this technique. Finally, we present an interesting application of successive damping shocks, which can annihilate specific monochromatic components. This represents a new wave-shaping mechanism, which may be interesting for tailoring specific frequencies of a spectral broadband wave.

In the third part, we were interested in the stabilization and propulsion of large volumes of liquids in the Leidenfrost state. This was possible thanks to a partial drainage of the vapor present in the insulating layer. For this purpose, we employed a homemade machine to drill small holes in solid substrates, which had to be connected to ambient pressure. Thanks to this, we managed to prevent the chimney regime, above a given concentration of holes, which is associated to the Rayleigh-Taylor instability. Under these conditions, the liquid evolves with an almost steady evaporation. Numerical simulations were also carried out to solve the Navier-Stokes equations coupled to the surface tension forces. These simulations corroborated our mechanism of liquid stabilization in the Leidenfrost state. Subsequently, we modified the hole distribution to break the rotational symmetry, achieving a new propelling mechanism for liquids in the Leidenfrost state. Since the chimney regime disappears, our mechanism generates a global rotation of arbitrarily large liquid volumes. Finally, we have fabricated substrates with different asymmetric hole distributions which could generate complex motions, such as alternating rotations. This shows that the design of the hole patterns makes it possible to engineer the desired movement of the liquid, which is particularly interesting for creating automatic locomotion processes in industry or fluidic devices. The optimization of this propelling mechanism by means of more engineering design could create an alternative way to propel large amounts of liquids.

Appendices

A

The mean arc length theorem for closed loop trajectories

Objects and properties in integral geometry are quantified by means of the kinematic dK-measure [16]. It is a measure invariant under rigid transformations. In the following, we designate the explored bounded domain Ω_1 with an area A_1 and perimeter P_1 and the trajectory by $\partial\Omega_2$ defined as the contour of a second domain Ω_2 of area A_2 and perimeter P_2. We restrict the Ω_1 topology to connected domains without internal holes.

A region $\Omega_1$is fixed in the frame XY while a contour $\partial\Omega_2$ is placed in a moving frame X'Y', that can perform rigid transformations in relation to XY. These are performed by a rotation $d\theta$ and a translation along (dx, dy) (see Fig. A.1). The kinematic measure of a function f relating the domain Ω_1 and the replicas of the contour $\partial\Omega_2$ is defined by the integral $f(\Omega_1, \Omega_2)dK$ over all the rigid transformations of $\partial\Omega_2$, where $dK = dxdyd\theta$ is the kinematic density. The integration is restricted to the situations in which whether $\partial\Omega_2$ or Ω_2 overlaps the region Ω_1.

Let us recall two central theorems of integral geometry. The first theorem is the Blaschke's formula which gives the kinematic measure of the length of congruent contours inside a domain [16]. The kinematic measure of the arc length $s(\partial\Omega_1 \cap \partial\Omega_2)$ that lies inside of the domain Ω_1 for a replica of the contour $\partial\Omega_2$ is given by:

$$S = \int s(\Omega_1 \cap \partial\Omega_2)dK = 2\pi A_1 P_2 \tag{A.1}$$

The integration is realized over all points in Ω_1, for all possible replica of Ω_2 such that $\partial\Omega_2 \cap \Omega_1 \neq \emptyset$.

The second theorem, called Poincare's formula [16], refers to the number of intersections between an arbitrary curve of finite length and the homogeneous and isotropic replicas of

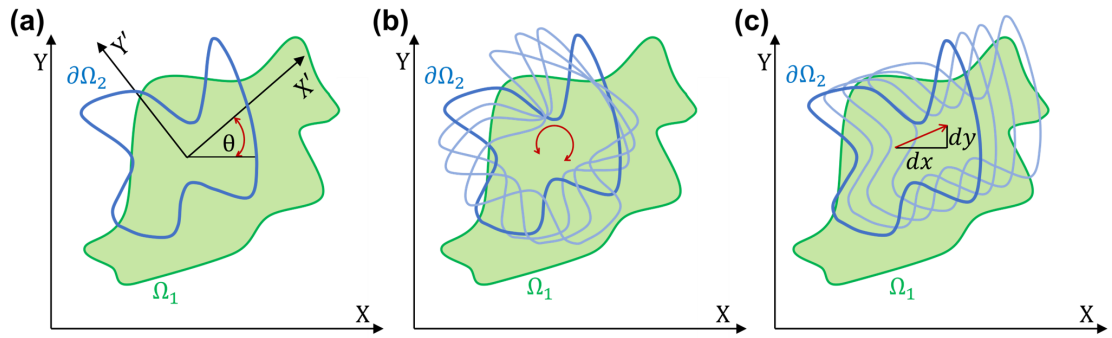

Figure A.1: Schematic representation of the measure of a domain Ω_1 by rigid transformed replicas of a contour $\partial\Omega_2$ [4]. (a) The region 1 (light green) is fixed in the frame XY, while the contour $\partial\Omega_2$ (dark blue) is placed in a moving frame $X'Y'$ which can perform a rigid transformation relative to XY. Replicas of $\partial\Omega_2$ (light blue) are obtained by (b) rotations $d\theta$ and (c) by translations along the vector (dx, dy).

another arbitrary curve. The kinematic measure of the intersections n of the contour of domain Ω_1, $\partial\Omega_1$, with the replicas of the contour $\partial\Omega_2$ is given by:

$$N_i = \int n(\partial\Omega_1 \cap \partial\Omega_2) dK = 4P_1P_2 \tag{A.2}$$

The integration is realized over every point in Ω_2, for all possible replica of Ω_2 such that $\partial\Omega_2 \bigcap \partial\Omega_1 \neq \emptyset$.In the case of closed contours $\partial\Omega_2$, n is an even number for each intersecting arc. Hence, the N_i is twice that of the number of intersecting arcs.

Provided that no contour is fully included in the domain, which would have no crossing with the boundary of $\partial\Omega_1$, $N_i/2$ is exactly the number of arcs that are involved in eq. 1 to compute S. Hence, when this condition is fulfilled, the mean value arc length $\bar{s}$ for closed contour trajectories is thus given by the ratio of S (eq. A.1) over $N_i/2$ (eq. A.2). This yields to:

$$\bar{s} = 2\frac{S}{N_i} = \frac{\pi A_1}{P_1} \tag{A.3}$$

This is a generalized Cauchy formula valid for any arbitrary closed trajectory exploring any arbitrary bounded domain whether convex or not, provided no trajectory can be fully included in the domain.

B

Demonstration of Crofton's formula

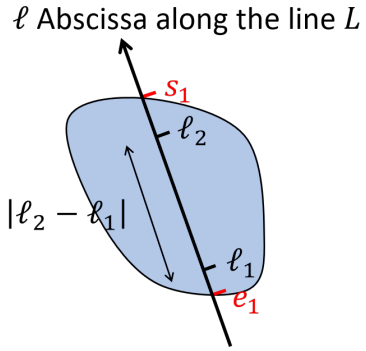

Figure B.1

We define a convex domain Ω of surface A. We denote $\partial\Omega$ its external border and P_{ext} the length of $\partial\Omega$. We consider a line L intersecting Ω. A point belonging to the line L is identified by its curvilinear abscissa ℓ along the line. For every line we denote e_1 and s_1 the curvilinear abscissa at which the line enters and exits the domain. Such a configuration is illustrated in the Figure B.1.

We consider P_1 and P_2 two points belonging to a line L and being inside the domain. ℓ_1 and ℓ_2 refer their curvilinear abscissa. We denote r the distance between P_1 and P_2. Following [16], for any given integer n, we consider the integral

$$J_n = \int_{(P_1,P_2)\in\Omega\times\Omega} r^n d^2P_1 d^2P_2 \tag{B.1}$$

We remark again that for $n = 0$

$$J_0 = \int\limits_{(P_1,P_2)\in\Omega\times\Omega} d^2P_1 d^2P_2 = \int\limits_{P_1\in\Omega} d^2P_1 \times \int\limits_{P_2\in\Omega} d^2P_2 = A \times A = A^2. \tag{B.2}$$

The streamline of the demonstration is as follows. We calculate first J_n in term of the internal chords and will equate the result with Eq. B.2 for the specific case $n = 0$.

$d^2P_1 d^2P_2$ can be expressed in the system of the line coordinates with a Jacobian given in [16]

$$d^2P_1 d^2P_2 = |\ell_2 - \ell_1| d\ell_1 d\ell_2 dL \tag{B.3}$$

with dL being the Poincaré kinematic measure. It gives

$$J_n = \int |\ell_2 - \ell_1|^{n+1} d\ell_1 d\ell_2 dL \tag{B.4}$$

The integration on dL is realized over every possible lines L intersecting the external border $\partial\Omega$ while the integration on $d\ell_1$ and $d\ell_2$ are realized in the interval $[e_1, s_1]$. It gives

$$J_n = \int\limits_{L;L\cap\partial\Omega\neq\varnothing} dL \int_{e_1}^{s_1} d\ell_1 \int_{e_1}^{s_1} d\ell_2 |\ell_2 - \ell_1|^{n+1} \tag{B.5}$$

We split the integral depending on the relative sign of $\ell_2 - \ell_1$.

$$J_n = \int\limits_{L;L\cap\partial\Omega\neq\varnothing} dL \int_{e_1}^{s_1} d\ell_1 \left[\int_{e_1}^{\ell_1} d\ell_2 (\ell_1 - \ell_2)^{n+1} + \int_{\ell_1}^{s_1} d\ell_2 (\ell_2 - \ell_1)^{n+1} \right] \tag{B.6}$$

which gives

$$J_n = \frac{2}{(n+2)(n+3)} \int\limits_{L;L\cap\partial\Omega\neq\varnothing} dL (s_1 - e_1)^{n+3} \tag{B.7}$$

For $n = 0$, we get

$$A^2 = \frac{1}{3} \int\limits_{L;L\cap\partial\Omega\neq\varnothing} dL (s_1 - e_1)^{n+3} \tag{B.8}$$

We denote $C_{n+3}(L) = (s_1 - e_1)^{n+3}$ and evaluate $\langle C_3(L)\rangle_L$ the mean value of $C_3(L)$ among all possible lines L uniformly and isotropically distributed. The probability $p(L)dL$ to

measure a line L intersecting $\partial\Omega$ corresponds to the kinematic probability

$$p(L)dL = \frac{dL}{\int\limits_{L;L\cap\partial\Omega\neq\varnothing} dL} \tag{B.9}$$

The Poincaré theorem of integral geometry gives $\int\limits_{L;L\cap\partial\Omega\neq\varnothing} dL = P_{\text{ext}}$. The probability density being defined we have

$$\langle C_3(L)\rangle_L = \int\limits_{L;L\cap\partial\Omega\neq\varnothing} C_3(L)p(L)dL = \frac{\int\limits_{L;L\cap\partial\Omega\neq\varnothing} C_3(L)dL}{\int\limits_{L;L\cap\partial\Omega\neq\varnothing} dL} = \frac{\int\limits_{L;L\cap\partial\Omega\neq\varnothing} C_3(L)dL}{P_{\text{ext}}} = \frac{3A^2}{P_{\text{ext}}} \tag{B.10}$$

This is another elegant result from integral geometry which relates the third moment of the chord length distribution of a convex domain to its area and perimeter.

C

A new generalized invariant for ballistic motion

Illustration with a banana shape

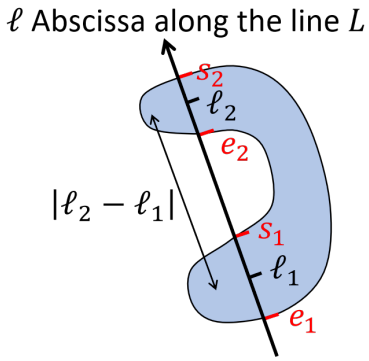

Figure C.1

We define a non-convex domain Ω of surface A. We denote $\partial\Omega$ its external border and P_{ext} the length of $\partial\Omega$. We consider a line L intersecting Ω. A point belonging to the line L is identified by its curvilinear abscissa ℓ along the line. For every line we enumerate the points where the line enters and exits the domain. With N being the number of exits for a given line L, we denote by $(e_i)_{i=1...N}$ the curvilinear abscissa of the entries and by $(s_i)_{i=1...N}$ the curvilinear abscissa of the exit. For a convex body, we have $N = 1$ for any possible lines intersecting $\partial\Omega$. However for a non-convex domain, there exits a family of lines such that $N > 1$ corresponding to multiple entries/exits. Such a line is illustrated in the Figure C.1. In this chapter we consider non-convex shape such that $N = 1, 2$.

We consider P_1 and P_2 two points belonging to a line L and being inside the domain. ℓ_1 and ℓ_2 refer their curvilinear abscissae. We denote r the distance between P_1 and P_2. For any given integer n, we consider the integral

$$J_n = \int\limits_{(P_1,P_2)\in\Omega\times\Omega} r^n d^2P_1 d^2P_2 \tag{C.1}$$

We remark again that for $n = 0$

$$J_0 = \int\limits_{(P_1,P_2)\in\Omega\times\Omega} d^2P_1 d^2P_2 = \int\limits_{P_1\in\Omega} d^2P_1 \times \int\limits_{P_2\in\Omega} d^2P_2 = A \times A = A^2. \tag{C.2}$$

The streamline of the demonstration is as follows. We calculate first J_n in term of internal and external chords and will equate the result with Eq. C.2 for the specific case $n = 0$.

We call f the characteristic function so that $f(P) = 1$ if $P \in \Omega$ and $f(P) = 0$ if $P \notin \Omega$. The $d^2P_1 d^2P_2$ can be expressed in the system of the line coordinates with a Jacobian similar to that above

$$d^2P_1 d^2P_2 = |\ell_2 - \ell_1| d\ell_1 d\ell_2 dL \tag{C.3}$$

with dL being the Poincaré kinematic measure. It gives

$$J_n = \int f(P_1) f(P_2) |\ell_2 - \ell_1|^{n+1} d\ell_1 d\ell_2 dL \tag{C.4}$$

The integration on dL is realized over every possible lines L intersecting the external border $\partial\Omega$ while the integrations on $d\ell_1$ and $d\ell_2$ are such that P_1 and P_2 remain in Ω. It gives

$$J_n = \int\limits_{L;L\cap\partial\Omega\neq\varnothing} dL \int d\ell_1 f(P_1) \int d\ell_2 f(P_2) |\ell_2 - \ell_1|^{n+1} \tag{C.5}$$

We separate the sets of lines L into two sets L_1 and L_2. A line L_1 enters once in the domain at a point e_1 and exits once at a point s_1. A line L_2 have two entries $(e_1; e_2)$ and two exits $(s_1; s_2)$ in the domain. A line L_2 is exemplified in the Figure C.1. It yields

$$J_n = \sum_{j=1}^{2} \int\limits_{L_j;L_j\cap\partial\Omega\neq\varnothing} dL_j \int d\ell_1 f(P_1) \int d\ell_2 f(P_2) |\ell_2 - \ell_1|^{n+1} \tag{C.6}$$

that we write into a compact form

$$J_n = \sum_{j=1}^{2} J_n^{(j)} \tag{C.7}$$

The computation of $J_n^{(1)}$ is strictly equivalent to that done in the previous chapter and gives

$$J_n^{(1)} = \frac{2}{(n+2)(n+3)} \int\limits_{L_1; L_1 \cap \partial\Omega \neq \varnothing} dL_1 (s_1 - e_1)^{n+3} \tag{C.8}$$

For a line L_2 the point P_1 can be either in or out of the domain Ω by sliding along the line L_2. It means that ℓ_1 must be integrated along two intervals $[e_1; s_1]$ and $[e_2; s_2]$ corresponding to P_1 being in Ω. It yields

$$J_n^{(2)} = \int\limits_{L_2; L_2 \cap \partial\Omega \neq \varnothing} dL_2 \left(\int_{e_1}^{s_1} d\ell_1 \int d\ell_2 f(P_2) |\ell_2 - \ell_1|^{n+1} + \int_{e_2}^{s_2} d\ell_1 \int d\ell_2 f(P_2) |\ell_2 - \ell_1|^{n+1} \right) \tag{C.9}$$

Then for every piece of integral we must pay attention to the sign of $\ell_2 - \ell_1$. The first piece of integration $\int_{e_1}^{s_1} d\ell_1 \ldots$ gives

$$\int_{e_1}^{s_1} d\ell_1 \int d\ell_2 f(P_2) |\ell_2 - \ell_1|^{n+1} = \int_{e_1}^{s_1} d\ell_1 \left(\int_{e_1}^{\ell_1} d\ell_2 \, (\ell_1 - \ell_2)^{n+1} + \int_{\ell_1}^{s_1} d\ell_2 \, (\ell_2 - \ell_1)^{n+1} + \int_{e_2}^{s_2} d\ell_2 \, (\ell_2 - \ell_1)^{n+1} \right) \tag{C.10}$$

The second piece of integration $\int_{e_2}^{s_2} d\ell_1 \ldots$ gives

$$\int_{e_2}^{s_2} d\ell_1 \int d\ell_2 f(P_2) |\ell_2 - \ell_1|^{n+1} = \int_{e_2}^{s_2} d\ell_1 \left(\int_{e_1}^{s_1} d\ell_2 \, (\ell_1 - \ell_2)^{n+1} + \int_{e_2}^{\ell_1} d\ell_2 \, (\ell_1 - \ell_2)^{n+1} + \int_{e_2}^{\ell_1} d\ell_2 \, (\ell_2 - \ell_1)^{n+1} \right) \tag{C.11}$$

All these integral can be performed explicitly which yields
The Figure C.2 gives a illustrative representation of each elements under the integral.

$J_n^{(2)} = \frac{2}{(n+2)(n+3)} \int\limits_{L_2; L_2 \cap \partial\Omega \neq \emptyset} dL_2$ 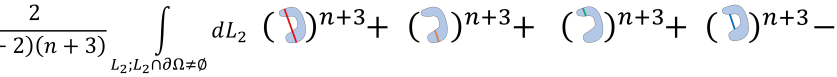

Figure C.2

For $n = 0$ we get the result

$$A^2 = \frac{1}{3} \int\limits_{L_1; L_1 \cap \partial\Omega \neq \varnothing} dL_1 (s_1 - e_1)^3 + \frac{1}{3} \int\limits_{L_2; L_2 \cap \partial\Omega \neq \varnothing} dL_2 \left(\left[(s_2 - e_1)^3 + (s_1 - e_1)^3 + (s_2 - e_2)^3 + (e_2 - s_1)^3 \right] - \left[(s_2 - s_1)^3 + (e_2 - e_1)^3 \right] \right) \tag{C.12}$$

For a line L_1 having only one entry in e_1 and one exit s_1, we denote

$$C_{n+3}(L_1) = (s_1 - e_1)^{n+3}. \tag{C.13}$$

For a line L_2 having two entries and two exits in Ω we define the quantity

$$C_{n+3}(L_2) = \left[(s_2 - e_1)^{n+3} + (s_1 - e_1)^{n+3} + (s_2 - e_2)^{n+3} + (e_2 - s_1)^{n+3} \right] - \left[(s_2 - s_1)^{n+3} + (e_2 - e_1)^{n+3} \right]. \tag{C.14}$$

We now want to evaluate $\langle C_3(L) \rangle_L$ the mean value of $C_3(L)$ among all possible lines L uniformly and isotropically distributed. The probability $p(L)dL$ to measure a line L intersecting Ω corresponds to the kinematic probability

$$p(L)dL = \frac{dL}{\int\limits_{L; L \cap \partial\Omega \neq \varnothing} dL} \tag{C.15}$$

Then, we have

$$\langle C_3(L) \rangle_L = \int\limits_{L; L \cap \partial\Omega \neq \varnothing} C_3(L) p(L) dL = \frac{\int\limits_{L; L \cap \partial\Omega \neq \varnothing} C_3(L) dL}{\int\limits_{L; L \cap \partial\Omega \neq \varnothing} dL} = \frac{3A^2}{\int\limits_{L; L \cap \partial\Omega \neq \varnothing} dL} \tag{C.16}$$

General case

We define a non-convex domain Ω of surface A. We denote $\partial\Omega$ its external border and P_{ext} the length of $\partial\Omega$. We consider a line L intersecting Ω. A point belonging to the line L is identified by its curvilinear abscissa ℓ along the line. For every line we enumerate the points where the line enters and exits the domain. While N being the number of exits, we denote by $(e_i)_{i=1\ldots N}$ the curvilinear abscissa of the entries and by $(s_i)_{i=1\ldots N}$ the curvilinear abscissa of the exit. Such a line is illustrated in the Figure C.3. In this chapter we consider non-convex shapes such that $N = 1, 2, 3, \ldots, \mathcal{N}$.

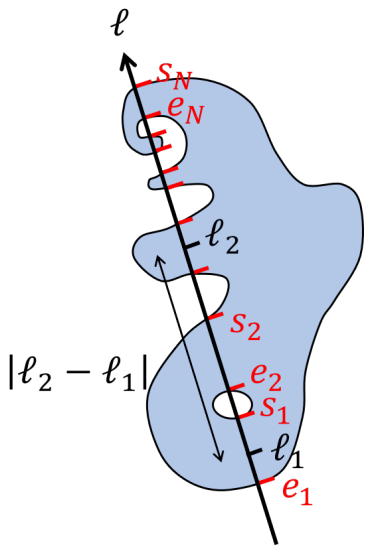

Figure C.3

We consider P_1 and P_2 two points belonging to a line L and being inside the domain. ℓ_1 and ℓ_2 refer their curvilinear abscissae. We denote r the distance between P_1 and P_2. For any given integer n, we consider the integral

$$J_n = \int\limits_{(P_1,P_2)\in\Omega\times\Omega} r^n d^2P_1 d^2P_2 \tag{C.17}$$

We remark again that for $n = 0$

$$J_0 = \int\limits_{(P_1,P_2)\in\Omega\times\Omega} d^2P_1 d^2P_2 = \int\limits_{P_1\in\Omega} d^2P_1 \times \int\limits_{P_2\in\Omega} d^2P_2 = A \times A = A^2. \tag{C.18}$$

The streamline of the demonstration is as follows the same as in previous chapter. We calculate first J_n in term of internal and external chords and will equate the result with Eq. C.18 for the specific case $n = 0$.

We call f the characteristic function so that $f(P) = 1$ if $P \in \Omega$ and $f(P) = 0$ if $P \notin \Omega$. The $d^2P_1 d^2P_2$ can be expressed in the system of the line coordinates with a Jacobian similar to that above

$$d^2P_1 d^2P_2 = |\ell_2 - \ell_1| d\ell_1 d\ell_2 dL \tag{C.19}$$

with dL being the Poincaré kinematic measure. It gives

$$J_n = \int f(P_1) f(P_2) |\ell_2 - \ell_1|^{n+1} d\ell_1 d\ell_2 dL \tag{C.20}$$

The integration on dL is realized over every possible lines L intersecting the external border $\partial\Omega$ while the integrations on $d\ell_1$ and $d\ell_2$ are such that P_1 and P_2 remain in Ω. It gives

$$J_n = \int\limits_{L; L\cap\partial\Omega\neq\varnothing} dL \int d\ell_1 f(P_1) \int d\ell_2 f(P_2) |\ell_2 - \ell_1|^{n+1} \tag{C.21}$$

The set of lines intersecting $\partial\Omega$ can be classified accordingly to the number of pairs entry-exit. We call L_N a line with $N \leq \mathcal{N}$ entries $(e_1, \ldots, e_N)$ and N exits $(s_1, \ldots, s_N)$. It gives

$$J_n = \sum_{N=1}^{\mathcal{N}} \int\limits_{L_N; L_N\cap\partial\Omega\neq\varnothing} dL_N \int d\ell_1 f(P_1) \int d\ell_2 f(P_2) |\ell_2 - \ell_1|^{n+1} \tag{C.22}$$

and we write the equation above into a compact form

$$J_n = \sum_{N=1}^{\mathcal{N}} J_n^{(N)} \tag{C.23}$$

with

$$J_n^{(N)} = \int\limits_{L_N; L_N\cap\partial\Omega\neq\varnothing} dL_N \int d\ell_1 f(P_1) \int d\ell_2 f(P_2) |\ell_2 - \ell_1|^{n+1} \tag{C.24}$$

While sliding along the line L_N, the point P_1 can be either in or out of the domain Ω. It means that ℓ_1 must be integrated along N intervals $[e_1; s_1]$, $[e_2; s_2], \ldots, [e_N; s_N]$, corresponding to P_1 being in Ω. It yields

$$J_n^{(N)} = \int\limits_{L_N; L_N\cap\partial\Omega\neq\varnothing} dL_N \sum_{k=1}^{N} \int_{e_k}^{s_k} d\ell_1 \int d\ell_2 f(P_2) |\ell_2 - \ell_1|^{n+1} \tag{C.25}$$

We treat the sum $\sum_{k=1}^{N}$ in three terms $k = 1$ and $k = N$ and $\sum_{k=2}^{N-1}$.

$$J_n^{(N)} = \int\limits_{L_N;L_N\cap\partial\Omega\neq\varnothing} dL_N \int_{e_1}^{s_1} d\ell_1 \int d\ell_2 f(P_2)|\ell_2-\ell_1|^{n+1} + \int\limits_{L_N;L_N\cap\partial\Omega\neq\varnothing} dL_N \sum_{k=2}^{N-1}\int_{e_k}^{s_k} d\ell_1 \int d\ell_2 f(P_2)|\ell_2-\ell_1|^{n+1} + \int\limits_{L_N;L_N\cap\partial\Omega\neq\varnothing} dL_N \int_{e_N}^{s_N} d\ell_1 \int d\ell_2 f(P_2)|\ell_2-\ell_1|^{n+1} \tag{C.26}$$

For every piece of integral we have to pay attention to the sign of $\ell_2-\ell_1$ and split the integration over ℓ_2.

$$J_n^{(N)} = \int\limits_{L_N;L_N\cap\partial\Omega\neq\varnothing} dL_N \int_{e_1}^{s_1} d\ell_1 \left[\int_{e_1}^{\ell_1} d\ell_2(\ell_1-\ell_2)^{n+1} + \int_{\ell_1}^{s_1} d\ell_2(\ell_2-\ell_1)^{n+1} + \sum_{k=2}^{N}\int_{e_k}^{s_k} d\ell_2(\ell_2-\ell_1)^{n+1}\right] + \int\limits_{L_N;L_N\cap\partial\Omega\neq\varnothing} dL_N \sum_{k=2}^{N-1}\int_{e_k}^{s_k} d\ell_1 \left[\sum_{i=1}^{k-1}\int_{e_i}^{s_i} d\ell_2(\ell_1-\ell_2)^{n+1} + \int_{e_k}^{\ell_1} d\ell_2(\ell_1-\ell_2)^{n+1} + \int_{\ell_1}^{s_k} d\ell_2(\ell_2-\ell_1)^{n+1} + \sum_{i=k+1}^{N}\int_{e_i}^{s_i} d\ell_2(\ell_2-\ell_1)^{n+1}\right] + \int\limits_{L_N;L_N\cap\partial\Omega\neq\varnothing} dL_N \int_{e_N}^{s_N} d\ell_1 \left[\sum_{i=1}^{N-1}\int_{e_i}^{s_i} d\ell_2(\ell_1-\ell_2)^{n+1} + \int_{e_N}^{\ell_1} d\ell_2(\ell_1-\ell_2)^{n+1} + \int_{\ell_1}^{s_N} d\ell_2(\ell_2-\ell_1)^{n+1}\right] \tag{C.27}$$

The integrals can be computed and expressed into a compact form

$$J_n^{(N)} = \frac{2}{(n+2)(n+3)} \int\limits_{L_N;L_N\cap\partial\Omega\neq\varnothing} dL_N \left(\sum_{k=1}^{N}\sum_{j=1}^{N}|s_k-e_i|^{n+3} - \sum_{k=1}^{N}\sum_{j=1}^{N}|s_k-s_i|^{n+3} - \sum_{k=1}^{N}\sum_{j=1}^{N}|e_k-e_i|^{n+3}\right) \tag{C.28}$$

with $j=1,\ldots,N$ and $k=1,\ldots,N$. For a line L_N having $N\leq\mathcal{N}$ entries and N exits in Ω we define the quantity

$$C_{n+3}(L_N) = \sum_{k=1}^{N}\sum_{j=1}^{N}|s_k-e_i|^{n+3} - \sum_{k=1}^{N}\sum_{j=1}^{N}|s_k-s_i|^{n+3} - \sum_{k=1}^{N}\sum_{j=1}^{N}|e_k-e_i|^{n+3} \tag{C.29}$$

that generalizes the definition in the two previous chapters. We now want to evaluate $\langle C_3(L)\rangle_L$ the mean value of $C_3(L)$ among all possible lines L uniformly and isotropically distributed. The probability $p(L)dL$ to measure a line L intersecting $\partial\Omega$ corresponds to the kinematic probability

$$p(L)dL = \frac{dL}{\int\limits_{L;L\cap\partial\Omega\neq\varnothing} dL} \tag{C.30}$$

Then, we have

$$\langle C_3(L)\rangle_L = \int\limits_{L;L\cap\partial\Omega\neq\varnothing} C_3(L)p(L)dL = \frac{\int\limits_{L;L\cap\partial\Omega\neq\varnothing} C_3(L)dL}{\int\limits_{L;L\cap\partial\Omega\neq\varnothing} dL} = \frac{3A^2}{\int\limits_{L;L\cap\partial\Omega\neq\varnothing} dL} \tag{C.31}$$

that we write under the form

$$\langle \sum_{k,j} |s_k - e_i|^3 - \sum_{k,j} |s_k - s_i|^3 - \sum_{k,j} |e_k - e_i|^3 \rangle_L = \frac{3A^2}{\int\limits_{L;L\cap\partial\Omega\neq\varnothing} dL} \tag{C.32}$$

In order to simplify the previous equation, let us calculate the generalized first moment $\langle C_1(L)\rangle_L$

$$\langle C_1(L)\rangle_L = \langle \sum_{k,j} |s_k - e_i| - \sum_{k,j} |s_k - s_i| - \sum_{k,j} |e_k - e_i| \rangle_L \tag{C.33}$$

If we take the oriented distances, this equation simplifies to

$$\langle C_1(L)\rangle_L = \langle \sum_{k,j} |s_k - e_k| \rangle_L \tag{C.34}$$

This corresponds to the length of the crossing portion of line. The measure of this length is the region's area multiplied by π, then

$$\langle \sum_{k,j} |s_k - e_i| - \sum_{k,j} |s_k - s_i| - \sum_{k,j} |e_k - e_i| \rangle_L = \frac{\pi A}{\int\limits_{L;L\cap\partial\Omega\neq\varnothing} dL} \tag{C.35}$$

Thus, by combining eqs. C.32 and C.35 we obtain

$$\frac{\langle \sum_{k,j} |s_k - e_i|^3 - \sum_{k,j} |s_k - s_i|^3 - \sum_{k,j} |e_k - e_i|^3 \rangle_L}{\langle \sum_{k,j} |s_k - e_i| - \sum_{k,j} |s_k - s_i| - \sum_{k,j} |e_k - e_i| \rangle_L} = \frac{3A}{\pi} \tag{C.36}$$

D

Transient regime analysis of a DTR

Let us consider the Fourier transform of the wave equation 2.1 where we add a damping term $-\zeta(k)\frac{\partial\phi}{\partial t}(r,t)$

$$\frac{\partial^2\widetilde{\phi}}{\partial t^2}(k,t)+\zeta(k)\frac{\partial\widetilde{\phi}}{\partial t}(k,t)+\omega_0^2(k)\widetilde{\phi}(k,t)=0, \tag{D.1}$$

We consider the regime of high dissipation, so that we assume $\zeta(k)>2\omega_0(k)$. is thus the equation of a damped harmonic oscillator in the overdamped regime, whose solutions are given by

$$\widetilde{\phi}(k,t)=Ae^{-\frac{\zeta(k)}{2}\left(1+\sqrt{1-\frac{\omega_0^2(k)}{\zeta^2(k)}}\right)(t-t_0)}+Be^{-\frac{\zeta(k)}{2}\left(1-\sqrt{1-\frac{\omega_0^2(k)}{\zeta^2(k)}}\right)(t-t_0)} \tag{D.2}$$

with A and B two constants. Given the initial conditions of continuity of the field and its time derivative, we obtain

$$\begin{aligned}\widetilde{\phi}(k,t)=&\frac{\left(\sqrt{1-\frac{\omega_0^2(k)}{\zeta^2(k)}}-1\right)\widetilde{\phi}_i(k,t_0)-\frac{2}{\zeta(k)}\frac{\partial\widetilde{\phi}_i}{\partial t}(k,t_0)}{2\sqrt{1-\frac{\omega_0^2(k)}{\zeta^2(k)}}}e^{-\frac{\zeta(k)}{2}\left(1+\sqrt{1-\frac{\omega_0^2(k)}{\zeta^2(k)}}\right)(t-t_0)}+\\&\frac{\left(\sqrt{1-\frac{\omega_0^2(k)}{\zeta^2(k)}}+1\right)\widetilde{\phi}_i(k,t_0)+\frac{2}{\zeta(k)}\frac{\partial\widetilde{\phi}_i}{\partial t}(k,t_0)}{2\sqrt{1-\frac{\omega_0^2(k)}{\zeta^2(k)}}}e^{-\frac{\zeta(k)}{2}\left(1-\sqrt{1-\frac{\omega_0^2(k)}{\zeta^2(k)}}\right)(t-t_0)}\end{aligned} \tag{D.3}$$

Developing at first order in $\frac{\omega_0(k)}{\zeta(k)} \to 0$ in front of and (at order 2) inside the exponential terms

$$\widetilde{\phi}(k,t) = -\frac{1}{\zeta(k)}\frac{\partial\widetilde{\phi}_i}{\partial t}(k,t_0)\, e^{-\frac{\zeta(k)}{2}\left(2-\frac{1}{2}\frac{\omega_0^2(k)}{\zeta^2(k)}+o\left(\frac{\omega_0^2(k)}{\zeta^2(k)}\right)\right)(t-t_0)} + \left(\widetilde{\phi}_i(k,t_0) + \frac{1}{\zeta(k)}\frac{\partial\widetilde{\phi}_i}{\partial t}(k,t_0)\right) e^{-\frac{\zeta(k)}{2}\left(\frac{1}{2}\frac{\omega_0^2(k)}{\zeta^2(k)}+o\left(\frac{\omega_0^2(k)}{\zeta^2(k)}\right)\right)(t-t_0)} \quad \text{(D.4)}$$

where we used the fact that $\frac{1}{\zeta(k)}\frac{\partial\widetilde{\phi}_i}{\partial t}(k,t_0)$ is of order one in $\omega_0(k)/\zeta(k)$. Taking the zeroth order inside the exponential yields to the expressions presented in 2.4.

Equation D.4 also reveals that the wave amplitude decreases like $e^{-\frac{\omega_0^2(k)}{4\zeta(k)}(t-t_0)}$ in the long run.

E

The lubrication approximation

We consider that the vapor flow located under the drop can be described by the incompressible and steady Stokes equation.

$$\eta \Delta \vec{v} = \nabla P \tag{E.1}$$

This flow must also satisfy the continuity equation:

$$\nabla \cdot \vec{v} = 0 \tag{E.2}$$

Due to the aspect ratio between the drop radius and the vapor layer thickness $R/\delta > 10^2$, we can use the lubrication approximation [170], which can be written in cylindrical coordinates

$$\frac{\partial^2 v_r}{\partial z^2} = \frac{1}{\eta}\frac{\partial P}{\partial r} \tag{E.3}$$

$$\frac{\partial^2 v_\theta}{\partial z^2} = \frac{1}{\eta}\frac{\partial P}{r\partial \theta} \tag{E.4}$$

We can integrate twice these equations with respect to z between $z = 0$ and $z = \delta$, applying the non-slip conditions for v_θ and v_r. We obtain

$$v_r = \frac{z(z-\delta)}{2\eta}\frac{\partial P}{\partial r} \tag{E.5}$$

$$v_\theta = \frac{z(z-\delta)}{2r\eta}\frac{\partial P}{\partial \theta} \tag{E.6}$$

These equations can be replaced in E.2. to eliminate the velocity field. After integrating between $z = 0$ and $z = \delta$ and considering a constant vapor thickness δ one finds

$$\frac{1}{r}\frac{\partial}{\partial r}\left(r\frac{\partial P}{\partial r}\right) + \frac{1}{r}\frac{\partial}{\partial \theta}\frac{1}{r}\frac{\partial P}{\partial \theta} = \frac{12\eta v_n}{\delta^3} \tag{E.7}$$

This is the Poisson equation written in cylindrical coordinates with a source term $f = 12\eta v_n/\delta^3$.

The torsional shear stress τ_θ can be approximated as $\tau_\theta \approx \eta\frac{\langle v_\theta \rangle}{\delta}$, which can be written in terms of the pressure gradient:

$$\tau_\theta \approx \left.\frac{\partial v_\theta}{\partial z}\right|_{z=\delta} = \frac{\delta}{2r}\frac{\partial P}{\partial \theta} \tag{E.8}$$

Bibliography

[1] A. L. B. Cauchy, *Mémoire sur la rectification des courbes et la quadrature des surfaces courbes*. 1832. Google-Books-ID: DUIczPvOt24C.

[2] A. Mazzolo, B. Roesslinger, and W. Gille, "Properties of chord length distributions of nonconvex bodies," *Journal of Mathematical Physics*, vol. 44, pp. 6195–6208, Dec. 2003. Publisher: American Institute of Physics.

[3] A. Mazzolo, C. de Mulatier, and A. Zoia, "Cauchy's formulas for random walks in bounded domains," *Journal of Mathematical Physics*, vol. 55, p. 083308, Aug. 2014. Publisher: American Institute of Physics.

[4] S. Hidalgo-Caballero, A. Cassinelli, M. Labousse, and E. Fort, "Mean arc theorem for exploring domains with randomly distributed arbitrary closed trajectories," *The European Physical Journal Plus*, vol. 137, no. 4, pp. 1–7, 2022.

[5] V. Bacot, M. Labousse, A. Eddi, M. Fink, and E. Fort, "Time reversal and holography with spacetime transformations," vol. 12, no. 10, pp. 972–977. Number: 10 Publisher: Nature Publishing Group.

[6] V. Bacot, G. Durey, A. Eddi, M. Fink, and E. Fort, "Phase-conjugate mirror for water waves driven by the faraday instability," *Proceedings of the National Academy of Sciences*, vol. 116, no. 18, pp. 8809–8814, 2019.

[7] J. G. Leidenfrost, *De aquae communis nonnullis qualitatibus tractatus*. Ovenius. Google-Books-ID: r3JgAAAAcAAJ.

[8] D. Quéré, "Leidenfrost dynamics," vol. 45, no. 1, pp. 197–215.

[9] G. Lagubeau, M. Le Merrer, C. Clanet, and D. Quéré, "Leidenfrost on a ratchet," vol. 7, no. 5, pp. 395–398.

[10] G. Dupeux, M. Le Merrer, G. Lagubeau, C. Clanet, S. Hardt, and D. Quéré, "Viscous mechanism for leidenfrost propulsion on a ratchet," vol. 96, no. 5, p. 58001.

[11] P. Dirac, "Approximate rate of neutron multiplication for a solid of arbitrary shape and uniform density," *Declassified British Report MS-D-5, Part I*, 1943.

[12] W. J. M. de Kruijf and J. L. Kloosterman, "On the average chord length in reactor physics," *Annals of Nuclear Energy*, vol. 30, pp. 549–553, Mar. 2003.

[13] S. Blanco and R. Fournier, "An invariance property of diffusive random walks," *EPL (Europhysics Letters)*, vol. 61, no. 2, p. 168, 2003.

[14] R. Jeanson, C. Rivault, J.-L. Deneubourg, S. Blanco, R. Fournier, C. Jost, and G. Theraulaz, "Self-organized aggregation in cockroaches," *Animal Behaviour*, vol. 69, pp. 169–180, Jan. 2005.

[15] R. Pierrat, P. Ambichl, S. Gigan, A. Haber, R. Carminati, and S. Rotter, "Invariance property of wave scattering through disordered media," *Proceedings of the National Academy of Sciences*, vol. 111, pp. 17765–17770, Dec. 2014. Publisher: Proceedings of the National Academy of Sciences.

[16] L. A. Santaló, *Integral geometry and geometric probability*. Cambridge university press, 2004.

[17] A. Kalousova, "The Origins of the Geometric Probability in England," *GEOMETRIC PROBABILITY*, p. 6.

[18] C. Z. Mooney, *Monte carlo simulation*. No. 116, Sage, 1997.

[19] E. Seneta, K. H. Parshall, and F. Jongmans, "Nineteenth-Century Developments in Geometric Probability: J. J. Sylvester, M. W. Crofton, J.-É. Barbier, and J. Bertrand," *Archive for History of Exact Sciences*, vol. 55, no. 6, pp. 501–524, 2001. Publisher: Springer.

[20] B. J. Arnow, "On laplace's extension of the buffon needle problem," *The College Mathematics Journal*, vol. 25, no. 1, pp. 40–43, 1994.

[21] R. Sanchez, "On the use of the average chord length," *Annals of Nuclear Energy*, vol. 31, pp. 2211–2216, Dec. 2004.

[22] D. Guéron and A. Mazzolo, "Properties of chord length distributions across ordered and disordered packing of hard disks," *Physical Review. E, Statistical, Nonlinear, and Soft Matter Physics*, vol. 68, p. 066117, Dec. 2003.

[23] A. Mazzolo, "On the generalization of the average chord length," *Annals of Nuclear Energy*, vol. 35, pp. 503–506, Mar. 2008.

[24] P. Reuss, "Cauchy's theorem and generalization," *EPJ Nuclear Sciences & Technologies*, vol. 4, p. 50, 2018. Publisher: EDP Sciences.

[25] T. B. Borak, "A method for computing random chord length distributions in geometrical objects," *Radiation research*, vol. 137, no. 3, pp. 346–351, 1994.

[26] G. J. Hine and G. L. Brownell, *Radiation dosimetry*. Elsevier, 2013.

[27] P. Tissier, "Bertrand's paradox," *The Mathematical Gazette*, vol. 68, no. 443, pp. 15–19, 1984.

[28] H. Solomon, *Geometric probability*. SIAM, 1978.

[29] A. Soranzo and A. Volčič, "On the bertrand paradox," *Rendiconti del Circolo Matematico di Palermo*, vol. 47, no. 3, pp. 503–509, 1998.

[30] G. Frangipane, G. Vizsnyiczai, C. Maggi, R. Savo, A. Sciortino, S. Gigan, and R. Di Leonardo, "Invariance properties of bacterial random walks in complex structures," *Nature communications*, vol. 10, no. 1, pp. 1–6, 2019.

[31] R. Savo, R. Pierrat, U. Najar, R. Carminati, S. Rotter, and S. Gigan, "Observation of mean path length invariance in light-scattering media," *Science*, vol. 358, pp. 765–768, Nov. 2017. Publisher: American Association for the Advancement of Science.

[32] C. Bechinger, R. Di Leonardo, H. Löwen, C. Reichhardt, G. Volpe, and G. Volpe, "Active particles in complex and crowded environments," *Reviews of Modern Physics*, vol. 88, no. 4, p. 045006, 2016.

[33] H.-T. Zhang, Z. Chen, L. Yan, and W. Yu, "Applications of collective circular motion control to multirobot systems," *IEEE Transactions on Control Systems Technology*, vol. 21, no. 4, pp. 1416–1422, 2012.

[34] H. Hadwiger, "Überdeckung ebener bereiche durch kreise und quadrate," *Commentarii Mathematici Helvetici*, vol. 13, no. 1, pp. 195–200, 1940.

[35] A. Mazzolo, "Invariance properties of random curves: an approach based on integral geometry," *arXiv preprint arXiv:2011.06343*, 2020.

[36] P. Moran, "Geometric probability theory," *Encyclopedia of Statistical Sciences*, 2004.

[37] T. M. Buzug, "Computed tomography," in *Springer handbook of medical technology*, pp. 311–342, Springer, 2011.

[38] A. G. Ramm and A. I. Katsevich, *The Radon transform and local tomography*. CRC press, 2020.

[39] A. Mazzolo, B. Roesslinger, and C. M. Diop, "On the properties of the chord length distribution, from integral geometry to reactor physics," *Annals of Nuclear Energy*, vol. 30, pp. 1391–1400, Sept. 2003.

[40] M. Rubenstein, C. Ahler, and R. Nagpal, "Kilobot: A low cost scalable robot system for collective behaviors," in *2012 IEEE international conference on robotics and automation*, pp. 3293–3298, IEEE, 2012.

[41] R. Sánchez and P. Díaz-Leyva, "Self-assembly and speed distributions of active granular particles," *Physica A: Statistical Mechanics and its Applications*, vol. 499, pp. 11–19, 2018.

[42] J.-F. Boudet, J. Lintuvuori, C. Lacouture, T. Barois, A. Deblais, K. Xie, S. Cassagnere, B. Tregon, D. Brückner, J.-C. Baret, *et al.*, "From collections of independent, mindless robots to flexible, mobile, and directional superstructures," *Science Robotics*, vol. 6, no. 56, p. eabd0272, 2021.

[43] P. Baconnier, D. Shohat, and O. Dauchot, "Tension-controlled switch between collective actuations in active solids," *arXiv preprint arXiv:2208.09258*, 2022.

[44] M. Ioannou and T. Bratitsis, "Teaching the notion of speed in kindergarten using the sphero sprk robot," in *2017 IEEE 17th International Conference on Advanced Learning Technologies (ICALT)*, pp. 311–312, IEEE, 2017.

[45] S. Kurkovsky, "Interdisciplinary connections in a mobile computing and robotics course," in *Proceedings of the 2014 conference on Innovation & technology in computer science education*, pp. 309–314, 2014.

[46] W. Gille, "Chord length distributions and small-angle scattering," *The European Physical Journal B - Condensed Matter and Complex Systems*, vol. 17, pp. 371–383, Oct. 2000.

[47] G. A. Brosamler, "An almost everywhere central limit theorem," in *Mathematical Proceedings of the Cambridge Philosophical Society*, vol. 104, pp. 561–574, Cambridge University Press, 1988.

[48] U. N. G. Assembly, *Universal declaration of human rights*, vol. 3381. Department of State, United States of America, 1949.

[49] R. F. Steidel Jr, "An introduction to mechanical vibrations. johnwiley& sons," 1989.

[50] D. S. Bernstein and S. P. Bhat, "Energy equipartition and the emergence of damping in lossless systems," in *Proceedings of the 41st IEEE Conference on Decision and Control, 2002.*, vol. 3, pp. 2913–2918, IEEE, 2002.

[51] W. C. Elmore, W. C. Elmore, and M. A. Heald, *Physics of waves*. Courier Corporation, 1985.

[52] H. B. Callen and T. A. Welton, "Irreversibility and generalized noise," *Physical Review*, vol. 83, no. 1, p. 34, 1951.

[53] R. Landauer, "Irreversibility and heat generation in the computing process," *IBM journal of research and development*, vol. 5, no. 3, pp. 183–191, 1961.

[54] R. Kubo, "The fluctuation-dissipation theorem," *Reports on progress in physics*, vol. 29, no. 1, p. 255, 1966.

[55] J. Loschmidt and J. Sitzungsber, "der kais. akad. d," *W. Math. Naturw. II*, vol. 73, p. 128, 1876.

[56] P. L. Marston, "Maxwell–thomson–loschmidt reversal," *Nature Physics*, vol. 13, no. 1, pp. 2–2, 2017.

[57] E. H. Kennard *et al.*, *Kinetic theory of gases*, vol. 483. McGraw-hill New York, 1938.

[58] T.-Y. Wu, "Boltzmann'sh theorem and the loschmidt and the zermelo paradoxes," *International Journal of Theoretical Physics*, vol. 14, no. 5, pp. 289–294, 1975.

[59] J. A. Roberts and G. Quispel, "Chaos and time-reversal symmetry. order and chaos in reversible dynamical systems," *Physics Reports*, vol. 216, no. 2-3, pp. 63–177, 1992.

[60] K. Breus, "Jean le rond d'alembert on the 250th anniversary of his birth," 1968.

[61] M. Fink, "Time-reversal waves and super resolution," in *Journal of Physics: Conference Series*, vol. 124, p. 012004, IOP Publishing, 2008.

[62] M. Fink, "Time-reversal mirrors," *Journal of Physics D: Applied Physics*, vol. 26, no. 9, p. 1333, 1993.

[63] M. Fink and E. Fort, "From the time-reversal mirror to the instantaneous time mirror," *The European Physical Journal Special Topics*, vol. 226, no. 7, pp. 1477–1486, 2017.

[64] M. Fink, "Time reversal of ultrasonic fields. i. basic principles," *IEEE transactions on ultrasonics, ferroelectrics, and frequency control*, vol. 39, no. 5, pp. 555–566, 1992.

[65] G. Lerosey, J. De Rosny, A. Tourin, A. Derode, G. Montaldo, and M. Fink, "Time reversal of electromagnetic waves," *Physical review letters*, vol. 92, no. 19, p. 193904, 2004.

[66] N. Bojarski, "A survey of the near-field far-field inverse scattering inverse source integral equation," *IEEE Transactions on Antennas and Propagation*, vol. 30, no. 5, pp. 975–979, 1982.

[67] D. Gabor, "A new microscopic principle," *nature*, vol. 161, pp. 777–778, 1948.

[68] D. Gabor, "Nobel lecture, december 11, 1971," *Nobel Lectures, Physics 1971–1980*, p. 6ff, 1992.

[69] F. T. S. Committee *et al.*, "Federal standard 1037c: Glossary of telecommunications terms (fed-std-1037c)," *National Communications System Technology Program Office, Arlington, Virginia*, 1996.

[70] J. Hecht, "A short history of laser development," *Applied optics*, vol. 49, no. 25, pp. F99–F122, 2010.

[71] Y. N. Denisyuk, "Photographic reconstruction of the optical properties of an object in its own scattered radiation field," in *Soviet Physics Doklady*, vol. 7, p. 543, 1962.

[72] E. N. Leith and J. Upatnieks, "Reconstructed wavefronts and communication theory," *JOSA*, vol. 52, no. 10, pp. 1123–1130, 1962.

[73] E. Ingelstam, "Dennis gabor-winner of the 1971 physics nobel prize," *Europhysics News*, vol. 3, no. 1, pp. 3–3, 1972.

[74] P. Günter, "Holography, coherent light amplification and optical phase conjugation with photorefractive materials," *Physics Reports*, vol. 93, no. 4, pp. 199–299, 1982.

[75] A. P. Brysev, L. Krutyanskii, and V. L. Preobrazhenskii, "Wave phase conjugation of ultrasonic beams," *Physics-Uspekhi*, vol. 41, no. 8, p. 793, 1998.

[76] A. Yariv, "Phase conjugate optics and real-time holography," *IEEE Journal of Quantum Electronics*, vol. 14, no. 9, pp. 650–660, 1978.

[77] G. S. He, "Optical phase conjugation: principles, techniques, and applications," *Progress in Quantum Electronics*, vol. 26, no. 3, pp. 131–191, 2002.

[78] N. Chakroun, M. A. Fink, and F. Wu, "Time reversal processing in ultrasonic nondestructive testing," *IEEE transactions on ultrasonics, ferroelectrics, and frequency control*, vol. 42, no. 6, pp. 1087–1098, 1995.

[79] M. Fink, D. Cassereau, A. Derode, C. Prada, P. Roux, M. Tanter, J.-L. Thomas, and F. Wu, "Time-reversed acoustics," *Reports on progress in Physics*, vol. 63, no. 12, p. 1933, 2000.

[80] F. Wu, J.-L. Thomas, and M. Fink, "Time reversal of ultrasonic fields. il. experimental results," *IEEE transactions on ultrasonics, ferroelectrics, and frequency control*, vol. 39, no. 5, pp. 567–578, 1992.

[81] J.-L. Thomas, F. Wu, and M. Fink, "Time reversal focusing applied to lithotripsy," *Ultrasonic imaging*, vol. 18, no. 2, pp. 106–121, 1996.

[82] M. Fink, G. Montaldo, and M. Tanter, "Time-reversal acoustics in biomedical engineering," *Annual review of biomedical engineering*, vol. 5, no. 1, pp. 465–497, 2003.

[83] M. Fink and C. Prada, "Acoustic time-reversal mirrors," *Inverse problems*, vol. 17, no. 1, p. R1, 2001.

[84] B. Y. Zel'Dovich, N. F. Pilipetsky, and V. V. Shkunov, *Principles of phase conjugation*, vol. 42. Springer, 2013.

[85] G. B. Arfken and H. J. Weber, "Mathematical methods for physicists," 1999.

[86] A. L. Cauchy, *Mémoire sur l'emploi du calcul des limites dans l'intégration des équations aux dérivées partielles*. 1842.

[87] J. L. Davis, "Mathematics of wave propagation," in *Mathematics of Wave Propagation*, Princeton University Press, 2022.

[88] B. Burgel, "Dispersion, reflection, and eigenfrequencies on the wave machine," *American Journal of Physics*, vol. 35, no. 10, pp. 913–915, 1967.

[89] Y. Escobar-Ortega, S. Hidalgo-Caballero, J. Marston, and F. Pacheco-Vázquez, "The viscoelastic-like response of a repulsive granular medium during projectile impact and penetration," *Journal of Non-Newtonian Fluid Mechanics*, vol. 280, p. 104295, 2020.

[90] H. Grubmüller, H. Heller, A. Windemuth, and K. Schulten, "Generalized verlet algorithm for efficient molecular dynamics simulations with long-range interactions," *Molecular Simulation*, vol. 6, no. 1-3, pp. 121–142, 1991.

[91] E. Hecht, "Optics 3rd ed., eddison wesley longman," *Inc., NY*, 1998.

[92] J. W. Thomas, *Numerical partial differential equations: finite difference methods*, vol. 22. Springer Science & Business Media, 2013.

[93] J. Wilson, F. Santosa, M. Min, and T. Low, "Temporal control of graphene plasmons," *Physical Review B*, vol. 98, no. 8, p. 081411, 2018.

[94] L. Li, M. Wang, J. Wang, and X. Zhao, "The control of ultrasonic transmission by the metamaterials structure of electrorheological fluid and metal foam," *Smart Materials and Structures*, vol. 26, no. 11, p. 115006, 2017.

[95] A. P. Mosk, A. Lagendijk, G. Lerosey, and M. Fink, "Controlling waves in space and time for imaging and focusing in complex media," *Nature photonics*, vol. 6, no. 5, pp. 283–292, 2012.

[96] M. E. Yavuz and F. L. Teixeira, "Ultrawideband microwave sensing and imaging using time-reversal techniques: A review," *Remote Sensing*, vol. 1, no. 3, pp. 466–495, 2009.

[97] V. Pacheco-Peña and N. Engheta, "Temporal metamaterials with gain and loss," *arXiv preprint arXiv:2108.01007*, 2021.

[98] S. Völker, "Hole-burning spectroscopy," *Annual Review of Physical Chemistry*, vol. 40, no. 1, pp. 499–530, 1989.

[99] B. Gottfried, C. Lee, and K. Bell, "The leidenfrost phenomenon: film boiling of liquid droplets on a flat plate," *International Journal of heat and mass transfer*, vol. 9, no. 11, pp. 1167–1188, 1966.

[100] C. J. Hoogendoorn and R. Den Hond, "Leidenfrost temperature and heat-transfer coefficients for water sprays impinging on a hot surface," in *International Heat Transfer Conference Digital Library*, Begel House Inc., 1974.

[101] H. Linke, B. Alemán, L. Melling, M. Taormina, M. Francis, C. Dow-Hygelund, V. Narayanan, R. Taylor, and A. Stout, "Self-propelled leidenfrost droplets," *Physical review letters*, vol. 96, no. 15, p. 154502, 2006.

[102] G. Dupeux, M. Le Merrer, C. Clanet, and D. Quéré, "Trapping leidenfrost drops with crenelations," vol. 107, no. 11, p. 114503.

[103] S. Perrard, Y. Couder, E. Fort, and L. Limat, "Leidenfrost levitated liquid tori," vol. 100, no. 5, p. 54006.

[104] D. Quéré, "Leidenfrost dynamics," *Annual Review of Fluid Mechanics*, vol. 45, no. 1, pp. 197–215, 2013.

[105] D. Saranadhi, D. Chen, J. A. Kleingartner, S. Srinivasan, R. E. Cohen, and G. H. McKinley, "Sustained drag reduction in a turbulent flow using a low-temperature leidenfrost surface," *Science advances*, vol. 2, no. 10, p. e1600686, 2016.

[106] S. Hidalgo-Caballero, Y. Escobar-Ortega, and F. Pacheco-Vázquez, "Leidenfrost phenomenon on conical surfaces," vol. 1, no. 5, p. 051902.

[107] A. Bouillant, B. Lafoux, C. Clanet, and D. Quéré, "Thermophobic leidenfrost," *Soft Matter*, vol. 17, no. 39, pp. 8805–8809, 2021.

[108] P. Agrawal, G. G. Wells, R. Ledesma-Aguilar, G. McHale, and K. Sefiane, "Beyond leidenfrost levitation: A thin-film boiling engine for controlled power generation," *Applied Energy*, vol. 287, p. 116556, 2021.

[109] A. Gauthier, C. Diddens, R. Proville, D. Lohse, and D. van der Meer, "Self-propulsion of inverse leidenfrost drops on a cryogenic bath," *Proceedings of the National Academy of Sciences*, vol. 116, no. 4, pp. 1174–1179, 2019.

[110] A.-L. Biance, C. Clanet, and D. Quéré, "Leidenfrost drops," vol. 15, no. 6, p. 7.

[111] G. Paul, P. K. Das, and I. Manna, "Droplet oscillation and pattern formation during leidenfrost phenomenon," *Experimental Thermal and Fluid Science*, vol. 60, pp. 346–353, 2015.

[112] X. Ma, J.-J. Liétor-Santos, and J. C. Burton, "Star-shaped oscillations of leidenfrost drops," vol. 2, no. 3, p. 031602.

[113] T. A. Caswell, "Dynamics of the vapor layer below a leidenfrost drop," *Physical Review E*, vol. 90, no. 1, p. 013014, 2014.

[114] X. Ma and J. C. Burton, "Self-organized oscillations of leidenfrost drops," vol. 846, pp. 263–291.

[115] J. Li, Y. Hou, Y. Liu, C. Hao, M. Li, M. K. Chaudhury, S. Yao, and Z. Wang, "Directional transport of high-temperature janus droplets mediated by structural topography," *Nature Physics*, vol. 12, no. 6, pp. 606–612, 2016.

[116] B. Sobac, A. Rednikov, S. Dorbolo, and P. Colinet, "Self-propelled leidenfrost drops on a thermal gradient: A theoretical study," *Physics of Fluids*, vol. 29, no. 8, p. 082101, 2017.

[117] F. Curzon, "The leidenfrost phenomenon," *American Journal of Physics*, vol. 46, no. 8, pp. 825–828, 1978.

[118] X. Ma, J.-J. Liétor-Santos, and J. C. Burton, "The many faces of a leidenfrost drop," *Physics of Fluids*, vol. 27, no. 9, p. 091109, 2015.

[119] L. Maquet, B. Sobac, B. Darbois-Texier, A. Duchesne, M. Brandenbourger, A. Rednikov, P. Colinet, and S. Dorbolo, "Leidenfrost drops on a heated liquid pool," *Physical Review Fluids*, vol. 1, no. 5, p. 053902, 2016.

[120] G. Dupeux, M. Le Merrer, G. Lagubeau, C. Clanet, S. Hardt, and D. Quéré, "Viscous mechanism for leidenfrost propulsion on a ratchet," *EPL (Europhysics Letters)*, vol. 96, no. 5, p. 58001, 2011.

[121] M. Gradeck, N. Seiler, P. Ruyer, and D. Maillet, "Heat transfer for leidenfrost drops bouncing onto a hot surface," *Experimental Thermal and Fluid Science*, vol. 47, pp. 14–25, 2013.

[122] A. Shahriari, J. Wurz, and V. Bahadur, "Heat transfer enhancement accompanying leidenfrost state suppression at ultrahigh temperatures," *Langmuir*, vol. 30, no. 40, pp. 12074–12081, 2014.

[123] I. U. Vakarelski, J. O. Marston, D. Y. Chan, and S. T. Thoroddsen, "Drag reduction by leidenfrost vapor layers," *Physical Review Letters*, vol. 106, no. 21, p. 214501, 2011.

[124] L. E. Dodd, D. Wood, N. R. Geraldi, G. G. Wells, G. McHale, B. B. Xu, S. Stuart-Cole, J. Martin, and M. I. Newton, "Low friction droplet transportation on a substrate with a selective leidenfrost effect," *ACS Applied Materials & Interfaces*, vol. 8, no. 34, pp. 22658–22663, 2016.

[125] G. G. Wells, R. Ledesma-Aguilar, G. McHale, and K. Sefiane, "A sublimation heat engine," *Nature communications*, vol. 6, no. 1, pp. 1–7, 2015.

[126] S. R. Waitukaitis, A. Zuiderwijk, A. Souslov, C. Coulais, and M. Van Hecke, "Coupling the leidenfrost effect and elastic deformations to power sustained bouncing," *Nature Physics*, vol. 13, no. 11, pp. 1095–1099, 2017.

[127] J. D. Bernardin and I. Mudawar, "A cavity activation and bubble growth model of the leidenfrost point," *J. Heat Transfer*, vol. 124, no. 5, pp. 864–874, 2002.

[128] J. Bernardin and I. Mudawar, "The leidenfrost point: experimental study and assessment of existing models," 1999.

[129] H. Kim, B. Truong, J. Buongiorno, and L.-W. Hu, "On the effect of surface roughness height, wettability, and nanoporosity on leidenfrost phenomena," *Applied Physics Letters*, vol. 98, no. 8, p. 083121, 2011.

[130] M. A. van Limbeek, O. Ramírez-Soto, A. Prosperetti, and D. Lohse, "How ambient conditions affect the leidenfrost temperature," *Soft matter*, vol. 17, no. 11, pp. 3207–3215, 2021.

[131] D. Orejon, K. Sefiane, and Y. Takata, "Effect of ambient pressure on leidenfrost temperature," *Physical Review E*, vol. 90, no. 5, p. 053012, 2014.

[132] L. Maquet, M. Brandenbourger, B. Sobac, A.-L. Biance, P. Colinet, and S. Dorbolo, "Leidenfrost drops: Effect of gravity," *EPL (Europhysics Letters)*, vol. 110, no. 2, p. 24001, 2015.

[133] M. Jiang, Y. Wang, F. Liu, H. Du, Y. Li, H. Zhang, S. To, S. Wang, C. Pan, J. Yu, *et al.*, "Inhibiting the leidenfrost effect above 1,000° c for sustained thermal cooling," *Nature*, vol. 601, no. 7894, pp. 568–572, 2022.

[134] G. Graeber, K. Regulagadda, P. Hodel, C. Küttel, D. Landolf, T. M. Schutzius, and D. Poulikakos, "Leidenfrost droplet trampolining," *Nature communications*, vol. 12, no. 1, pp. 1–7, 2021.

[135] G. I. Taylor, "The instability of liquid surfaces when accelerated in a direction perpendicular to their planes. i," vol. 201, no. 1065, pp. 192–196. Publisher: Royal Society.

[136] J. H. Snoeijer, P. Brunet, and J. Eggers, "Maximum size of drops levitated by an air cushion," vol. 79, no. 3, p. 036307.

[137] F. Celestini and G. Kirstetter, "Effect of an electric field on a leidenfrost droplet," *Soft Matter*, vol. 8, no. 22, pp. 5992–5995, 2012.

[138] L. Zhong and Z. Guo, "Effect of surface topography and wettability on the leidenfrost effect," *Nanoscale*, vol. 9, no. 19, pp. 6219–6236, 2017.

[139] L. E. Dodd, P. Agrawal, N. R. Geraldi, B. B. Xu, G. G. Wells, J. Martin, M. I. Newton, G. McHale, and D. Wood, "Planar selective leidenfrost propulsion without physically structured substrates or walls," *Applied Physics Letters*, vol. 117, no. 8, p. 081601, 2020.

[140] K. J. Baumeister, R. C. Hendricks, and T. D. Hamill, *Metastable leidenfrost states*. National Aeronautics and Space Administration, 1966.

[141] A. Bouillant, *Dynamiques spontanées en caléfaction*. PhD thesis, Institut polytechnique de Paris, 2019.

[142] A.-L. Himbert-Biance, *Gouttes inertielles: de la caléfaction à l'étalement*. PhD thesis, Université Pierre et Marie Curie-Paris VI, 2004.

[143] P. Brunet and J. H. Snoeijer, "Star-drops formed by periodic excitation and on an air cushion–a short review," *The European Physical Journal Special Topics*, vol. 192, no. 1, pp. 207–226, 2011.

[144] X. Noblin, A. Buguin, and F. Brochard-Wyart, "Triplon modes of puddles," *Physical review letters*, vol. 94, no. 16, p. 166102, 2005.

[145] M. Okada and M. Okada, "Observation of the shape of a water drop on an oscillating teflon plate," *Experiments in fluids*, vol. 41, no. 5, pp. 789–802, 2006.

[146] C. Shen, W. Xie, and B. Wei, "Parametrically excited sectorial oscillation of liquid drops floating in ultrasound," *Physical Review E*, vol. 81, no. 4, p. 046305, 2010.

[147] Y. Fautrelle, J. Etay, and S. Daugan, "Free-surface horizontal waves generated by low-frequency alternating magnetic fields," *Journal of Fluid Mechanics*, vol. 527, pp. 285–301, 2005.

[148] M. Papoular and C. Parayre, "Gas-film levitated liquids: Shape fluctuations of viscous drops," *Physical review letters*, vol. 78, no. 11, p. 2120, 1997.

[149] A. Bouillant, C. Cohen, C. Clanet, and D. Quéré, "Self-excitation of leidenfrost drops and consequences on their stability," *Proceedings of the National Academy of Sciences*, vol. 118, no. 26, p. e2021691118, 2021.

[150] J. E. Bergen, B. C. Basso, and J. B. Bostwick, "Leidenfrost drop dynamics: Exciting dormant modes," *Physical Review Fluids*, vol. 4, no. 8, p. 083603, 2019.

[151] T. R. Cousins, R. E. Goldstein, J. W. Jaworski, and A. I. Pesci, "A ratchet trap for leidenfrost drops," vol. 696, pp. 215–227. Publisher: Cambridge University Press.

[152] A. G. Marin, D. Arnaldo del Cerro, G. R. Römer, B. Pathiraj, A. Huis in't Veld, and D. Lohse, "Capillary droplets on leidenfrost micro-ratchets," *Physics of fluids*, vol. 24, no. 12, p. 122001, 2012.

[153] D. Soto, G. Lagubeau, C. Clanet, and D. Quéré, "Surfing on a herringbone," *Physical Review Fluids*, vol. 1, no. 1, p. 013902, 2016.

[154] P. Agrawal, G. G. Wells, R. Ledesma-Aguilar, G. McHale, A. Buchoux, A. Stokes, and K. Sefiane, "Leidenfrost heat engine: Sustained rotation of levitating rotors on turbine-inspired substrates," *Applied energy*, vol. 240, pp. 399–408, 2019.

[155] M.-y. Chen, Z.-h. Jia, T. Zhang, and Y.-y. Fei, "Self-propulsion of leidenfrost droplets on micropillared hot surfaces with gradient wettability," *Applied Surface Science*, vol. 433, pp. 336–340, 2018.

[156] D. Zhao, Y. Sun, C. Liu, H. Zhan, M. Wang, J. Liu, and Y. Liu, "Temperature-regulated directional bounce of impacting droplets on gradient grooves," *Surface and Coatings Technology*, vol. 356, pp. 132–137, 2018.

[157] M. Labousse and J. W. Bush, "Polygonal instabilities on interfacial vorticities," *The European Physical Journal E*, vol. 38, no. 10, pp. 1–11, 2015.

[158] I. Chakraborty, M. V. Chubynsky, and J. E. Sprittles, "Computational modelling of leidenfrost drops," vol. 936, p. A12.

[159] O. Ozkan and V. Bahadur, "Electrohydrodynamic analysis of bubble burst in large leidenfrost droplets," *Physics of Fluids*, vol. 32, no. 12, p. 122002, 2020.

[160] M. Kintel and C. Wolf, "Openscad," *GNU General Public License, p GNU General Public License*, 2014.

[161] J. C. Burton, A. L. Sharpe, R. C. A. van der Veen, A. Franco, and S. R. Nagel, "Geometry of the vapor layer under a leidenfrost drop," vol. 109, no. 7, p. 074301.

[162] J. A. Sethian, *Level set methods and fast marching methods: evolving interfaces in computational geometry, fluid mechanics, computer vision, and materials science*, vol. 3. Cambridge university press, 1999.

[163] S. Osher and R. P. Fedkiw, *Level set methods and dynamic implicit surfaces*, vol. 1. Springer New York, 2005.

[164] A. Dervieux and F. Thomasset, "A finite element method for the simulation of a rayleigh-taylor instability," in *Approximation methods for Navier-Stokes problems*, pp. 145–158, Springer, 1980.

[165] J. A. Sethian, P. Smereka, *et al.*, "Level set methods for fluid interfaces," *Annual review of fluid mechanics*, vol. 35, no. 1, pp. 341–372, 2003.

[166] D. Pino Muñoz, J. Bruchon, S. Drapier, and F. Valdivieso, "A finite element-based level set method for fluid–elastic solid interaction with surface tension," *International Journal for Numerical Methods in Engineering*, vol. 93, no. 9, pp. 919–941, 2013.

[167] C. Multiphysics, "Introduction to comsol multiphysics®," *COMSOL Multiphysics, Burlington, MA, accessed Feb*, vol. 9, no. 2018, p. 32, 1998.

[168] A. Bouillant, T. Mouterde, P. Bourrianne, A. Lagarde, C. Clanet, and D. Quéré, "Leidenfrost wheels," *Nature Physics*, vol. 14, no. 12, pp. 1188–1192, 2018.

[169] W. Thielicke and E. Stamhuis, "PIVlab – towards user-friendly, affordable and accurate digital particle image velocimetry in MATLAB," vol. 2, no. 1, p. e30. Number: 1 Publisher: Ubiquity Press.

[170] G. K. Batchelor, *An introduction to fluid dynamics*. Cambridge university press, 2000.

RÉSUMÉ

Les systèmes physiques autopropulsés, également appelés actifs, possèdent une phénoménologie riche avec de multiples domaines d'application. Il s'agit de systèmes naturels ou artificiels constitués d'un ou plusieurs individus qui convertissent une source d'énergie interne ou externe pour se mouvoir. Dans ce travail, nous étudions quelques applications de trois systèmes actifs que nous pouvons contrôler à volonté. Premièrement, nous étudions la dynamique d'un robot qui explore de manière aléatoire une région de forme arbitraire. Grâce à l'utilisation d'un nouveau théorème, nous démontrons qu'il est capable de mesurer la surface et le périmètre d'une région quelconque. Ainsi, nous développons une stratégie pour reconnaître des formes préalablement sauvegardées dans un dictionnaire. Dans une deuxième partie, nous étudions un autre système expérimental composé d'aimants en lévitation sur un coussin d'air et se repoussant mutuellement. Ce réseau magnétique se comporte comme un milieu élastique dans lequel les ondes mécaniques peuvent se propager. Nous démontrons qu'une onde propagative peut être inversée temporellement par l'application d'un changement violent de l'amortissement du milieu. L'application successive des chocs d'amortissements nous permet d'absorber sélectivement des composantes monochromatiques d'une onde dont le spectre est large bande. Enfin, nous nous intéressons au contrôle des liquides en état de caléfaction. Nous introduisons un nouveau mécanisme de stabilisation basé sur un drainage partiel de la couche de vapeur qui supporte le liquide pour empêcher l'instabilité de Rayleigh-Taylor. Finalement, nous montrons qu'un contrôle local de la direction de l'évacuation de la vapeur nous permet de propulser des liquides et, ainsi de fabriquer une nouvelle génération de moteurs hydrodynamiques.

MOTS CLÉS

Système actif, reconnaissance de forme, retournement temporel, filtrage spectrale, caléfaction.

ABSTRACT

Self-propelled physical systems, also called active systems, have a rich phenomenology with multiple application domains. They are natural or artificial systems consisting of one or more individuals that convert an internal or external energy source to move. In this work, we study some applications of three active systems that we can control at will. First, we study the dynamics of a robot that randomly explores a region of arbitrary shape. Thanks to the use of a new theorem, we demonstrate that it is able to measure the area and perimeter of any region. Then, we develop a strategy to recognize shapes previously saved in a dictionary. In the second part, we study another experimental system made of magnets levitating on a cushion of air and repelling each other. This magnetic network behaves like an elastic medium in which mechanical waves can propagate. We demonstrate that a propagating wave can be time-reversed by applying a violent change in the damping of the medium. The successive application of damping shocks allows us to selectively absorb monochromatic components of a wave with a broadband spectrum. Finally, we are interested in the control of liquids in the Leidenfrost state. We introduce a new stabilization mechanism based on a partial draining of the vapor layer supporting the liquid to prevent the Rayleigh-Taylor instability. Finally, we show that a local control of the vapor evacuation direction is able to propel liquids and, thus, to build a new generation of hydrodynamic engines.

KEYWORDS

Active system, shape recognition, time-reversal, spectral filtering, Leidenfrost.